MULTI-SCALE SIMULATION METHODS OF CROSSLINKED POLYMER NETWORKS AND DEGRADATION

A Dissertation
Submitted to the Graduate Faculty
of the
North Dakota State University
of Agriculture and Applied Science

By

Aaron James Feickert

In Partial Fulfillment of the Requirements
for the Degree of
DOCTOR OF PHILOSOPHY

Major Department:
Physics

January 2018

Fargo, North Dakota

NORTH DAKOTA STATE UNIVERSITY

Graduate School

Title

MULTI-SCALE SIMULATION METHODS OF CROSSLINKED POLYMER NETWORKS AND DEGRADATION

By

Aaron James Feickert

The supervisory committee certifies that this dissertation complies with North Dakota State University's regulations and meets the accepted standards for the degree of

DOCTOR OF PHILOSOPHY

SUPERVISORY COMMITTEE:

Stuart Croll, Ph.D.
Chair

Andrew Croll, Ph.D.

Daniel Kroll, Ph.D.

Friedrich Littmann, Ph.D.

Approved:

9 January 2018
Date

Sylvio May, Ph.D.
Department Chair

ABSTRACT

Crosslinked thermoset polymers are used heavily in industrial and consumer products, as well as in infrastructure. When used as a protective coating, a thermoset's net-like structure can act as a barrier to protect an underlying substrate from permeation of moisture, salt, or other chemicals that otherwise weaken the coating or lead to substrate corrosion. Understanding how such coatings degrade, both at microscopic and macroscopic scales, is essential for the development and testing of materials for optimal service life. Several numerical and computational techniques are used to analyze the behavior of model crosslinked polymer networks under changing conditions at a succession of scales. Molecular dynamics is used to show the effects of cooling and constraints on cavitation behavior in coarse-grained bulk thermosets, as well as to investigate dynamical behavior under varying degradation conditions. Finite-element analysis is applied to examine strain distributions and loci of failure in several macroscopic coated test panel designs, discussing the effects of flexure and coating stack moduli. Finally, the transport of moisture through model coatings under cycled conditions is examined by lattice Boltzmann numerical techniques, considering several common concentration-dependent diffusivity models used in the literature and suggesting an optimal behavior regime for non-constant diffusivity.

ACKNOWLEDGEMENTS

Without the support of many people over many years, none of this work would have been possible. I first thank my adviser, Prof. Stuart Croll, for guidance throughout my research. My colleagues in the Department of Physics, most notably Prof. Alexander Wagner, Kyle Strand, and Kent Ridl, deserve a standing ovation for innumerable discussions and derivations about diffusion. The graduate students alongside whom I learned and worked are some of the finest colleagues I could hope for, and I will always remember my time with them fondly. And most importantly, the love and support of my family and friends makes all the difference in the world.

Computational and partial funding support from the North Dakota State University Center for Computationally-Assisted Science and Technology is gratefully acknowledged. Additional funding was provided by the Strategic Environmental Research and Development Program under contract W912HQ-15-C-0012. Views, opinions, and/or findings contained in this dissertation are those of the author and should not be construed as an official Department of Defense position or decision unless so designated by other official documentation.

TABLE OF CONTENTS

LIST OF TABLES

LIST OF FIGURES

1. GENERAL INTRODUCTION

Polymeric materials are ubiquitous in daily life. Formed of chain-like structures, polymers are used heavily for industrial, infrastructure, and consumer applications because of their desirable properties for a host of applications. Broadly speaking, polymeric materials are divided into two classes, thermoplastics and thermosets.

Thermoplastics are polymeric materials consisting of chains that are not chemically bonded together. Instead, structural and material integrity is provided through chain entanglement. Many consumer and industrial plastics are thermoplastics, such as polyethylene, polypropene, and polystyrene materials.

Thermosets, on the other hand, are comprised of chains that are chemically bonded together. This crosslinking between chains offers several advantages to thermoplastics; for example, they are often tougher, more chemical resistant, and offer better environmental protection. The network structure formed as a result of the crosslinking process can act as a barrier against the passage of moisture and other invasive species. These include common coating materials like polyurethanes, epoxies, and polyesters.

1.1. Crosslinked polymer networks

In general, performance requirements often dictate or assume that the polymer network of a coating system is completely cured and homogeneous throughout. In the case of a coating that may be only tens or a hundred micrometers thick, it is difficult to experimentally determine the structure of such a network through its bulk.

In practice, crosslinked polymers are produced from two or more reactive liquid precursors. A huge variety of compositions are available to maximize performance of coatings in many different service conditions. Although the individual structure formed by a particular choice of reactive species is always of interest, it is also necessary to understand in more gen-

eral ways how molecular architecture and topology affect the properties of three-dimensional polymer networks.

Crosslinking reactions in organic polymers result in a final solid material that is denser than the initial liquid reactants. Shrinkage during polymer network formation is almost universal. Not only is a solid generally denser than a liquid, but many crosslinking reactions eliminate part of the original reactants as small, volatile reactants; it is also common for the initial liquid system to contain solvent that evaporates during the film formation. Thermal shrinkage may occur since many industrial applications involve curing at a temperature much higher than use temperature in order to assure the required chemical reactions are complete and occur within a reasonable time. Most coating polymers adhere to a substrate or pigments that are much more rigid. After crosslinking has proceeded to the extent that a molecular network spans its volume, it gels and acquires solid-like properties. At that point, the rigid substrate, or included particles, constrains densification and further reaction leads to internal strains within the network in the plane of the substrate. In cases where the polymer forms without such rigid external constraints, it will be free to shrink, but even then it is common to find internal stresses and heterogeneities.

1.2. Modeling techniques

Approaches to modeling polymeric materials vary greatly, and continue to evolve in complexity with advances in mathematical and computational technique. Early statistical approaches to linking structure and mechanical properties relating to conversion and gelation took advantage of topologies that are assumed to be ideal [2, 3], but are insensitive to network flaws that inevitably arise during the crosslinking process [1].

Explicit modeling of dynamical behavior became possible with early availability of computing, where groups of atoms at the Kuhn length are treated as a single charge-free mass that interacts according to Newtonian physics with appropriate potentials applied to impose bonding. This arose as a natural extension of early work on simpler Lennard-Jones fluids [4, 5] to thermoplastic chains [6, 7], but only recently has this been applied more broadly to

thermosets despite the relative simplicity of including the bonding of chains via crosslinkers. Molecular dynamics is used to examine structural properties, curing and cooling processes, multi-atom kinetics and rearrangement behavior, and the results of mechanical changes.

At macroscale lengths, Monte Carlo simulations yield data about stochastic processes like effects of radiation on surface properties and topology [8], and dynamical processes of bulk materials [4]. Other statistical models are used to link degradation to surface property changes [9]. Structural finite-element modeling provides insight into stress and strain distributions in idealized coatings, especially relating to engineering scenarios involving particular substrate geometries like joints and layerings [10, 11].

Moisture transport modeling occurs at several scales. In molecular dynamics, percolating paths can be observed where moisture and other aggressive species might enter a polymer network, either with or without consideration for charge distributions. More indirect mathematical modeling of diffusion typically assumes idealized conditions about density and uniform bonding, and may or may not provide for physical changes like swelling that affect diffusive behavior.

1.3. Environmental testing

The testing of protective coatings depends on the environment in which the coatings are expected to be used. For coatings and paints intended for automotive or aerospace use, for example, near-constant exposure to the natural elements introduces a substantial number of environmental stressors [12]. These include parameters like temperature, air humidity, salt, moisture exposure from rain or dew, ultraviolet (UV) radiation from the sun, and possibly aggressive chemicals contained in cleaners, oil, or fuel. Interactions between different exposure parameters, like acid rain and ultraviolet radiation, further compound the challenges with such testing [13]. Further, mechanical stresses from scratching, moving components, or flexing (*e.g.* when an aircraft takes off or lands) may be present.

The goals of artificial weathering are often twofold. On one hand, it is often desired to have a rather short test protocol accurately reproduce coating degradation or failure that

would occur during longer-term natural exposure in the environment. On the other hand, it may simply be enough to produce a test protocol that will initiate failure modes (often in a way that allows multiple candidate coatings to be compared) to ensure that improper coatings are rejected from further consideration. Despite many years of comparative study, it is well established that commonly-accepted test protocols are often unable to faithfully mimic natural results over time [14]. For many conditions, only tenuous correlations between certain environmental factors and degradation metrics are established [15, 16].

Methods for quantifying the results of coating degradation are varied. After surface pitting and material loss, gloss is often reduced and a coating begins to yellow or otherwise change its coloring. These are easily quantifiable in the laboratory and even somewhat with the eye. Bulk moisture transport can be measured using gravimetric or electrochemical techniques like electrochemical impedance spectroscopy [17, 18].

Most weathering protocols use fairly short times, on the order of four to eight hours, for cycling of parameters. These short times are chosen both for convenience (to scale neatly to the workday) and in an attempt to accelerate the appearance of a diurnal cycle over a shorter total test time. In particular, tests involving UV radiation chambers frequently change temperature, water exposure, and radiation simultaneously in an attempt to reproduce diurnal cycles. However, this likely does not permit a good barrier coating to become sufficiently saturated, and the presence of underlying base coat materials can further complicate this. More recent analyses have suggested the use of longer cycles on the order of half a day, but even this was found not to reproduce the extent of field weathering [19].

Notably absent from common protocols is any type of mechanical stress. This is likely due both to a lack of understanding of the precise relationship between mechanical strain and many other weathering parameters, as well as the practical challenges of stressing a test panel inside a test chamber. Much analysis of the fracture mechanics of a coating is done using free films and stacks, and even then the behavior can be quite complex [20]. This is perhaps to be expected; after all, imparting a large strain to a thin coating on a flat test

panel would likely serve only to fatigue the panel into its plastic regime and make further cycling testing impractical.

1.4. Moisture transport

As is known, most coatings permit, to some degree, moisture ingress [21]. This can be due to imperfections in the preparation process [22], the formation of void space during curing or cooling [23], or because of damage in service. Most accelerated test protocols include moisture cycling since the cycled appearance of atmospheric moisture is present in nature, despite there being no complete and predictive model that accurately correlates a coating's performance in such testing, performance in field testing, and failure modes or lifespan that is likely to occur in service [24]. Since corrosion is linked to moisture reaching the substrate in sufficient quantities, understanding the nature of substrate exposure and coating saturation over time is essential to designing better weathering testing. Some tests do not permit most barrier coatings to reach saturation within a cycle due to the short time scales used [25]. In general, cyclic testing does not provide a complete picture of the failure modes or service life of a system under test [24].

In the field, overall moisture uptake has been observed to enhance photooxidation and hastens degradation processes that decrease service life [25], both alone and in the presence of ultraviolet radiation from the sun [26]. Transport of moisture, and especially the time scales at which it occurs, has broad effects on the thermal and mechanical properties of coating systems over time [27], as well as on the adhesion of a coating to other layers or a substrate [28]. Moisture permeation has also been linked to the presence of pores [29] and pathways [21] within a coating that are often the result of the statistics and chemistry of the crosslinking process [22] both before and after gelation [1, 30], and of cavitation [23].

Several methods exist to model idealized diffusion. Early work on diffusion through coatings focused primarily on precise mathematical modeling and numerical solutions to boundary-matched differential equations governing diffusion [31, 32]. Modern approaches include network connectivity models [29], Monte Carlo simulations [33], and finite-element

analysis [34] for more complex structures like porous media where an effective diffusivity is desired. However, approaches dealing with pore structures may depend on the structure and porosity of the material in question, quantities that most often unknown *a priori*. Additionally, finite-element models tend to be computationally complex and often rely on commercial closed codes. As a whole, there is comparatively little known about the precise dynamics of diffusion through polymeric coatings [35].

Additionally, different approaches exist when multiple layers are considered. In the case of multiple hydrophobic barrier coatings, solutions that apply particular boundary-matched conditions on flux or concentration can be used [32] and matched to experiment via electrochemical methods. When a base coating is hydrophilic, as may happen in some primers, an alternative approach couples Fickian diffusion for any overlying barrier coatings with the assumption of an instantaneous reservoir for the base layer [36]. In either case, different coatings in a multi-layer stackup differ in their effective diffusivity.

Modeling the kinetics of moisture transport through a coating or stack permits a fine-grained approach to examining water content throughout the system over time, which is difficult to achieve in the laboratory [37]. Experimental methods like electrochemical impedance spectroscopy are well suited to examine bulk properties like diffusivity and uptake during cycled exposure [38], but have the disadvantage of requiring consistent preparation, application, and measurement conditions. However, it is straightforward to gain information about the diffusion process. Fickian diffusion has been shown to provide a good basis for water transport through a variety of barrier and underlying base coatings with different chemistries [28, 38, 25, 39]. Other work has examined bilayer systems where an instantaneous reservoir model was used for a hydrophilic base coat [36]. Multilayer systems provide additional modeling challenges, since additives like pigments can lead to a variety of unexpected changes in diffusivity [40] and boundary conditions must be carefully considered [32]. However, an assumption of generally Fickian behavior provides good matching to experiment under a variety of setups.

1.5. Organization

This dissertation is organized into four major topics, each comprising a different, but related, computational application of numerical modeling to crosslinked polymer networks. Each topic is provided its own introduction that introduces the particular method used, as well as providing a discussion of important results in the area of study.

The second chapter presents a molecular dynamics study of coarse-grained bulk thermoset heterogeneity, in order to better understand the internal structure of general crosslinked networks. Using a fully periodic system with different crosslinker functionalities, a stochastic crosslinking process results in regions of variable network formation. This setup leads to cavitation depending on the curing procedure, the temperature relative to the glass transition, and the functionality of the network.

The third chapter presents a computational study of short-time network cage behavior using molecular dynamics, in which it is shown that crosslinked networks exhibit molecular transitions between cage regions imposed by their neighbors. The statistics of this behavior are investigated in detail and shown to exhibit dependence on temperature and crosslinker functionality. Structural degradation is imposed on the system via the removal of bonds and compared to the fully-formed network results, noting comparisons to traditional bulk network models and properties.

The fourth chapter examines coatings on a macroscale and investigates structural properties of coating strain over common geometries. Since mechanical stress is not typically studied in laboratory coating testing, the origins of adhesive or cohesive failure are not well understood in engineering or structural situations. Structural finite-element analysis is used to examine the strain distributions in a coating over a gap sealant under various substrate geometries and displacements, and comment on the corresponding results for a countersunk rivet. Possible loci of failure, as well as a dependence on coating moduli, are discussed throughout.

The fifth and sixth chapters use discrete lattice Boltzmann numerical methods to model moisture transport through a finite single-layer coating adhered to a substrate and exposed to a cycled moisture reservoir. The numerical framework is developed and verified alongside an analytical derivation. Since the lattice diffusion equation is typically derived only up to a second-order Taylor approximation, its validity is confirmed across a wide parameter space, such that further refinement of the approximation is unnecessary for this application. The numerical method is used to study the effects of moisture cycling under different concentration-dependent diffusivity functional forms over time. While constant diffusivity leads to a simple scaling argument for concentration at a substrate, non-constant forms yield much different behavior. Applications to laboratory test protocols are discussed.

The seventh chapter extends the lattice Boltzmann model to the case of multiple coating layers, where the diffusion rate and maximal saturation of each layer are varied independently. An application of Henry's law is used to account for differences in relative saturation layers. This is shown to result in a filling effect as maximal saturation increases, delaying the passage of moisture to subsequent layers.

Together, these studies show the broad range of numerical techniques that provide insight into polymeric coatings at a variety of length and time scales, and provide frameworks for future study, design, and testing of coating materials.

2. CAVITATION IN CROSSLINKED POLYMERS: MOLECULAR DYNAMICS SIMULATIONS OF NETWORK FORMATION

2.1. Introduction

The protective qualities of a polymer depend on its strength and whether it allows foreign species to permeate and attack a substrate. It is usually assumed that a higher degree of crosslinking leads to stronger, less permeable materials because the network structure is denser and will not allow foreign species to percolate. However, it is also recognized that aggressive species from the environment do, in fact, permeate through crosslinked polymers. The mechanisms involved are not well understood [21], making it difficult, *a priori*, to design a completely successful composition. A better understanding of the molecular and nanoscale causes of this permeability is needed in order to design materials with improved protective properties. However, traditional approaches to understanding crosslinked network formation focus on the overall crosslinked network, not on the possibility of void formation or other local variations [41, 42, 43, 44]. In particular, an interest in possible pore formation in crosslinked polymers that are formed from liquids is supported by simulations that show pores can arise by cavitation in amorphous liquids [45, 46] and even metals [47].

Molecular dynamics is a computational technique that tracks the state of a system of particles through time. Once set in an initial configuration and assigned velocities, interparticle interactions are used in the computation of forces, which then give rise to accelerations that are used for position evolution of each particle. The models we use for thermosets

The work of this chapter was completed by the author and collaborators M. Zee, D.M. Kroll, and S.G. Croll in a published paper [23]. Zee investigated many material parameters associated to a range of coarse-grained precursors that established the cavitation phenomenon. Simulations and data analysis were conducted by the author, Zee, and Kroll. Three-dimensional visualizations were produced by the author and Kroll, with additional analysis from Croll and Zee.

are subject to a coarse-graining process in which no charges are considered; instead, inter-particle interactions will be governed by potentials that model van der Waals interactions, short-range repulsion, and strong covalent bonding. The use of any barostats or thermostats to control pressure or temperature are included in the velocity Verlet algorithm used in each timestep.

Although molecular dynamics was developed decades ago, there have been few studies applying it to highly crosslinked polymer networks. The use of a coarse-grained bead-and-spring model, previously used to examine bulk polymer melts consisting of single chains, was also used to examine adhesion and fracture mechanics in model thermosets [48, 49, 50]. The coarse-graining process, which removes atomistic effects by treating groups of atoms as a single functional unit, is useful since it both generalizes the results and decreases computation time. We are able, for example, to simulate such materials on time scales on the order of microseconds and lengths on the order of tens of nanometers. Atomistic simulations, which include chemical and other specific interactions, require far higher resource levels to achieve the same scale, and may provide results that are limited in scope.

Crosslinked polymer networks are created from a wide range of molecules with different numbers and types of reactive sites. Early studies investigated crosslinked rubbers [51, 52], but typical coating or composite network polymers are more rigid and more densely crosslinked. Here, we use two selected systems to exemplify a range of possibilities within the realm of highly-crosslinked polymers. One is formed from a 3-functional "crosslinker" that reacts with a 2-functional chain extender. The resulting network consists of 3-fold coordinated nodes, the minimum required to form a three-dimensional crosslinked network, connected by chains containing four beads. This is representative of networks formed from a wide variety of crosslinking chemistries that are used in coatings technology. The other system type employs a 6-functional crosslinker that reacts with the same chain-extender and produces a much more densely crosslinked network. These two systems represent coatings and composites that are typically much more highly crosslinked than rubber networks, and

thus complement the prior work of Grest and co-workers [51, 52] that described rubber-like networks.

Networks were formed by crosslinking at high temperatures to simulate the mobility of liquid reactants, and at low densities characteristic of liquids in order to simulate the formation from liquid precursors. A volatile solvent is very common in coating formulations, but was not included here for simplicity. The temperature of the resulting networks was subsequently varied and they were investigated well into their glassy, solid state. Two scenarios were considered. In the first, the size of the simulation cell was held fixed as the network was cooled so that it suffered overall shrinkage strain, similar to what would occur in a network attached to a rigid substrate on curing. In the second, the system was cooled under zero-load conditions, which corresponds to a bulk polymer that is free to shrink. In practice, a polymer can flow and accommodate shrinkage while it is crosslinking, but still in the liquid, sol state, so most practical situations will fall in between the two procedures used here. In this work, the emphasis is on understanding the general features of pore formation and obtaining an understanding of the network features that control or permit them.

2.2. Models

The simple coarse-grained models used here are generated from precursors consisting of a 2-functional chain extender of two beads ("dimer" for brevity) and a "crosslinker". In coarse-grained models such as these, one bead represents not one atom but, rather, a group of atoms with the convenient result that network precursors have only a few beads per strand.

Following earlier work [48], the minimal case of two beads linked by a single spring is used for one of the reactants where each bead has one reactive site. The other reactants are two types of crosslinkers that consist of several beads with different functionalities, in order to span a range of crosslinking densities and structures. Figure 2.1 shows the precursors along with examples of maximal network formation.

Beads are allowed to bond together according to the rule that black (as shown in Figure 2.1) must react with colored; no colored–colored or black–black reaction is allowed.

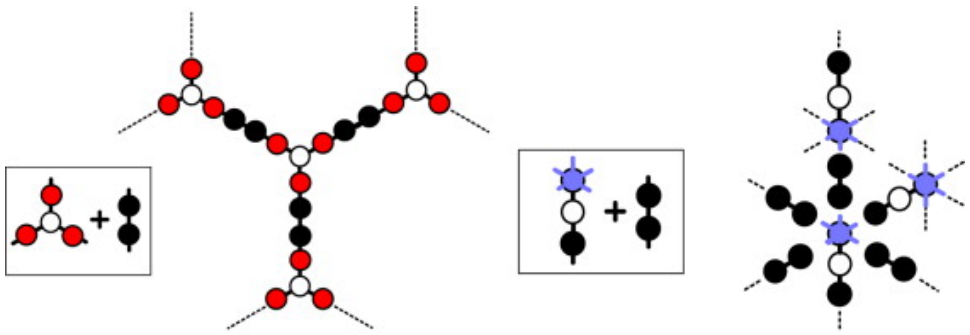

Figure 2.1. Precursors and sample networks for 3-4 (left) and 6-2 (right) systems

Table 2.1. Numbers of dimers, crosslinkers, and total beads in each system

System	Dimers	Crosslinkers	Total beads
3-4	2448	1632	11424
6-2	3264	1632	11424

The middle (open) beads do not react. So for the 3-functional system, a crosslinker molecule cannot react directly with another crosslinker molecule. For stoichiometry and 100% conversion, in the 3-functional system each crosslinker (four beads) shares three dimers (two beads each) with other crosslinker molecules, as shown in Table 2.1.

In the other system type, the 6-functional bead has one functionality already occupied by a two-bead tail, and that tail has a black bead that can react with one functionality on a separate crosslinker. Thus, this system needs only enough dimers for sharing between four functionalities of each crosslinker, *i.e.* $1632 \times 4/2 = 3264$ dimers.

A small number of simulations were performed using systems containing 1,428,000 beads in order to check for finite size effects and verify the results obtained using smaller networks, which was the case. Because of this, results presented here are for simulations consisting of 11,424 beads; these systems were found to be large enough to produce results characteristic of the bulk, yet small enough to allow us study a large range of parameters in a reasonable amount of time. Other studies of the same coarse-grained models with different simulation sizes support this [1, 30].

Periodic boundary conditions and a rectangular parallelepiped simulation cell geometry were used to avoid boundary effects. All non-bonded beads interact via the cut-off and shifted Lennard–Jones (LJ) potential

$$U(r) = \begin{cases} U_{\mathrm{LJ}}(r) - U_{\mathrm{LJ}}(r_c) & (r \leq r_c) \\ 0 & (r > r_c) \end{cases} \tag{2.1}$$

with a cutoff at $r_c = 2.5\sigma$ [51], where

$$U_{\mathrm{LJ}}(r) = 4\epsilon \left[\left(\frac{\sigma}{r}\right)^{12} - \left(\frac{\sigma}{r}\right)^{6} \right]. \tag{2.2}$$

Here σ is the length scale in the LJ potential, r the distance between bead centers, and ϵ the energy parameter. This potential models the van der Waals attractive forces between all the beads and a strong repulsive core that defines the extent of the bead. "Covalent" bonds between beads that were pre-existing or formed during reaction are described using a potential that prevents chain crossing [51]. This bond potential is the sum of the Weeks-Chandler-Anderson potential, which is the purely repulsive LJ interaction with a cutoff at $2^{1/6}\sigma$ (the minimum of the LJ potential), and a finite-extensible nonlinear elastic (FENE) attractive potential [52]

$$U_{\mathrm{FENE}} = \begin{cases} -\frac{R_0^2 k}{2} \ln\left[1 - \left(\frac{r}{R_0}\right)^2\right] & (r < R_0) \\ \infty & (r \geq R_0) \end{cases} \tag{2.3}$$

where $k = 30\epsilon/\sigma^2$ and $R_0 = 1.5\sigma$. Here, k controls the strength of the spring (bond) potential and R_0 is the maximum bond extension. This choice of parameters introduces incompatible length scales in the inter- and intra-polymer interactions which inhibits crystallization, allowing us to study solely amorphous materials. This choice also ensures relatively strong bonds and avoids chain crossing. The average bond length for these parameter choices is

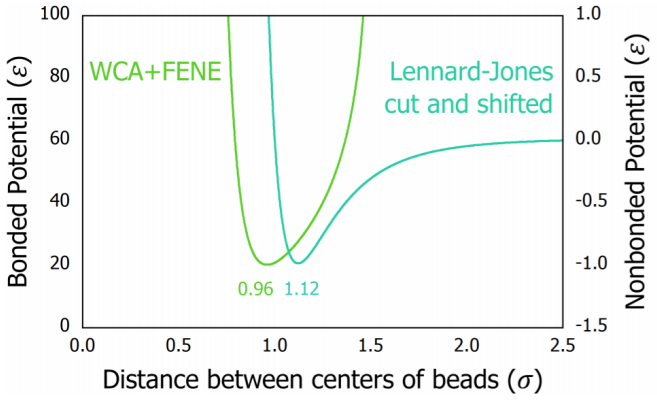

Figure 2.2. Unbonded (LJ) and bonded (WCA+FENE) potentials

narrowly distributed around 0.961σ. A comparison of the two potentials is shown in Figure 2.2.

The Large-scale Atomic/Molecular Massively Parallel Simulator (LAMMPS) software, developed at Sandia National Laboratories, was used for simulations. It iteratively solves equations of motion to analyze the kinetic behavior of our systems using these potentials, and is particularly useful due to its efficiency over parallel processing units [53].

All dimer and crosslinker beads have identical LJ parameters. Before crosslinking, the mixture of dimers and crosslinkers is equilibrated at a high temperature $T = 1.0\epsilon$ at zero load using a Nosé–Hoover thermostat and barostat with a time step of 0.005τ, where $\tau = \sigma(m/\epsilon)^{1/2}$ is the Lennard–Jones unit of time. After equilibration, the network is dynamically crosslinked under the same conditions.

To form the network, every 2000 time steps (10τ), potential bonding partners that have open bond sites and are separated by a distance less than 1.3σ are identified, and the nearest potential bonding partners are crosslinked with a probability of 10%. A detailed description of the crosslinking procedure can be found elsewhere [48, 49, 54]. This low probability allows the network to form slowly and evenly. Crosslinking continues until a conversion $\sim 98\%$ is achieved.

Both system types were replicated five times, each with a different random seed, to ensure that the behavior reported was typical and did not depend on a particular random

arrangement. There proved to be only negligible differences between replicas for each system, confirming that they were of sufficient size to produce consistent results characteristic of a bulk system [48]. Results for the larger simulation size were consistent with the behavior of the 11,424 bead simulations.

In one case, 3-functional crosslink nodes are connected by chains consisting of four beads. This system emulates many coating polymers with typical properties. The other system has a crosslinker of much higher functionality with only two beads between junctions and, in this form, has been used elsewhere [48, 49, 54]; it may also be thought of as being a very compact crosslinker with a functionality $f = 6$ that has already reacted with one dimer. The notation for these two systems in discussion here is "3-4" and "6-2". Additionally, 4-functional systems, with both 2 and 4 beads between nodes, have also been investigated; they exhibit behavior intermediate between the systems reported here and do not provide additional insight into the phenomena discussed here.

2.3. Results and discussion

Our focus is on the formation of voids within crosslinked polymer networks. However, understanding how and where the voids arise requires some background on the nature of the networks and their properties. These are dealt with first.

2.3.1. Crosslinking

Crosslinking reactions were continued until approximately 98% of all possible bonds were formed. This is higher than is generally achieved in practice or in the laboratory, but this value provides an easily repeatable reference point for further studies. The number density of the initial "liquid" mixture is $\rho = 0.8\sigma^{-3}$. Because of the comparatively short FENE bond length, the density of the systems increases while crosslinking, with $\rho = 0.91\sigma^{-3}$ for the 3-functional system and $0.95\sigma^{-3}$ for the 6-functional system, at $T = 1.0$ and 98% conversion.

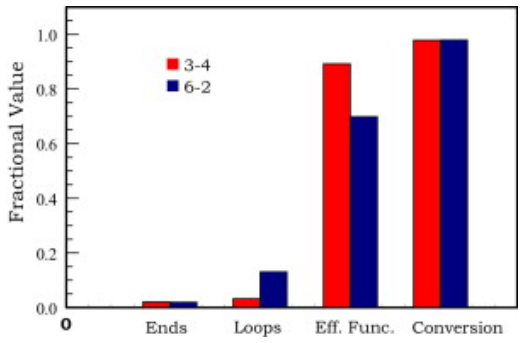

Figure 2.3. Fraction of dangling ends, loops, scaled effective functionality, and conversion for both network types

2.3.2. Network defects

A loose or dangling end occurs when a reactive site remains unused: for example, a dimer bound to a crosslinker at only one end. Loose ends do not contribute to the modulus of a network. Another network defect considered is a minimal loop, which occurs when a dimer makes both bonds to a single crosslinker molecule. Although minimal loops may contribute to elastic and barrier properties in compression (and by entanglements in less densely crosslinked systems), this is improbable here because of the short length of the dimers. To a first approximation, minimal loops are probably not network effective at all, in a manner analogous to dangling ends. To characterize the effective connectivity of each crosslink site, the numbers of bonds, minimal loops, and loose ends were determined for each crosslinker. The effective functionality was then determined using the following relation:

$$[\text{effective functionality}] = [\text{bonds made}] - 2[\text{minimal loops}] - [\text{loose ends}]$$

The effective functionality is essentially the number of crosslinks to larger network fragments at each node, as a fraction of the nominal functionality. The effect of network defects in the 3-4 and 6-2 networks is shown in Figure 2.3. While the incidence of dangling ends was small for both models, the occurrence of loops increases with the functionality of the crosslinker, as might be expected. For this reason, the 3-4 model has a relatively larger effective functionality than the 6-2 model.

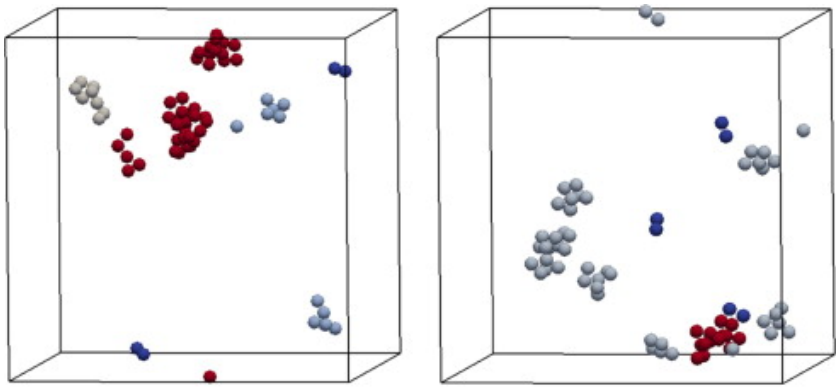

Figure 2.4. Position and size of fragments in (a) 3-4 and (b) 6-2 networks after crosslinking. In each case, fragments with between 2 and 14 beads are shown. Colors only differentiate separate clusters.

Further examination showed that there were a few fragments of material that were not incorporated into the main network during crosslinking. Figure 2.4 contains representative diagrams of the network showing only the fragments. Crosslinking requires that reactive functionalities can approach each other closely enough to react. Statistically, there will always be a small number that will not diffuse to encounter a suitable co-reactant, so that there will be a small number of clusters not connected to the network backbone, especially in stoichiometric systems. This mirrors practical experience since a small amount of material can often be leached out of crosslinked polymer networks using a suitable solvent [55, 56]. For the systems described in the figure, 0.58% of the nodes in the 3-4 model and 0.6% of the nodes in the 6-2 model were not linked to the network backbone.

2.3.3. Glass transition

To determine the glass transition temperature T_g, simulations were performed at zero load using a Nosé–Hoover thermostat and barostat. The temperature was lowered incrementally from $T = 1.0$ at a rate of 0.1 reduced units per 400,000 time steps (2000τ). Data collected during the last 100,000 time steps of each stage were averaged in order to create the plots shown in Figure 2.5 from which the glass transition temperature was determined at the intersection of the straight lines fitted to the high and low temperature results.

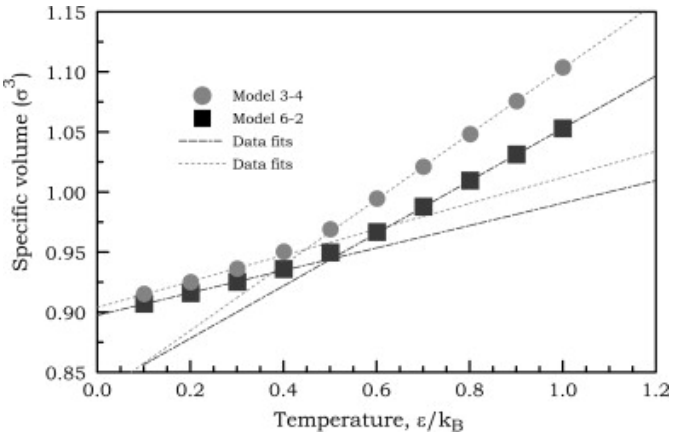

Figure 2.5. Specific volume during cooling for 3-4 and 6-2 systems, with linear intersection fit

Table 2.2. Glass transition temperature and Young's modulus for both system types; value for Young's modulus is at $T = 1.0$

System	T_g (ϵ/k_B)	E (ϵ/σ^3)
3-4	0.448	0.17
6-2	0.502	1.02

The glass transition temperature was found to be close to $T_g \approx 0.5$ for both systems, and is shown in Table 2.2. As expected, the glass transition for the more constrained 6-2 network is higher than for the 3-4 system. From this value, these simulations provide distinct, broad rubbery and glassy regimes. The results for the 6-2 system agree with results obtained elsewhere [48].

2.3.4. Elastic moduli

Calculations of elastic moduli above T_g were made at $T = 1.0$ in order to confirm that the simulations of these two networks conform to expectations for crosslinked polymers. Some results are listed in Table 2.2.

It can be seen that the higher functionality and shorter chains between crosslinks resulted in the 6-2 system having a larger rubbery modulus than the 3-4 system, consistent with the predictions of rubber elasticity theory.

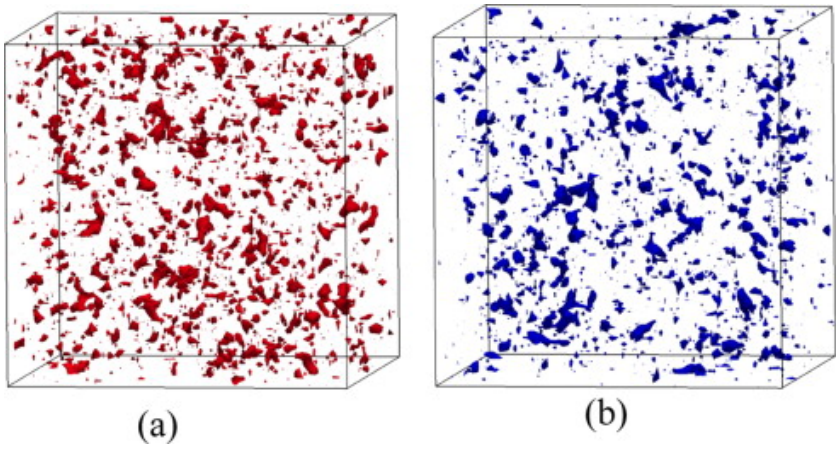

Figure 2.6. Pores in crosslinked (a) 3-4 and (b) 6-2 systems at $T = 1.0$, with isosurfaces showing the locus of points a distance 0.8σ away from the nearest bead

2.3.5. Void formation

It is not possible in a random dense network for all the beads to be positioned in their potential minimum. While many are, there will be a distribution of unoccupied, "free" volume where it is not the case. In the crosslinked networks at $T = 1.0$, (*i.e.* in the initial, hot, rubbery state), there are many small pores distributed randomly across the volume of the network. Figure 2.6 shows this free volume as the locus of points a distance 0.8σ away from the nearest bead. In the 3-4 system, the maximum neighboring bead separation is 1.08σ; in the 6-2 system, it is 1.11σ.

There appears to be little difference between free volume distributions in these two systems, with the more highly functional system having slightly fewer but larger pores. Images in the figure conform to what might be conventionally expected when the term "free volume" is used in discussions; there is no sign of cavitation under these conditions. Our interest here is to understand how the free volume distribution changes as the systems are cooled from the rubbery state into the glassy state.

We use two distinct protocols during cooling in order to identify parameters which may influence both the distribution and magnitude of free volume. They represent limiting cases of what occurs in industrial thermosets which may be first oven-cured to obtain high conversions and then cooled to ambient temperatures for use. Coatings formed in this

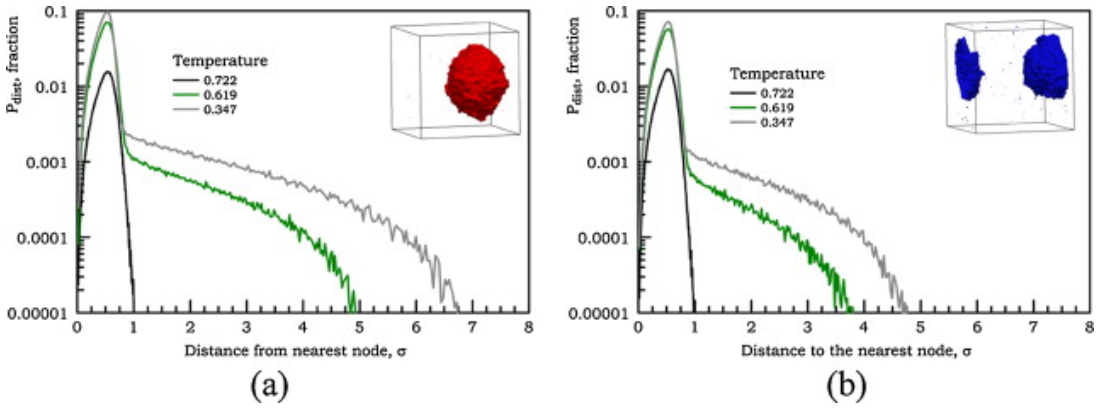

Figure 2.7. Pore distribution P_{dist} at various temperatures after ramped cooling for (a) 3-4 system and (b) 6-2 system, with visualization of pore space at the lowest temperature used for each

manner are confined in lateral dimensions by adhesion to their substrates, and shrinkage in the direction of thickness may also be restricted because it requires cooperative motion of polymer chains across long distances. Similarly, in composites, extensive shrinkage of the matrices is inhibited by the rigid, densely packed reinforcement fibers, and in pigmented coatings by rigid pigment particles. Such constraints are represented here by cooling at fixed volume (*i.e.* fixed cell dimensions). The second scenario is cooling at zero load (the simulation cell is allowed to shrink), which models a bulk polymer with no rigid constraints that is free to relax the strains caused by cooling and covalent bond formation. We expect the behavior of real systems to be bracketed by the results for the two cases used here. We also study the evolution of the pore space when the networks, cooled at constant volume (constrained), are then allowed to relax under zero load. The effect of cooling rate in the various circumstances will be explained as the results are discussed.

To quantify the distribution and size of pores, we divide the simulation box volume into a fine mesh of equally spaced nodes. At each node, we compute the distance to the nearest bead, accounting for periodic boundary conditions. We aggregate these node-bead data into a probability distribution P_{dist} that a randomly selected node is a given distance from the nearest bead. Figure 2.7 shows the size distribution for the ramped cooling scheme, along with the corresponding pore isosurfaces.

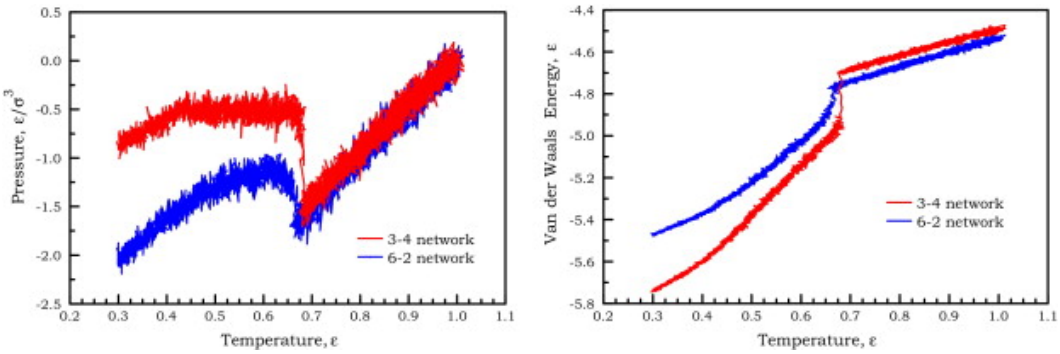

Figure 2.8. Pressure (left) and van der Waals energy per particle (right) for both 3-4 and 6-2 systems during cooling at fixed volume

Initially, at high temperatures, $P_{\text{dist}}(d/\sigma)$ has a narrow peak near $d \approx 0.5\sigma$, which is expected for nodes between beads that are close to the minimum in the FENE (bonded) potential (0.961σ) or the minimum for the LJ potential for non-bonded beads (1.12σ). These pore spaces at high temperature were shown in Figure 2.6. The distribution changes little as the temperature is lowered until, at a cavitation temperature $T^* \approx 0.673$ for the 3-4 system and $T^* \approx 0.658$ for the 6-2 system, a large-separation tail in the distribution suddenly appears, indicating that a larger open spaces have formed. The tail in the distribution for the 6-2 system, for example, indicates that a void has formed that has a radius greater than 4σ at $T = 0.619$. The tail in the distribution is somewhat larger in the 3-4 system, and in both cases, the tail increases in size upon further cooling, as expected. Visualizations of this pore space, shown as insets in the figure, indicate that the pores are globular in form. Pores are present, even though there is no possibility, in these simulations, of spaces being left behind by the escape of volatile material.

Figure 2.8 shows the variation of the pressure and van der Waals energy per particle as a function of temperature for ramped cooling at fixed volume. As the temperature is lowered from $T = 1.0$, the network shrinks and the pressure becomes increasingly negative (tensile) until the tensile strength of the van der Waals network is reached. At this point it ruptures and a void is formed, relieving some of the stress.

Table 2.3. Density ρ, cavitation temperature T^*, and cavitation onset pressure P^* for 3-4 and 6-2 systems during temperature ramp from $T = 1.0$ to $T = 0.3$ at fixed volume over six million timesteps.

System	Density (ρ)	T^* (ϵ/k_B)	P^* (ϵ/σ^2)
3-4	0.9075	0.673	-1.53
6-2	0.9480	0.658	-1.71

The fact that the surrounding crosslinked network does not rupture limits the possible stress relaxation. The pressure then stays relatively constant (and the void size increases) as the temperature decreases until the low temperature glassy phase is reached and the pressure starts to become more negative again. The behavior of the van der Waals energy per node as a function of temperature is consistent with this picture. In particular, it initially decreases linearly with temperature until dropping discontinuously at the void-formation transition T^*. Below the transition, the density of the coherent regions of van der Waals network is greater than above the transition, resulting in significantly stronger binding energies. We find a transition temperature for each system consistent with the onset of void formation. Because of the higher density of the 6-2 network, the critical pressure for the 6-2 network ($P^* = -1.71\epsilon/\sigma^2$) is larger in magnitude than for the 3-4 network ($P^* = -1.53\epsilon/\sigma^2$). Note that these transition temperatures are significantly higher than the glass transition temperatures for these networks. The results are summarized in Table 2.3.

The pore size and morphology depend heavily on the rate of cooling. Figure 2.9 compares the pore size distributions at $T = 0.3$ after a rapid quench (blue) and slow ramped cooling (red) starting from the same $T = 1.0$ crosslinked configuration. To generate the quenched configuration, velocity rescaling was used to quench the network to $T = 0.3$. The simulation was then continued for 400,000 time steps using a Langevin heat bath algorithm. For the ramped cooling, the temperature was more slowly lowered to $T = 0.3$ over six million time steps using the Langevin heat bath algorithm. In both cases the simulations were performed at fixed volume. As might be expected, the resulting pore space is larger

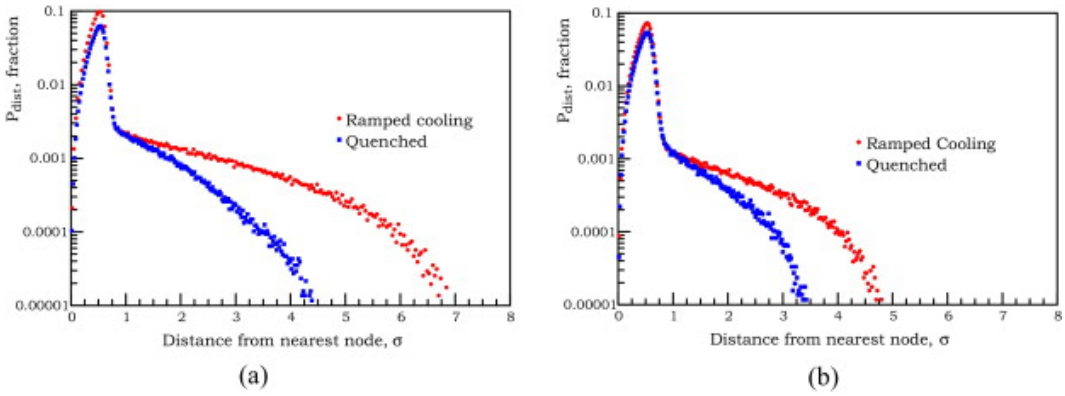

Figure 2.9. Pore distributions for (a) 3-4 and (b) 6-2 systems, comparing ramped and quenched cooling methods to $T = 0.3$

for ramped cooling, since the void had a longer time to anneal and grow above the glass transition temperature.

An interesting result is that the pore morphology is very different for the two cooling scenarios.

2.3.6. Pore morphology

Figure 2.10 shows the pore space isosurfaces for the 3-4 and 6-2 networks at $T = 0.3$ after a rapid quench. The globular pore shape for a slow ramped cooling from $T = 1.0$, at fixed volume, was already shown previously. The isosurfaces are again the locus of points a distance 0.8σ from the nearest bead. After a quench to below T_g, several pores have formed, and although their total volume is less than was found after a slow temperature ramp, the pores have a ramified structure that almost reaches across the simulation cell. It may not have been appreciated that such void structures were possible in a crosslinked network, but it is very important because the protective qualities of polymers used in coatings and composites, such as permeability as well as other properties, are obviously related to any such structural imperfections.

A convenient measure of pore size is the reduced pore volume v_p quantified using the pore distribution functions, with values greater than the given threshold values, and normalized by the simulation cell size. Results for v_p at $T = 0.3$ for pores formed using both cooling protocols are shown in Table 2.4.

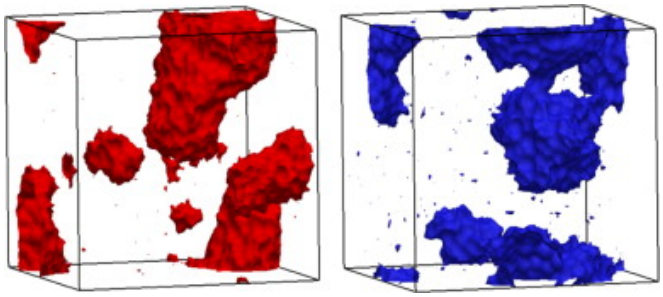

Figure 2.10. Ramified pore structure in 3-4 (left) and 6-2 (right) systems after quenched cooling to $T = 0.3$

Table 2.4. Reduced pore volume v_p at $T = 0.3$ for 3-4 and 6-2 systems after either ramped or quenched cooling for varying thresholds (in parentheses; units of d/σ)

System	Ramped (0.8)	Ramped (1.0)	Quenched (0.8)	Quenched (1.0)
3-4	0.123	0.109	0.110	0.091
6-2	0.084	0.072	0.074	0.057

What happens to the pores when the constant volume constraint is relaxed? Figure 2.11 compares the pore space distribution function $P_{\text{dist}}(d/\sigma)$ after ramped cooling along an isochore (lines) and subsequent relaxation over one million time steps at zero load, with the fixed volume constraint removed (symbols). Data for $T = 0.529$, $T = 0.442$, and $T = 0.347$ are shown.

Above the glass transition, the network relaxes on this time scale and the pore vanishes. Below T_g, relaxation slows as expected. Figure 2.12 collects these results and shows the reduced pore volume as a function of temperature. Again, we see that the 3-4 system

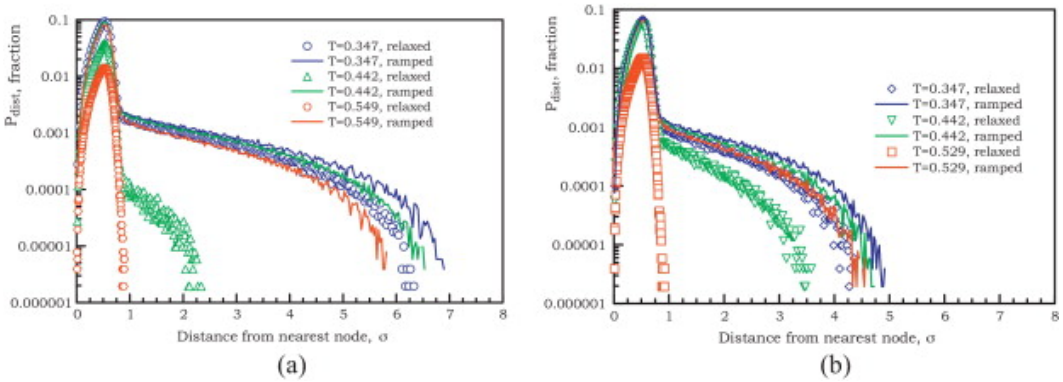

Figure 2.11. Pore distributions for (a) 3-4 and (b) 6-2 systems at various temperatures, showing constant-volume (solid lines) and zero-load (symbols) phases of the cooling process

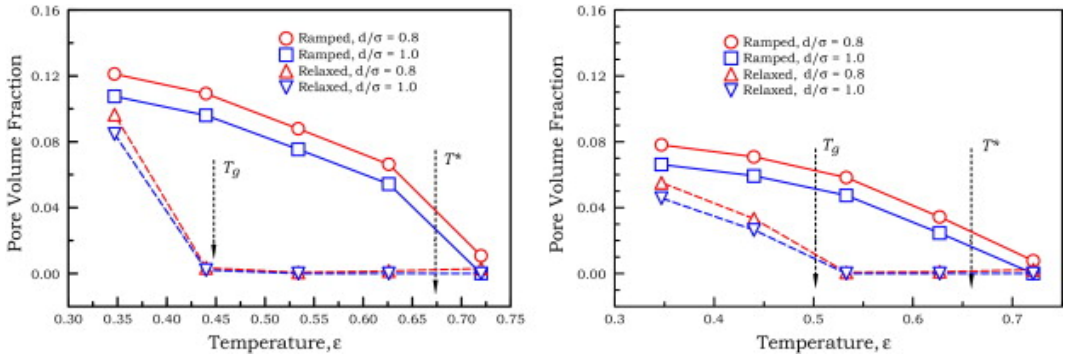

Figure 2.12. Pore volume fraction before and after zero-load relaxation as a function of temperature for 3-4 (left) and 6-2 (right) systems, using two different node-bead threshold distances

permits larger void volume than does the more densely functional 6-2 system. Below the glass transition, decreased mobility results in greater residual pore volume. Correspondingly, the pores may persist below T_g in real crosslinked polymer networks even in the absence of external mechanical constraints. Further, the voids are up to several bead diameters in size. Corresponding pores in an actual polymer network might be up to several nanometers in diameter and could contribute to the permeability of water and ions and serve as initiation sites for larger scale mechanical failure.

2.3.7. Cavitation in thermosets

Void formation by cavitation has been explored in a variety of simulations of liquids and materials in which there is only a single, general interaction between the components, e.g. polymer cavitation and crazing during deformation of thermoplastic polymers [45, 47, 57, 58, 59, 60, 61]. However, we find that pores appear even in a highly connected network of strong covalent (FENE) bonds in addition to Lennard–Jones forces between all the beads.

This appearance of the large pores is not a gradual consolidation of pore volume over a range of temperature, but a sudden occurrence at a particular temperature and pressure. For our current choice of models and parameters, pores form above the glass transition temperature; while this may not be a universal feature of crosslinking systems, it is important because many crosslinked polymers are used in a temperature range around or below Tg. Pore formation was seen in previous simulations of the 6-2 polymer system

[49, 50], but unexplored there because the focus was on the mechanical properties of the crosslinked network. Void formation and cavitation in LJ liquids has been extensively studied [45, 46, 62, 63, 64, 65, 66] where it was found that void formation generally occurs at the spinodal and is held to be characteristic of liquids. Experiments using positron annihilation spectroscopy confirm the formation of void structures in a variety of materials [67, 68, 69].

Qualitatively, the cavitation in these systems is easy to understand. As the temperature is lowered, the specific volume becomes smaller as the particles relax toward their potential minimum. At fixed volume, this causes the pressure to become negative, which can cause local cavitation when the tensile stress exceeds the mechanical strength of the material, resulting in a reduction of the total free energy. The density–pressure–temperature parameters at which cavitation voids form in van der Waals fluids [64, 70] are very similar to what we find in these crosslinked rubbery networks, which confirms that the voids in these crosslinked networks are indeed the result of cavitation. This, and the fact that the network backbone remains intact through the transition, indicates that the failure of the homogeneous Lennard–Jones (van der Waals) bonding is responsible for void formation, even in crosslinked networks.

It may be difficult to imagine how such cavitation could occur in an homogeneously crosslinked network. However, the crosslinking process results in a network in which many nodes, that are spatial neighbors, are not bonded together. Thus there are potential fissures, of varied extent, across which only Lennard–Jones (*i.e.* van der Waals) forces are present. In addition, the internal pressure is not homogenously distributed, but stress is concentrated at the crosslink nodes; cavitation appears to nucleate at such nodes next to a potential fissure. These few, irregular fissures are where voids can form in these networks, in close analogy to what happens in pure Lennard–Jones systems.

These results indicate van der Waals network failure and void formation should occur in a wide range of materials as they are cooled under conditions where local stresses cannot relax. We find voids form during network formation and solidification, prior to any in-

service stresses. If that is true, they are likely initiation sites for larger failures during service, especially if the system cannot relax to eliminate the voids because the prevailing temperature is below the glass transition temperature. This would also be true of their likely impact on permeability in protecting the reinforcing elements of a composite or the substrate of a coating. It is notable that significant voids appear even in the highly crosslinked system modeled here. Solely increasing network density may not diminish permeability enough to improve barrier properties, but controlling the glass transition temperature and compatibility of the network with the possible permeants must also be considered.

2.4. Conclusions

In studying crosslinked networks using a typical coarse grained molecular dynamics approach, void formation and growth is found that initiates above the glass transition temperature of the network as it cools through its rubbery to its glassy low temperature state. It is somewhat surprising that these cavitation voids occur in simulations of crosslinked polymers where the network is supported by strong directional, FENE (covalent) bonds as well as the much weaker, non-directional Lennard–Jones (van der Waals) interactions. Such voids have been noted and studied in simulations of liquids and amorphous solids with only Lennard–Jones forces, at very similar values of pressure, temperature and density. These voids are not a consolidation of "free volume", nor due to a loss of volatiles, but are caused by cavitation, happening as the solidification/cooling stresses exceed the local tensile strength of the material. The voids first appear in the rubbery state while the network has substantial mobility. That voids occur during the formation of crosslinked networks seems to be a new observation that has consequences for the end-use properties of such materials and their long term performance. Although these finding are very consistent with previous simulations of liquids, the time scales of all such simulations is very brief and it may be that the pores will disappear in real liquids and solids if they are well above their glass transition temperature and are not constrained by adhesion to, or between, more rigid material bodies. This is currently under study, where these effects in much larger and more extended simulations

are investigated. However, pores are much more likely to persist if the polymer network is maintained near or below the glass transition, and constrained by adhesion. This is the case for most polymer coatings.

The simulations show that the network connectivity, network strength and internal pressure are all heterogeneous. Polymers formed from mobile reactive precursors produce clusters of reacted material as the network grows toward the gel point. It follows that there can be adjacent regions that are not connected by covalent bonds and are weak points where voids can form to reduce the internal tensile strain caused by the solidification/cooling process. These voids, depending on circumstances, may comprise a significant fraction of the simulation volume, and their dimensions would scale to the order of nanometers in a physical system. This suggests that there may be regions of lowered density, as seen in recent results [71]. These would occur especially in polymers that are confined by adhesion to substrates, reinforcing fibers or pigment particles, and are in use around or below their glass transition temperature. Not only may the voids be the initiation sites of larger scale mechanical failure, but they are likely to contribute to the permeability of the polymer, especially if degradation in service acts to enlarge such features.

3. STRUCTURE AND DYNAMICS OF DEGRADED THERMOSET NETWORKS

3.1. Introduction

Below the glass transition temperature T_g in a variety of material types, individual particle motion takes place that characterizes a "cage jump" behavior. In this phenomenon, individual particle trajectories exhibit longer periods of localized thermal motion that are interrupted by rapid shifts in position, often in cooperative regions [72]. This behavior has been observed experimentally in colloidal suspensions [73] and numerically in bulk supercooled Lennard-Jones liquids [74, 75, 76, 77] and thermoplastic polymer chains [78, 79, 75]. This links to physical aging [75], diffusivity [73, 80], and effects on the glass transition [79]. However, no such analysis is known for model thermosets to determine the extent to which this behavior occurs in the presence of crosslink bonding, nor whether the occurrence or statistics of caged jump behavior are affected by network degradation that reduces the overall bonding.

Polymer networks may degrade via the destruction of chemical bonds. When a coating is exposed to the sun, high-energy photons cause the scission of bonds and eventually of small material fragments, which can be modeled as a stochastic process [8]. Since the removal of bonds from a thermoset network reduces the dynamic constraints applied to the immediately surrounding material, there is interest in the extent to which this process might affect the caging of beads in our coarse-grained model, and whether such a stochastic model requires modification given molecular dynamics data.

The gel point of bulk networks with 3-functional and 6-functional crosslinkers has been investigated previously [1]. Usually, the criterion is that an aggregated cluster (defined as a maximal set of beads linked by bond paths) spans one or more Cartesian dimensions in

the network. A useful approximation is that the size of the second-largest cluster is maximized, assuming this occurs immediately before it merges to form a giant component. Other definitions involve network percolation through one or more dimensions, or the spanning of the largest cluster. It was found that among these definitions, a 3-functional topology gels between $74.7 - 79.6\%$ conversion, and a 6-functional topology gels between $50.2 - 55.7\%$ conversion [1]. A topologically-dense network forms from clusters that aggregate fairly suddenly into a backbone (defined as the largest cluster in the network) that ideally comprises all constituent beads. Since not every bead is placed such that it is within bonding distance to enough neighbors, it is far more likely that the backbone consists of most, but not all, beads.

In this chapter, we examine possible rearrangement in crosslinked thermoset polymer networks prior to an after degradation in thin film models consisting of a featureless substrate, bulk region, and free surface. Model thermosets with different functionalities are constructed using a coarse-grained model and cooled above and below the glass transition. The particle trajectories are examined to determine the dynamics of the jump phenomena and compared to earlier thermoplastic and Lennard-Jones simulations. After network degradation imposed by the removal of bonds, we examine the resulting topology and make comparisons to the jump dynamics.

3.2. Model and setup

3.2.1. Potentials and bonding

We consider two different variants of a coarse-grained model thermoset system, as before. The two systems differ only in the crosslinker functionality and associated precursor bonding, which affect the density of the resulting three-dimensional network and the constraints under which such particles interact. These systems form crosslinked thermoset bead-and-spring networks, where beads interact via a Lennard-Jones potential, and may be additionally bonded together using a spring-like nonlinear elastic potential, also described below. These models have been examined in terms of adhesion, fracture, and other mechanical

properties as a generic model of a variety of polymeric systems with a single polymerization reaction [81, 82, 83].

All units in the model are scaled; σ is the length scale, ϵ the energy scale, and τ the time scale. As a result, temperature is measured in ϵ/k_B and time in $\sqrt{\sigma^2/\epsilon}$. Coarse-graining is applied to model a monomer group as a single bead with no charge at its surface. Beads that are not bonded together interact with a shifted Lennard-Jones potential $U(r)$ with a cutoff at $r = r_c$:

$$U(r) = \begin{cases} U_{\mathrm{LJ}}(r) - U_{\mathrm{LJ}}(r_c) & (r \leq r_c) \\ 0 & (r > r_c) \end{cases} \tag{3.1}$$

In this case,

$$U_{\mathrm{LJ}}(r) = 4\epsilon \left[\left(\frac{\sigma}{r}\right)^{12} - \left(\frac{\sigma}{r}\right)^{6} \right] \tag{3.2}$$

is the standard Lennard-Jones 12/6 potential. This potential combines a van der Waals long-tail attraction between beads with a short-range Pauli repulsion, with exponents chosen for computational efficiency. The cutoff is set at $r_c = 2.5\sigma$ since the potential dies off quickly at this range, consistent with other studies involving this potential.

Beads in the crosslinked systems that are bonded, either as precursors or during later crosslinking, have an interaction that is the sum of the purely repulsive portion of the Lennard-Jones potential (with a cutoff at $r = 2^{1/6}$ at the Lennard-Jones minimum) and a spring-like finite-extensible nonlinear elastic (FENE) potential:

$$U_{\mathrm{FENE}} = \begin{cases} -\frac{R_0^2 k}{2} \ln \left[1 - \left(\frac{r}{R_0}\right)^2 \right] & (r < R_0) \\ \infty & (r \geq R_0) \end{cases} \tag{3.3}$$

Here R_0 is the maximum bead separation and k acts as a spring constant that controls the bond strength, with $R_0 = 1.5\sigma$ and $k = 30\epsilon/\sigma^2$ [52]. The minimum of this bonded potential is at approximately $r = 0.961\sigma$.

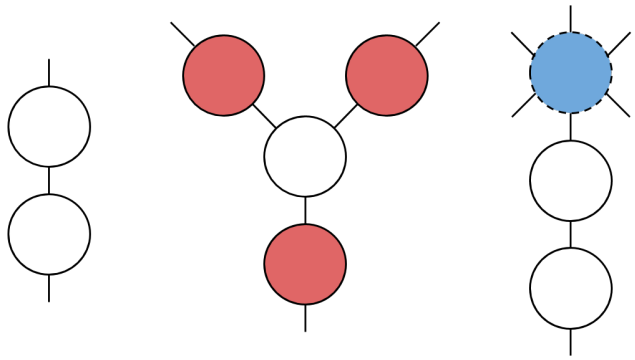

Figure 3.1. Network precursors: chain extender (left), 3-functional crosslinker (center), and 6-functional crosslinker with chain extender pre-bonded (right)

One type of precursor used is two-functional and acts as a chain extender, consisting of two beads bonded in a dimer formation. The second type, a crosslinker, is either 3-functional and consists of four beads arranged in a cluster, or is 6-functional and consists of three beads arranged in a line [84, 81]. The system consists of 11,424 monomer beads at stoichiometry, so there are no leftover beads that do not start as part of either a dimer or crosslinker molecule. Figure 3.1 shows the chain extender and crosslinkers. The 3-functional system consists of dimers and crosslinkers, in which the white beads of a chain extender are allowed to bond with the red beads of a crosslinker. The 6-functional system consists of dimers and crosslinkers, in which the white chain extender beads (including those pre-bonded within a crosslinker) are allowed to bond only with a blue crosslinker bead.

After initial random placement of precursor beads, a soft cosine potential is applied to gently remove any residual overlap, and each thermoset system is crosslinked by randomly linking dimers to crosslinker molecules if they are within bonding distance; this procedure takes place until at least 99% conversion is reached. As examined elsewhere [22], there is no guarantee of homogeneous crosslinking throughout the entire system, and regions where bond gaps exist are likely to occur, even in systems of this size. In particular, imperfections in the form of dangling ends and larger pendants are present in such networks both before and after gelation [1, 30, 85, 86].

Simulations are performed by integrating the Newtonian equations of motion for each bead using the LAMMPS software package [53] with timestep $\Delta t = 0.005\tau$. We generated five equivalent replicates of both crosslinked network types, each with a different random seed value for initialization, and verified that the resulting network topologies used subsequently are consistent and not dependent on a particular initial random particle arrangement.

3.2.2. Simulation box

Each network is set up in a simulation box with periodic boundary conditions in the x- and y-directions. At the lower z-boundary, we establish a fixed modified Lennard-Jones potential:

$$U_{\text{wall}}(r) = \begin{cases} U_{\text{LJ}\,93}(r) - U_{\text{LJ}\,93}(r_c) & (r \leq r_c) \\ 0 & (r > r_c) \end{cases} \tag{3.4}$$

Here

$$U_{\text{LJ}\,93}(r) = \epsilon \left[\frac{2}{15} \left(\frac{\sigma}{r} \right)^9 - \left(\frac{\sigma}{r} \right)^3 \right] \tag{3.5}$$

is the Lennard-Jones 9/3 potential. It is derived by integrating over a three-dimensional half lattice of standard Lennard-Jones particles, and is less repulsive than the original Lennard-Jones 12-6 potential used for unbonded bead interactions. This potential was examined by Abraham and Singh [87] and been used extensively to model the interaction between hard spheres and a soft wall. It mimics the behavior of an idealized featureless substrate.

We place the upper z-boundary sufficiently far from the collection of monomers and make it a reflective wall. Monomers that attempt to cross this wall have their velocity vector reflected, similar to billiard balls striking the bumper of the table. Because the wall is positioned far enough above the monomers, it does not play a role in the resulting dynamics after the system is fully prepared. After the subsequent cooling process (described below), this results in a free surface in the upper z-direction. Hence the system contains three zones of interest: the featureless substrate, the bulk, and the free surface. We investigate each in detail throughout our results.

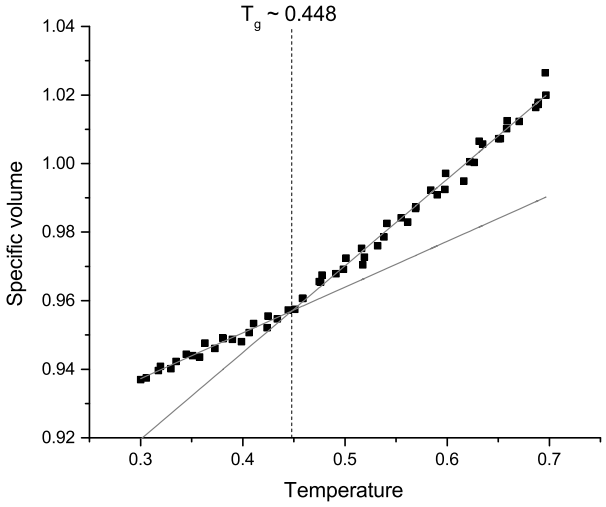

Figure 3.2. Specific volume of 3-functional thermoset during cooling, with linear least-squares fit indicating $T_g = 0.448$

3.2.3. Cooling and glass transition

To determine the glass transition temperature T_g of each resulting thermoset, we slowly cool the system at fixed volume using a Langevin thermostat ramp to $T = 0.2$ over a period of 5×10^6 timesteps. We compute the specific volume as a function of temperature; since the slope of this curve changes discontinuously at the glass transition, the intersection point of the resulting piecewise linear curve is interpolated to determine T_g, shown in Figures 3.2 and 3.3. We find that $T_g = 0.448$ for the 3-functional system and $T_g = 0.500$ for the 6-functional system. These values are consistent with earlier analysis of bulk thermosets with the same functionality [84].

After determining the glass transition temperature, we restart the simulation at $T = 1.0$ and cool the system. This method is a ramped cooling, where we apply a Langevin thermostat to decrease the temperature from $T = 1.0$ to one of several temperatures $T = 0.3, 0.35, 0.4, 0.45, 0.5, 0.55, 0.6$ to ensure values both below and above T_g for each of the functionality types. We then apply a new Langevin bath to hold the temperature at this final value for the remainder of the simulation. During the Langevin cooling and subsequent

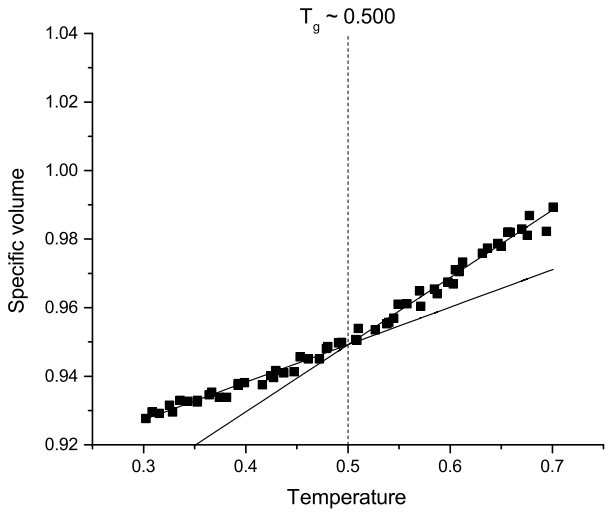

Figure 3.3. Specific volume of 6-functional thermoset during cooling, with linear least-squares fit indicating $T_g = 0.500$

temperature hold, we periodically zero the aggregate linear momentum every 100 timesteps in order to prevent drift. This is needed since the substrate is featureless and offers no resistance to thermal drift, but does not affect the relative velocities of any pair of beads. Initial testing indicated that this thermal drift occurs on timescales at least two orders of magnitude greater than the analysis intervals for which we examine particle dynamics, described below.

3.3. Jump detection

To determine the extent to which caging behavior can influence short-time particle mobility in these networks, we use a jump detection method similar to that of Helfferich et al [88, 89]. After cooling, the position of each bead is recorded at intervals of 20 timesteps. We partition the simulation time of 5×10^6 timesteps into window intervals of size $w = 2 \times 10^4$ timesteps each; hence each interval contains 1000 bead position samples, and there are 250 intervals in the simulation.

For a given fixed bead, let $r_\alpha(i, j)$ be the position component corresponding to the jth sampling point in the ith interval, where α is one of x, y, or z. We compute the average

position of the bead component-wise as

$$\overline{r}_\alpha(i) = \frac{1}{w}\sum_{j=1}^{w} r_\alpha(i,j). \tag{3.6}$$

We also compute the interval variance of the bead as

$$\sigma_\alpha^2(i) = \frac{1}{w}\sum_{j=1}^{w} \left[r_\alpha(i,j) - \overline{r}_\alpha(i)\right]^2 \tag{3.7}$$

where again α is one of the position components x, y, or z. The total variance is given as

$$\sigma^2(i) = \sqrt{(\sigma_x^2(i))^2 + (\sigma_y^2(i))^2 + (\sigma_z^2(i))^2}. \tag{3.8}$$

To avoid detecting small movements within the interval that are attributed solely to localized motion near a temporary equilibrium position, we say that a jump occurred in interval i if $\sigma^2(i)$ exceeds some nominal value. Other work involving thermoplastic systems of monomer chains uses the Lindemann criterion, which holds that a solid melts if bead displacement near equilibrium positions is on the order of one-tenth the nearest-neighor distance [90, 88]. Although a thermoset network cannot melt due to its tightly crosslinked structure, we appropriate this criterion for comparison to Lennard-Jones fluids and thermoplastics, and say that a jump has occurred when $\sigma^2(i) > 0.1$; that is, if the interval variance exceeds one-tenth the bead diameter within a single interval. Other jump criteria and thresholds have been used that find behavior that is qualitatively independent of the precise variance cutoff chosen [75, 91, 92].

When a jump occurs for a particular bead in interval i, we define the jump length to be $l(i) \equiv |\overline{r}(i+1) - \overline{r}(i-1)|$ using the average positions in the surrounding intervals. In case the jump occurs in the first or last interval of the simulation, we replace $i-1$ or $i+1$ with i, respectively.

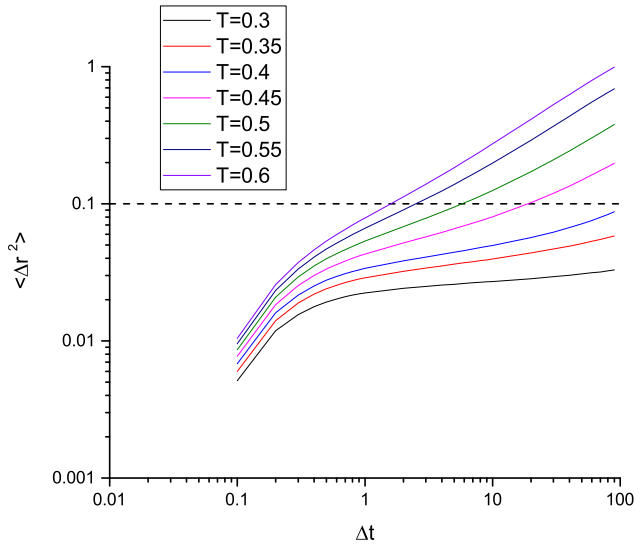

Figure 3.4. Mean-square displacement $\langle \Delta r^2 \rangle$ for 3-functional system in σ reduced units, with variance threshold (dashed line)

To better understand the dynamics of particles relative to the time scales of the detection process, we compute the mean-square displacement for both functionalities. To do so, 1000 particles are selected at random from each system. For values $0.1 < \Delta t < 100$, we average the displacement of those particles during the Langevin temperature hold where jump detection takes place. A duration $\Delta t = 100$ corresponds to the length of each jump detection interval. Figures 3.4 and 3.5 show these results at each temperature, with a dashed line indicating the variance cutoff from the detection algorithm. For temperatures below T_g, a smaller slope is more clearly defined. Further, the displacement curve at longer time scales is flatter in the more constrained 6-functional network. Notably, the well-defined intermediate plateau observed in thermoplastic simulations caused by chain entanglement is not evident in these thermoset systems.

3.4. Intact network

3.4.1. Jump rate

It is natural to assume that the dynamics of short-time bead motion in model thermoset systems might differ from that of bulk Lennard-Jones fluids or thermoplastics due to the added constraints imposed by network formation. In particular, while Lennard-Jones

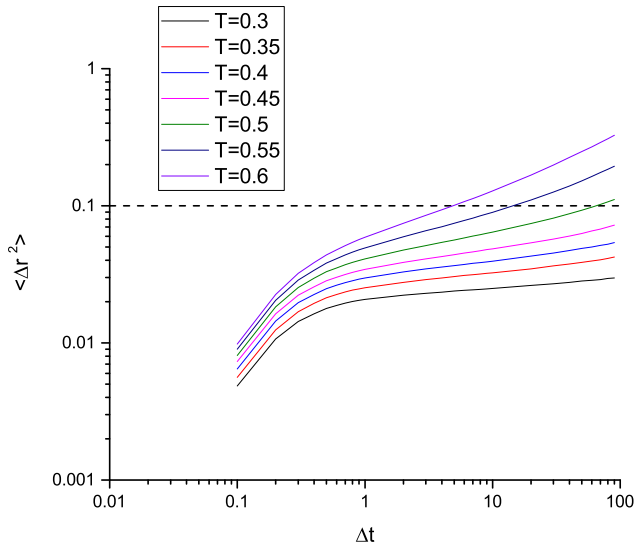

Figure 3.5. Mean-square displacement $\langle \Delta r^2 \rangle$ for 6-functional system in σ reduced units, with variance threshold (dashed line)

fluids exhibit short-time ballistic motion and longer-term diffusive regimes, bulk thermoplastics exhibit an intermediate plateau regime where chain bonding and reptation impede diffusion [88]. The cages formed by neighbors (whether bonded to a given bead or not) set the stage for jump motion behavior. Cages in thermosets are even more prevalent due to the much higher bonding density and lack of chain motion.

It is instructive to investigate the dependence of jump dynamics on the z-position of the monomer (hereafter referred to as the depth), since our three-zone system imposes heterogeneous constraints that differ throughout. In particular, behavior within the network bulk might differ from that near the substrate or free surface. We slice the simulation box into 1σ-thick slices in the z-direction and average the number of jumps per particle within each slice, scaled by the total number of intervals used in the analysis. We denote this average jump rate by $R(z)$, where z is the lower integer bound within a given slice. For example, a value $R(2) = 0.1$ means that in the slice $2\sigma \leq z \leq 3\sigma$, a particle in this slice jumped, on average, once every ten intervals during the simulation analysis period. Figures 3.6 and 3.7 show the depth dependence of $R(z)$ for both functionalities; note the logarithmic scale used.

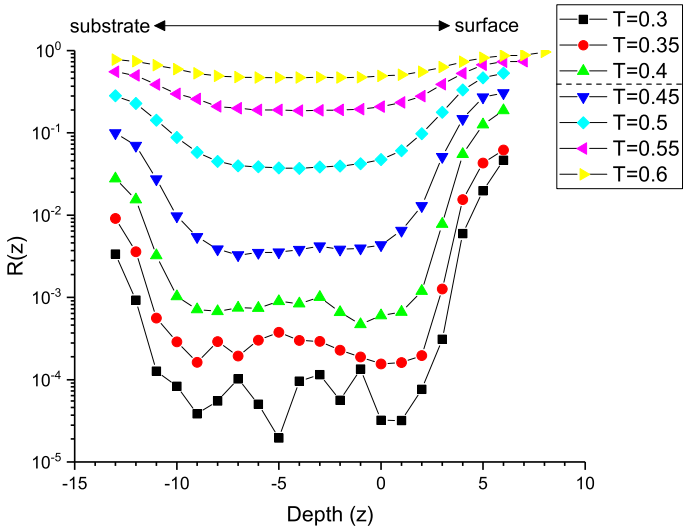

Figure 3.6. Jump rate $R(z)$ as a function of depth for 3-functional system (in σ reduced units), with dotted line indicating T_g

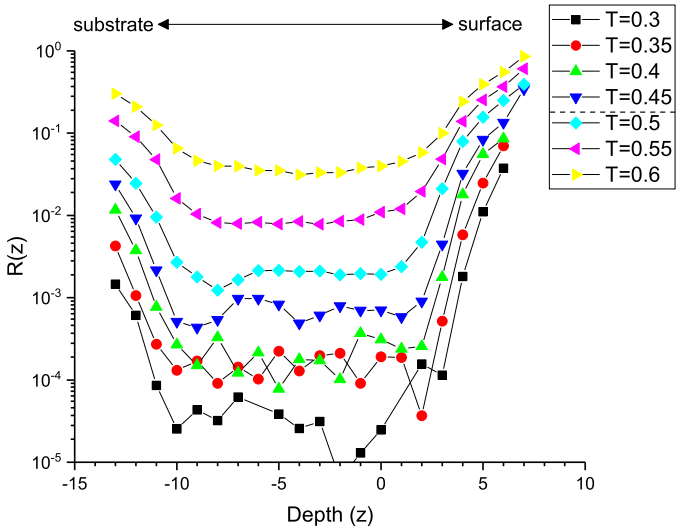

Figure 3.7. Jump rate $R(z)$ as a function of depth for 6-functional system (in σ reduced units), with dotted line indicating T_g

The jump rate $R(z)$ suggests three distinct regions whose behavior differs by up to two orders of magnitude, indicating a natural but continuous split in jump behavior between the substrate, bulk, and free surface zones of the simulation box. We use an estimate of the split points to define these three zones for subsequent analysis. This determination is clear at lower temperatures, but less obvious above T_g.

In the bulk region, behavior below the glass transition is nearly identical for both the systems, suggesting that the constraints of the 3-functional crosslinking density are sufficient to limit the jump rate, and that additional crosslinking density in the 6-functional system does not appreciably affect this behavior. Above the glass transition, apparent jump behavior increases substantially as thermal activity dominates both the jump detection process and the overall motion of beads in this region. In the case of the 3-functional system, the increased thermal activity is sufficient to nearly eliminate the effects of zone position altogether at high temperatures. This behavior is also consistent with determination primarily by Lennard-Jones forces acting between beads.

In the substrate and free surface regions, jump rate is also temperature dependent, with higher rates occurring at the surface than at the substrate for any given temperature. Since the free surface offers no resistance to lateral particle motion and crosslinking density is less here, beads are free to move more easily and rapidly. That the surface jump rate shows less temperature dependence both above and below the glass transition in the 6-functional system (especially compared to the 3-functional system) suggests that the effects of crosslinking density are more important here. This difference in behavior is not present in the substrate zone.

A more global way to examine the jump rate behavior and compare to thermoplastic models uses the approach of Helfferich [88]:

$$\nu(T) = \frac{J(T)}{Nt_m} \tag{3.9}$$

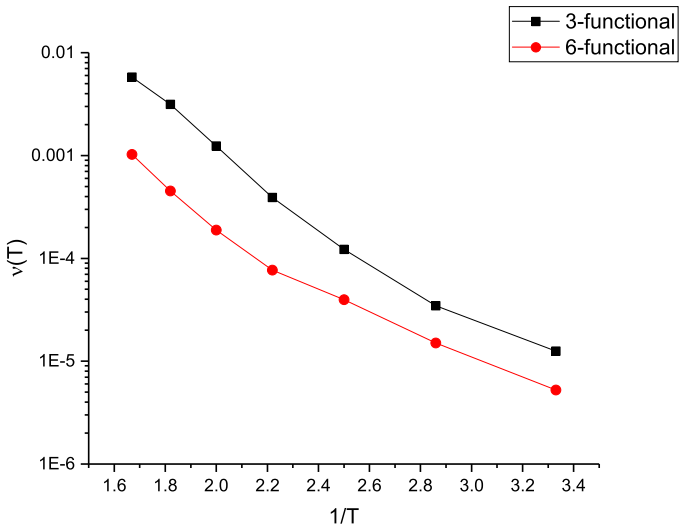

Figure 3.8. Jump rate $\nu(T)$ for 3-functional and 6-functional systems

Here $J(T)$ is the total number of jumps measured in the simulation, N is the total number of monomers, and t_m is the total simulation time. The authors in [88] found that in thermoplastic chains at low temperatures, $\nu(T)$ followed an Arrhenius decay of the form $\nu(T) \sim \exp(-1/T)$; after additional filtering of certain types of jumps, the resulting behavior followed the Vogel-Fulcher-Tamman equation. It was noted that non-filtered jumps may include those which include correlated forward-backward motion that does not contribute to overall network relaxation, and only a small temperature range was examined. Figure 3.8 shows a logarithmic plot of $\nu(T)$. The simulations here are performed over a much wider temperature range above and below T_g and do not apply the filtering used in [88]. The behavior does, however, exhibit a decay in $1/T$. The 3-functional system jump rate is of the same order as found in bulk thermoplastic chains, while the more densely restricted 6-functional system rate is substantially lower.

3.4.2. Jump length

We next compute the jump length $l(i)$ for each monomer in each interval i. Aggregating these values, we denote by $L(z)$ the average jump length of beads contained in the

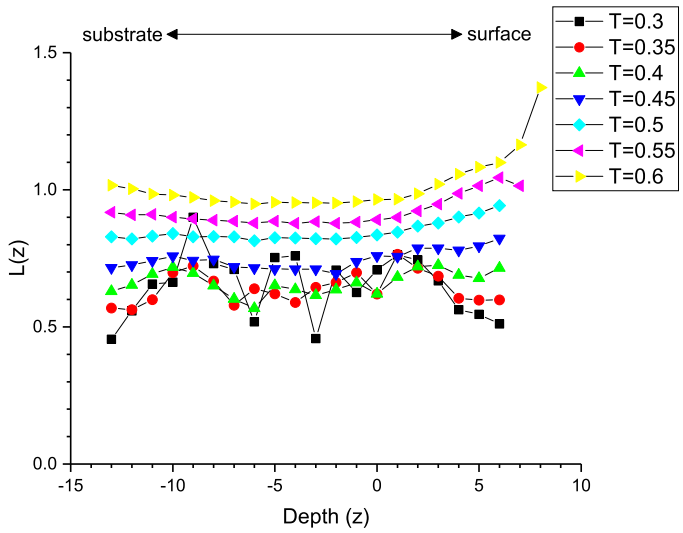

Figure 3.9. Average jump length $L(z)$ as a function of depth for 3-functional system (in σ reduced units)

depth slice z, averaged by the number of monomers in the slice. Figures 3.9 and 3.10 show the depth dependence of $L(z)$ for the 3-functional and 6-functional systems.

There is increased noise in the overall jump length plots at lower temperatures, due primarily to the far lower jump rate making the averages less uniform. However, of note is that the average jump length shows little overall dependence on zone position at lower temperatures; this is to be expected, since crosslinking implies substantial constraints on motion. However, there is a small increasing tail at the free surface that is especially visible at higher temperatures where thermal activity becomes apparent. This is more evident in the 3-functional system than the denser 6-functional, and is also consistent with the lower T_g materials exhibit near a free surface.

When comparing the 3-functional and 6-functional systems at the same temperatures, the average length increases as crosslinking functionality decreases, with a nearly 25% increase in average jump length between 3-functional and 6-functional systems at $T = 0.6$. Below the glass transition, the two functionality types result in average jump lengths that are nearly identical, spanning a range of about 0.5-0.7σ.

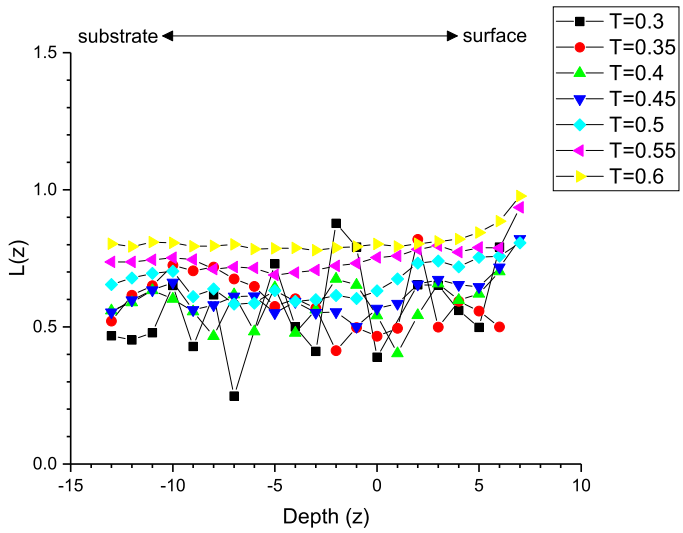

Figure 3.10. Average jump length $L(z)$ as a function of depth for 6-functional system (in σ reduced units)

It is natural to ask whether the distribution of jump lengths within a particular zone is normally distributed, since the frequency of jumps is tightly related to the relative degrees of freedom of monomers based on their zone. The distribution for each temperature is plotted in Figure 3.11 for the 3-functional system and in Figure 3.12 for the 6-functional system. An exponential long tail exists in both cases at higher temperatures, but bond constraints are evident for shorter jump lengths.

There is both a clear overall dependence on temperature in the jump length distribution, as well as a plateau behavior exhibited at short lengths that depends on the glass transition. Below the glass transition in both the 3-functional and 6-functional systems, jumps up to 1.0σ in length have nearly equal probability, indicating the extent of caged behavior that is not affected by crosslinking density or temperature in this regime. This correlates well to an average bond length of nearly 0.97σ.

Above the glass transition, there is a more smooth distribution that, at longer jump lengths, is consistent with the distribution below the glass transition. The extent of the long-range tail differs at high temperatures between functionality types, but such behavior at lower temperatures shows remarkably little dependence on functionality. Examination of

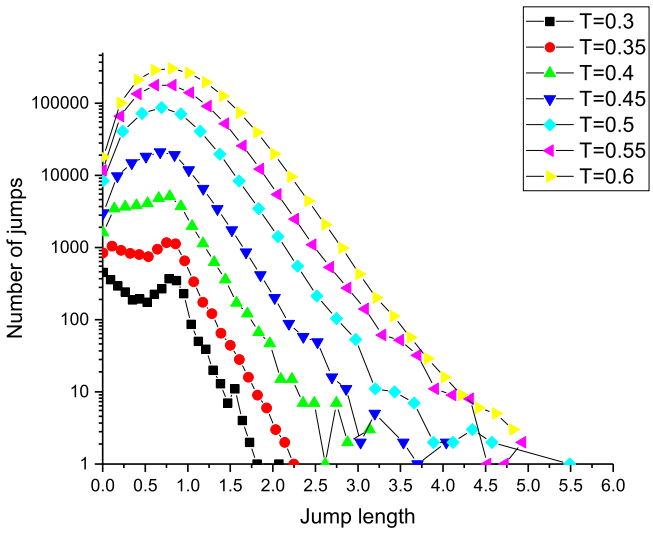

Figure 3.11. Jump length distribution for 3-functional system (in σ reduced units)

the long jump behavior shown by the distribution tail at higher temperatures was found to correspond to small mobile fragments consisting of only one or two free beads not connected to the bulk of the network.

3.4.3. Bead connectivity

In these coarse-grained thermosets, beads are bonded differently. To examine the effect of crosslinking and bonds on jump dynamics, we consider the fraction of jumping beads with various bond numbers.

In an idealized complete 3-functional network, every bead has either two bonds (chain extenders) or three bonds (crosslinker centers). In an idealized complete 6-functional network, every bead has either two bonds (chain extenders) or six bonds (crosslinker centers). However, since there is no guarantee of complete conversion in this model (or in any polymeric system in practice), it is natural to wonder if jump behavior depends on the extent to which bonds, or lack thereof, affect jump constraints.

The leftmost data column of Tables 3.1 and 3.2 list the fraction of beads in the 3-functional and 6-functional systems (respectively) of each bond count. In the case of the 3-functional system, at least 2.3% of beads are incompletely bonded; there may be crosslinker

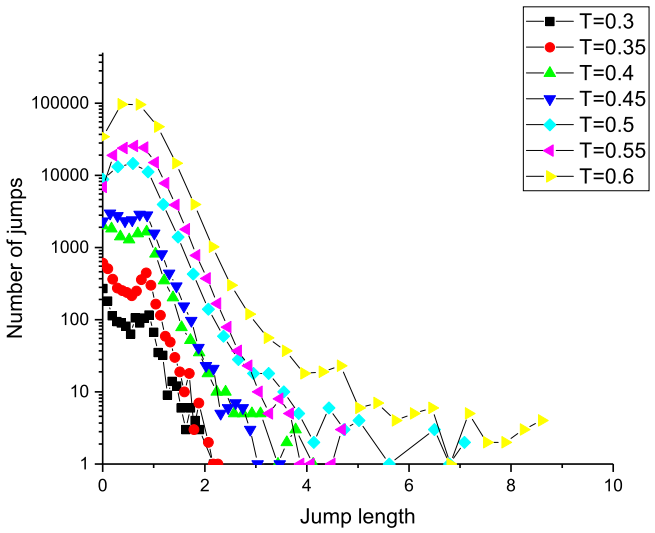

Figure 3.12. Jump length distribution for 6-functional system (in σ reduced units)

centers with only two bonds that are also not fully bonded. In the 6-functional system, at least 3.6% of beads are incompletely bonded, with similar reasoning.

The remaining data columns of the tables show, for each temperature, the fraction of beads of each bond count that jump in at least one interval, ignoring in the total any beads in the system that do not jump at all. If the jump behavior were to be totally independent of bond density, these values would match those of the total bead count in the first column.

In the 3-functional system, the bond count distribution is extremely close to the overall bead distribution; however, below the glass transition there is a trend toward higher jump likelihood in beads with fewer bonds. Since the overall jump rate rises so rapidly above the glass transition, it is expected that the bond count distribution approaches the ideal case since all beads effectively have more freedom to move at higher temperatures.

In the 6-functional system, the dependence on bond count is far more apparent. While nearly 13% of all beads in the system are six-bonded, the fraction of such beads that jump is an order of magnitude lower below the glass transition (and not much higher above the glass transition). Similarly, beads with only a single bond jump far more frequently than the overall system distribution, often to a remarkable extent.

Table 3.1. Bond distribution of all beads in the 3-functional system (left column) and of all beads that jumped in any interval (right columns)

	All beads	Jumping beads						
		$T = 0.3$	$T = 0.35$	$T = 0.4$	$T = 0.45$	$T = 0.5$	$T = 0.55$	$T = 0.6$
1 bond	0.023	0.027	0.042	0.033	0.028	0.024	0.023	0.023
2 bonds	0.834	0.868	0.835	0.849	0.849	0.842	0.834	0.834
3 bonds	0.143	0.104	0.123	0.118	0.123	0.133	0.143	0.143

Table 3.2. Bond distribution of all beads in the 6-functional system (left column) and of all beads that jumped in any interval (right columns)

	All beads	Jumping beads						
		$T = 0.3$	$T = 0.35$	$T = 0.4$	$T = 0.45$	$T = 0.5$	$T = 0.55$	$T = 0.6$
1 bond	0.021	0.163	0.107	0.083	0.066	0.049	0.036	0.026
2 bonds	0.837	0.830	0.885	0.902	0.915	0.925	0.938	0.932
3 bonds	0.001	0.007	0.000	0.003	0.001	0.002	0.000	0.001
4 bonds	0.004	0.000	0.000	0.001	0.000	0.003	0.002	0.003
5 bonds	0.010	0.000	0.002	0.004	0.005	0.004	0.003	0.004
6 bonds	0.128	0.000	0.005	0.007	0.012	0.018	0.020	0.034

3.5. Degraded network

Because networks are formed using precursors (chain extenders and crosslinkers) that are already bonded, it should not be expected that the distribution of small fragments during degradation should simply reverse that of the crosslinking process. Degradation can produce single-bead fragments that are smaller than the dimer precursor used to form the 3-functional and 6-functional networks. This suggests that a study of fragment distribution in degraded networks is nontrivial.

3.5.1. Bond removal algorithms

Bond removal is performed after each system is crosslinked and cooled, but immediately before equilibration and jump analysis. We consider two algorithmic approaches to gradual network bond destruction. In each case, we use five independent realizations of the 3-functional and 6-functional networks with different random seeds to verify that the network topology is consistent.

The first method is commonly used in LAMMPS molecular dynamics simulations. Each bead that contains at least one bond to a neighbor identifies the longest such bond (by considering bead center distances) and, if the neighboring bead makes a similar identification, the bond is marked as a candidate. Each candidate bond is then removed with some probability. This procedure is iterated until enough bonds are removed to reach a desired conversion. This algorithm permits each bead to be part of at most one bond removal. After removal, the system continues to equilibrate at its cooled temperature. This is similar to a physical process where the most strained and "fragile" bond is broken first.

The second method is purely stochastic, and is used only for network topology and cluster analysis for comparison to the LAMMPS algorithm. In this method, we choose a bead at random and, if it is bonded to a neighbor, choose a bond at random to remove. We iterate this process until conversion is reduced to the desired level.

3.5.2. Network structure

The network backbone is defined as the largest connected cluster in the system. This is determined by using a depth-first graph search algorithm to partition the system into spanning trees, which we identify as clusters [93]. Figure 3.13 shows the fraction of beads in the network backbone for representative replicates of the 3-functional and 6-functional systems during the stochastic degradation process. This process is done at the same high temperature used for the initial crosslinking process during system preparation. There were no appreciable differences between any of the replicates, nor between the stochastic method and LAMMPS algorithm. Conversion is computed as the fraction of bonds in the network relative to the maximal number possible.

As expected, the backbone breaks down more quickly in the 3-functional network due to the lower crosslinking density afforded by the crosslinker functionality than in the 6-functional network. To identify the degraded equivalent of the gel point more quantitatively, we use two independent criteria. The first criterion identifies the degraded gel point as the conversion where the size of the second-largest cluster is maximized. The second criterion

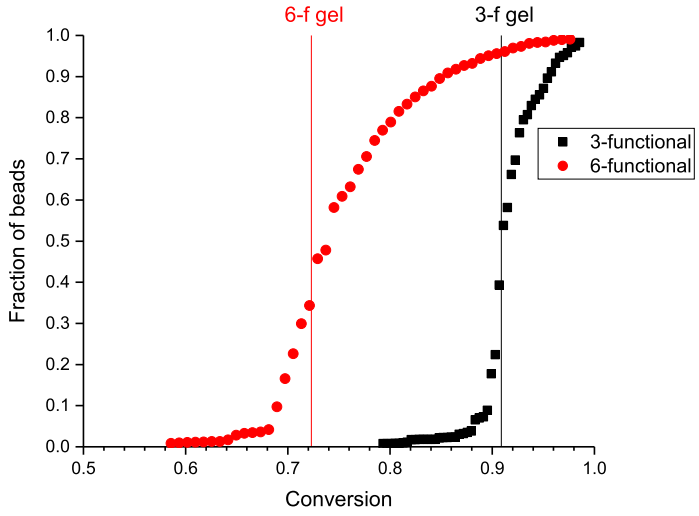

Figure 3.13. Fraction of beads in backbone by conversion

Table 3.3. Comparison of bulk [1] gel point and film degraded gel point by network type; criterion 1 requires the maximization of the second largest-cluster, and criterion 2 requires that the network span the simulation box

Network type	Bulk gel average	Criterion 1	Criterion 2
3-functional	0.770	0.909	0.894
6-functional	0.525	0.723	0.712

identifies the degraded gel point as the conversion when the network no longer spans the simulation box in all periodic Cartesian directions. Table 3.3 shows the degraded gel point for each of our thin film systems using these criteria, and compares them to the bulk gel point averages computed in [1] that used fully-periodic systems.

Earlier work on hydrogels gives a prediction of the conversion required to reach the degraded gel point in a bulk network [94]. The theory predicts that this occurs at a conversion $1/\sqrt{N-1}$ for a bulk hydrogel network where each bead has an average of N bonding sites. In our non-bulk model films, this predicts a degraded gel point for the 3-functional network of 0.935 conversion, and 0.798 conversion for the 6-functional network. Our observed results are slightly lower in both cases, but the theory is notably far more accurate to our results than a simple comparison to the bulk computations in [1] for the "standard" gel point measured during the crosslinking process.

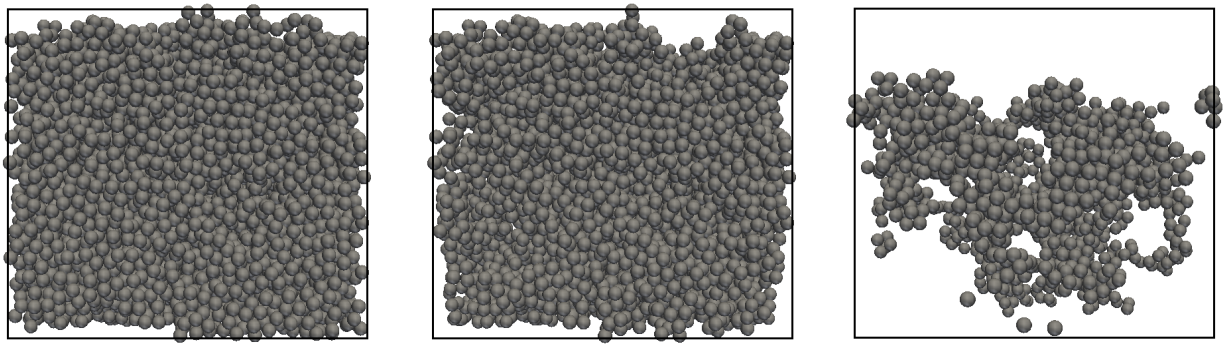

Figure 3.14. Beads in 3-functional backbone during degradation: slightly above gel (93% conversion, left), near gel point (91% conversion, center), and slightly below gel (89% conversion, right)

The gel points for both functionality types in these thin-film models are far higher than in the equivalent bulk systems. In bulk system analysis, periodic boundaries in all three dimensions allow for faster aggregation of otherwise distant clusters, and the presence of two planar surfaces means there are fewer potential bonding regions. During the degradation process, fewer bonds need to be broken to cause the rapid breakdown of the backbone.

It is instructive to visualize the degradation process near the gel point, since the network breaks down rapidly over a short conversion range. Figures 3.14 and 3.15 show the beads comprising the backbone slightly above, near, and slightly below the gel point conversion for the 3-functional and 6-functional networks at high temperature prior to cooling. Each simulation box is periodic horizontally, but not vertically. The substrate is at the bottom, with the free surface at the top.

We are also interested in the distribution of small fragment clusters. These are small sol regions that would be likely candidates for evaporative removal or leaching in the presence of moisture in the environment. Table 3.4 shows the fraction of beads in such fragments at the gel point.

In the 3-functional network, only a small portion of the network is in small fragments due to the high conversion at the gel point. However, in the 6-functional network where the gel point is much lower, a significant fraction of the network (nearly 10%) is degraded into

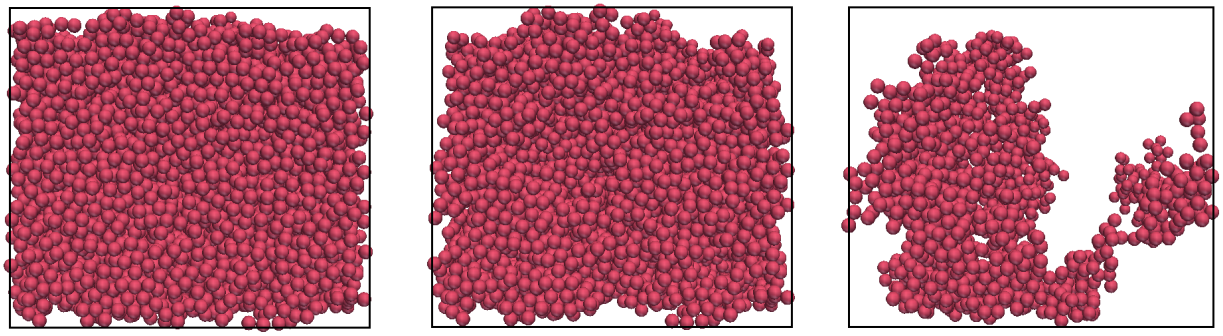

Figure 3.15. Beads in 6-functional backbone during degradation: slightly above gel (80% conversion, left), near gel point (74% conversion, center), and slightly below gel (68% conversion, right)

Table 3.4. Fraction of beads in small fragments at the gel point for each network functionality type

Beads in fragment	3-functional	6-functional
≤ 3	0.0157	0.0917
≤ 2	0.0119	0.0932
1	0.0077	0.0654

small clusters that could leach out. The distribution of beads in small clusters is similar in the 6-functional network due to the larger number of bonds per bead, on average. It is easier for larger fragments in the 3-functional network to break free due to the lower average bond density.

To show the evolution of these clusters during the degradation process, Figure 3.16 shows the fraction of beads in clusters of 3 beads or fewer as a function of degraded conversion. Since the results were nearly identical for all independent replicates, only one such replicate is shown for each functionality type.

Unlike the backbone, which exhibits a sharp breakdown at the gel point, the distribution of small clusters changes continuously due to the stochastic nature of the bond removal process. Bulk properties like adhesion, permeability, and mechanical durability depend heavily on the structure of the network remaining intact. However, other local properties like color and gloss depend on the average measured over a substantial area, and are consistent with a slower fragment loss.

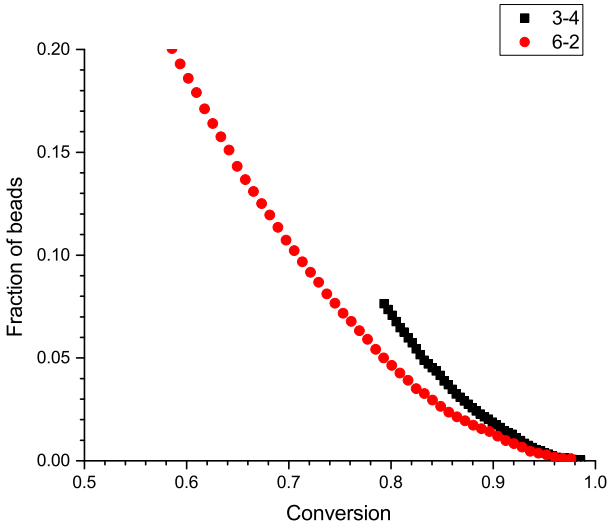

Figure 3.16. Fraction of beads in clusters of 3 beads or fewer at varying degraded conversion

Figures 3.17, 3.18 and 3.19 break down the fragment distribution into those fragments with exactly three, two, and one bead, respectively. The rate of single bead and 2-cluster formation initially proceeds identically regardless of crosslinker functionality, indicating these arise primarily from chain extenders. For the 3-functional network, all small clusters begin forming simultaneously, with the rates diverging at the gel point. This behavior is not exhibited by the more densely-formed 6-functional network. In this network, the larger 3-cluster emergence coincides with the gel point.

These results confirm that little degradation is required before volatile single beads emerge in a manner independent of the crosslinker functionality, caused by the common 2-functional dimer. The distribution of fragments larger than a single bead depends highly on the structure of the crosslinking, however, confirming that dense crosslinking helps to avoid material leaching.

3.5.3. Jump rate

In order to examine the effects of degradation on jump dynamics, intact 3-functional and 6-functional networks cooled to temperatures $T = 0.3$, 0.4, 0.5, and 0.6 undergo the LAMMPS semi-stochastic bond scission algorithm until the networks are degraded to the

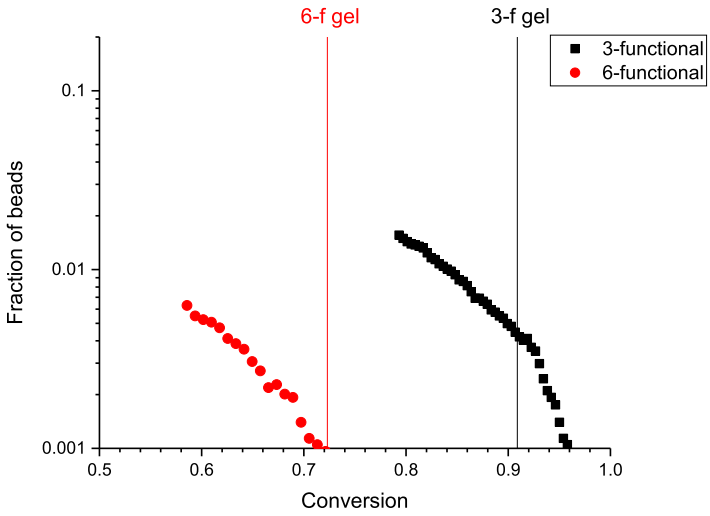

Figure 3.17. Fraction of beads in clusters of exactly three beads at varying degraded conversion

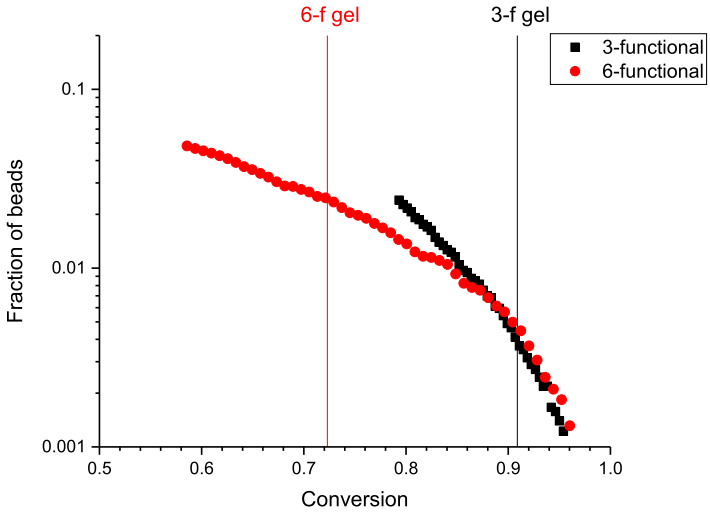

Figure 3.18. Fraction of beads in clusters of exactly two beads at varying degraded conversion

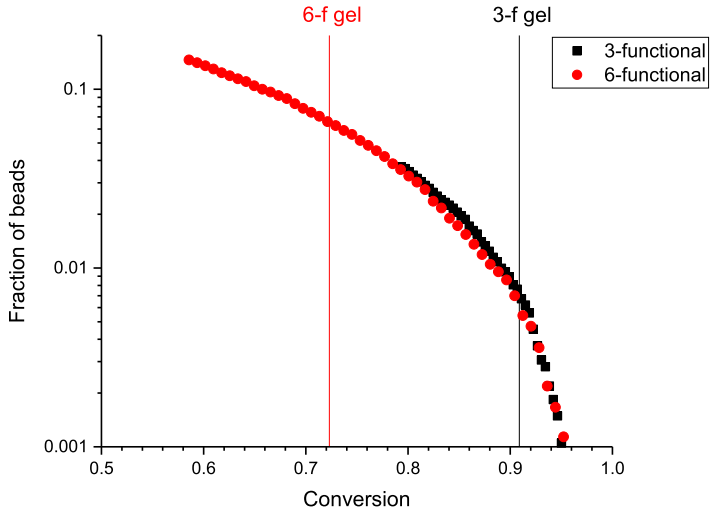

Figure 3.19. Fraction of single beads at varying degraded conversion

corresponding degraded gel point from Table 3.3. The observed fragment distribution indicates the resulting network is more complex than a simple Lennard-Jones fluid, but is not expected to retain gel-like properties. We then run the same bond detection and analysis processes used for the intact networks. This provides directly comparable results at high gel conversion and degradation to the sol-gel transition.

The jump rate $R(z)$ as a function of depth is shown for the degraded 3-functional and 6-functional systems in Figures 3.20 and 3.21, respectively.

The qualitative behavior of $R(z)$ is similar between these degraded networks and the intact networks in Figures 3.6 and 3.7. However, the degraded rates are markedly greater than the corresponding intact networks. This indicates a greater propensity for short-time subdiffusive motion corresponding to fewer bond restrictions. This effect is far more pronounced in the 6-functional system, where the gel point is much lower than the 3-functional system. However, the results indicate that below the glass transition, bead motion is still extremely limited.

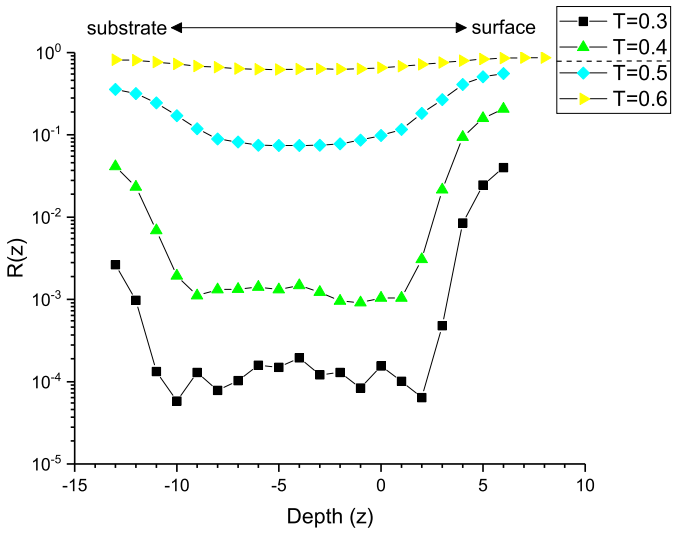

Figure 3.20. Jump rate $R(z)$ as a function of depth for degraded 3-functional system (in σ reduced units), with dotted line indicating T_g

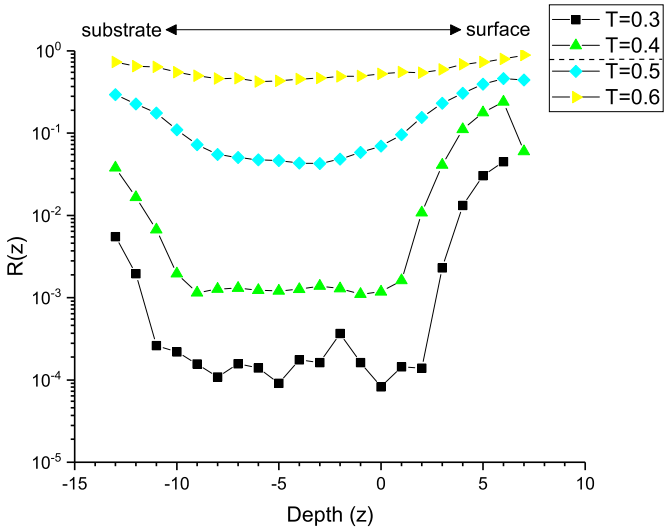

Figure 3.21. Jump rate $R(z)$ as a function of depth for degraded 6-functional system (in σ reduced units), with dotted line indicating T_g

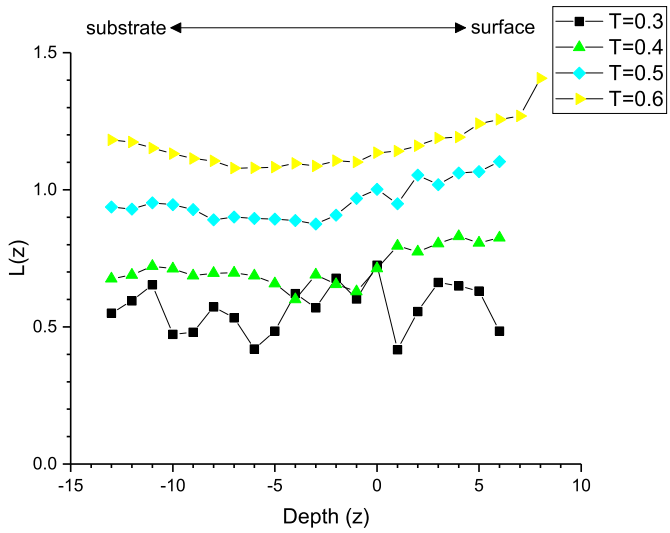

Figure 3.22. Average jump length $L(z)$ as a function of depth for degraded 3-functional system (in σ reduced units)

3.5.4. Jump length

Also of interest is the length. The average jump length $L(z)$ by depth is shown in Figures 3.22 and 3.23 for the networks degraded to the gel point.

Compared to the corresponding data for the intact networks in Figures 3.9 and 3.10, the degraded average jump length is greater in both network types, primarily due to the presence of smaller mobile fragments that are not constrained by the backbone structure after the bond scission process. These beads are part of separated fragments that are distributed throughout the network. The corresponding jump length distributions are shown in Figures 3.24 and 3.25.

The effects of mobile fragments are evident in the longer distribution tail in both 3-functional and 6-functional networks, while the flat region for lengths below the nearest-neighbor distance persists below the glass transition, albeit with greater frequency due to the higher jump rate after degradation.

Even near the free surface in the degraded network, it is unlikely that a bead will move fully to a neighboring position below the glass transition. Reducing the cage constraints

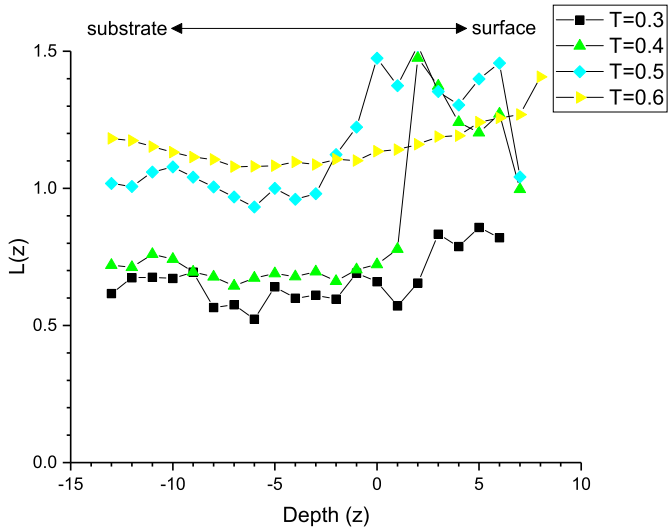

Figure 3.23. Average jump length $L(z)$ as a function of depth for degraded 6-functional system (in σ reduced units)

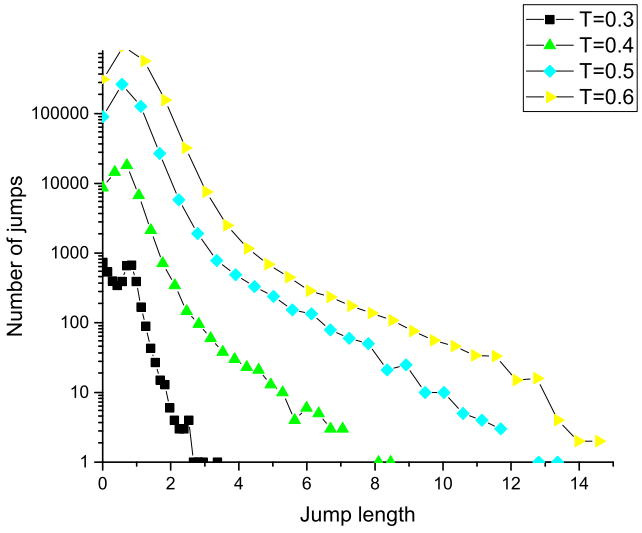

Figure 3.24. Jump length distribution for degraded 3-functional system (in σ reduced units)

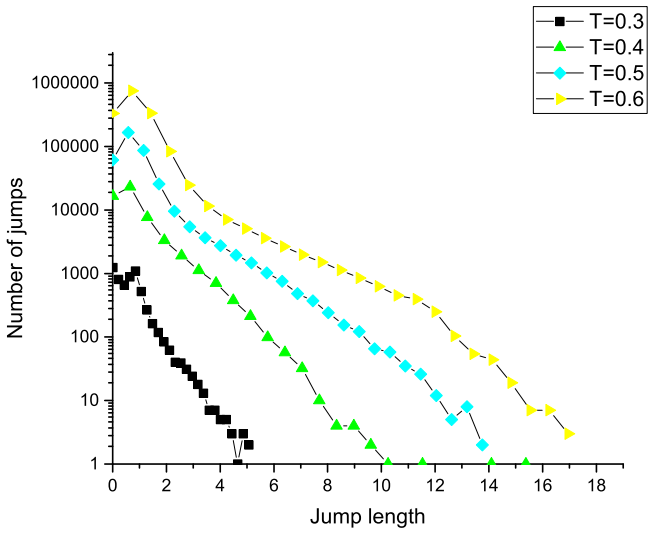

Figure 3.25. Jump length distribution for degraded 6-functional system (in σ reduced units)

through bond scission is therefore not enough to permit substantial motion. If a fragment were to be removed from the network entirely below the glass transition, the vacancy is unlikely to be filled. Above T_g, the relaxation of bond constraints couples with thermal activity to allow for higher jump lengths.

To illustrate the local behavior in a region of bond scission, example instances of the 3-functional and 6-functional network were cooled to $T = 0.3$ and $T = 0.6$, after which all bonds within a small region near the free surface were removed. The average displacement per timestep of the beads within the region were examined before and after bond scission. Results are shown in Figures 3.26 and 3.27.

Even under the rather extreme condition of full bond removal, network response is limited to the time period immediately surrounding the removal event as beads immediately find local equilibrium positions. The extent of this response is limited to a length much smaller than the nearest-neighbor bead distance.

3.6. Conclusions

We have investigated the caged jump dynamics of model thermosets before and after stochastic bond scission, where coarse-grained particles exhibit localized thermal motion

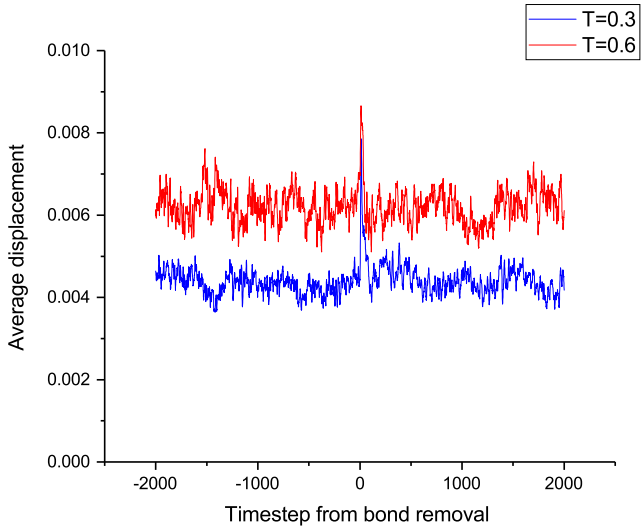

Figure 3.26. Average displacement per timestep near bond removal event in 3-functional network, at temperatures $T = 0.3$ (lower) and $T = 0.6$ (upper)

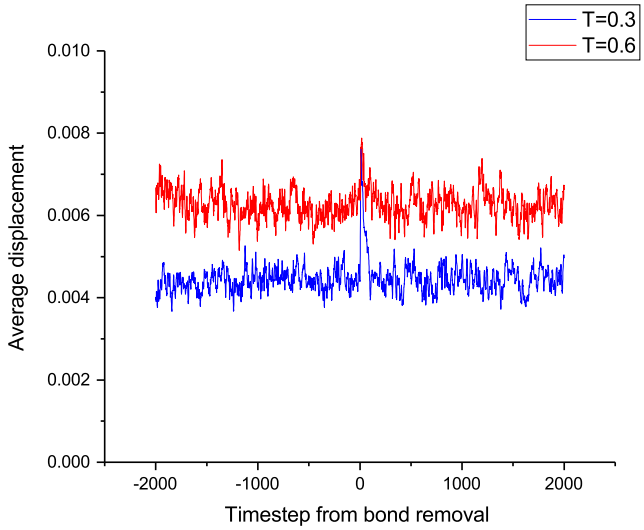

Figure 3.27. Average displacement per timestep near bond removal event in 6-functional network, at temperatures $T = 0.3$ (lower) and $T = 0.6$ (upper)

within neighbor cages that is interrupted by rapid jump motion out of the cage. This behavior has been previously observed numerically in simulations of Lennard-Jones fluids and entangled thermoplastic chains, and experimentally in colloidal fluids. Two model thermosets, used in other work to examine a variety of crosslinked polymer network phenomena, were examined: a 3-functional and 6-functional densely-crosslinked network in thin-film configurations with a free surface and substrate.

After crosslinking to high conversion, each network was cooled to one of several temperatures ranging from the glassy to the rubbery state in order to observe the effects of thermal activity and the glass transition. Dynamical jump behavior similar to fluid and thermoplastic systems was observed despite the constraints imposed by the dense crosslinking process. This behavior was observed to depend heavily on temperature, and was particularly evident through the glass transition. The propensity of beads to jump is orders of magnitude higher near the free surface and substrate than in the bulk region. Bulk jump behavior is relatively independent of crosslinker functionality, but is more evident near the surface and substrate. The distribution of jump lengths is equiprobable for lengths below the nearest-neighbor distance, but shows an exponential tail at longer lengths.

An analysis of network topology was conducted, examining both the backbone behavior of the model thin films and the distribution of volatile fragments formed during stochastic bond scission, modeling the effects of damage by radiation or hydrolysis. The degraded gel point in the thin film case was observed to be far higher than the measured gel point of equivalent bulk networks studied elsewhere, with a non-trivial fraction of the network present as single particles or small fragments that may be at risk of leaching during environmental exposure. The network backbone begins to fail with even small levels of bond scission.

The jump behavior of networks at the degradation gel point was examined. Compared to the intact systems, degradation behavior was seen to increase both the frequency of neighbor cage jumps and the lengths of such jumps. Small fragments formed during degradation are particularly susceptible to jumps due to the lack of connectivity to the network

backbone. However, jump behavior in the bulk region of the networks is still extremely low, suggesting that particles are generally unable to rearrange to the extent needed to fill damaged regions that may form in service.

In the case of coating systems used in the laboratory or in the field, this suggests that the caged motion observed in fluids and thermoplastics is present even in densely-crosslinked materials, offering a link to previous work. Further, material degradation enhances this behavior and confirms that volatile fragments formed during hydrolysis or exposure to radiation are highly mobile even at the extremely short time scales considered here, and are likely candidates to be quickly leached from the material. Constrained motion due to bonding of the remaining network is unlikely to allow such vacated regions to be filled by rearrangement of the network.

4. STRAIN CONCENTRATIONS IN COATINGS OVER JOINTS AND AROUND RIVETS: FINITE-ELEMENT MODELS

4.1. Introduction

It is common to fill or seal joints and gaps with grouts, sealants, caulks, and similar materials, and to paint over the result. One has only to look around to see that painting over the gaps around screws, bolts, rivets, and other fasteners is ubiquitous. The many types of traditional joints studied in the literature, for example, single and double lap joints, are often painted in practice.

Adhesive bonding has seen continued interest in many industries and areas of study, as noted by [96]. Joining materials adhesively reduces the need for reliance on precise machining associated with rivets and other mechanical joints, while helping to distribute loads and stresses across a broader joint area. Adhesive bonding can save weight over a large application and can help to control corrosion of the underlying substrate.

A quick glance at an aged coated gap system on an automobile or within a building indicates that temperature cycling, flexing, and general environmental exposure pose long-term hazards. The process of using a coated and sealed gap presents inherent difficulties for field service. Thermal expansion and contraction of adherents introduces stresses both within the sealed gap and to coatings painted on top. Mechanical flexing abounds in aerospace and automotive applications due to frequent movement and vibrations which force the gap open and closed and introduce tensile and compressive strains that may cause adhesive or cohesive failure in a number of locations over time. Taken together, this means an understanding of

Work in this chapter was completed by the author with assistance from collaborator S.G. Croll, in a paper to appear [95].

the presence of strain within a sealed and coated gap or joint is essential for the design of systems intended for long service life.

Much research in the literature has been devoted to the analysis of stress and strain distributions; such work, as by [10], has primarily focused on single and double lap joints under tension and, to a lesser extent, bending loads. Work by [11] has been conducted to determine the role of gaps in stress concentrations. Relatively little attention, however, has been paid to other types of joints like butt joints, presumably because of the geometric simplicity. At the other extreme, the geometric complexity of a traditional rivet precludes much study in favor of lap joints where loads can be more easily controlled and experimental setups more easily machined. It is recognized and understood that coatings that must stretch over joints often fail due to large strains, but has proved difficult to find quantitative analysis of the geometry that is directly relevant. However, inexpensive high-powered computing now allows for much more complicated models to study a large array of cases in structural, electrical, and hydrodynamic fields that had been too difficult in the past.

The study of adhesion and joint strength via finite-element analysis (FEA) is a fairly recent development, due in no small part to a growing understanding of the role of meshing and stress singularities on failure regimes of models under study. Recent work of [10] suggests that an analysis of peak stress singularities across similarly-meshed models can provide useful information about relative strengths of adhesive-adherend joints. Several techniques exist to model the progression of failures like cracks through an FEA model over time. Cohesive zone modeling, thoroughly reviewed by [97], and peridynamics, whose role in FEA was investigated by [98], are the most common methods. However, instead assuming perfect adhesion has the advantage of analytical simplicity and no a priori knowledge of areas where failure is expected to occur, as noted by [99]. Essentially, the locations of stress concentrations indicate areas where cracks begin and will propagate, and provide the starting point for more comprehensive study of the dynamics of crack advancement.

In this paper, we analyze the strain distributions of gap and joint systems, beginning with geometrically simple models and progressing to more complex setups. In particular, we examine sealed and coated two-dimensional tensile and hinged butt joints. Analysis is presented of how the gap opens around a conventional countersunk rivet in a flexed material in three dimensions. The analyses include the addition of a coating layer played over each two-dimensional model, and we examine how the strain distributions are affected by the Young's modulus of the coating and gap sealant. In the models that involve bending, the relationship between coating strain and substrate yielding is explicitly considered since the method of load application often determines in which layer failure occurs first, observed by [10]. Indications are considered for which models might be suitable for use in conventional laboratory accelerated exposure apparatus for future study of candidate materials for coatings and gap sealants.

4.2. Methods

4.2.1. Adhesive joint models

Two different two-dimensional coated joints and a three-dimensional uncoated countersunk rivet joint were modeled using the ANSYS® Academic Research Mechanical (release 17.2) finite-element software package. In each model, all substrate panels use material parameters typical of aircraft-grade aluminum alloys to represent the situation where the substrate is much more rigid than the other materials. Properties of gap sealants and coatings used vary only in modulus. The sealant modulus was chosen to be 10 MPa in all models, with the ratio of top coating modulus to sealant modulus varying as 1:1, 1.5:1, 10:1, 100:1, and 1000:1 in each coated joint. Such a sealant is common in consumer and industrial caulks and sealants that have rubbery properties. Thus this range of coating types spans from one with flexibility like the rubbery gap sealant to one with a modulus of 10 GPa, which is probably somewhat more rigid than a typical topcoat, even below its glass transition temperature. A listing of parameters is shown in Table 4.1.

Table 4.1. Material parameters

	Substrate	Sealant	Top coating
Modulus	71.7 GPa	10 MPa	variable
Poisson ratio	0.33	0.45	0.45
Density (g/cm^3)	2.81	1.20	1.20

In each coated joint model, perfect adhesion is assumed between the material types to allow for close examination of strain concentration points without assuming any particular type or magnitude of adhesive or cohesive failure in the system. However, locations found to have high values of strain are where such failure may be expected. Gap and coating dimensions are chosen larger than might be used in practice initially; they are used in order to clearly observe how strain varies across a gap in each system. However, we also discuss the effects of coating thickness.

The first two-dimensional model, a coated tensile butt joint, has geometric simplicity but general applicability to a range of more complicated joints typically seen on automobiles, airframes, and the like. It consists of two substrate adherends separated by a small gap that is filled with a rubbery sealant and painted over the top. The model has symmetry axes vertically through the center of the gap and along the bottom for ease of computation. The two ends of the substrate panels are pulled apart in-plane a distance up to 15% of the original gap width. The substrate panels and the coating are long compared to the gap, so that all variations in strains on either side of the gap can be calculated. A diagram of the coated tensile butt joint is shown in Figure 4.1. Although these geometries may be used in any orientation in practice, for convenience, terms like "up" and "down" will refer to how the models appear in these diagrams.

The second two-dimensional model examines the same initial geometry but in simple flexure rather than tension, as though there were a hinge at the midpoint. It is visualized here, symmetrically, as though the joint is curved upward, applying non-constant strain across the gap. Thus the gap sealant is in tension at the top and may either be in compression or tension at the bottom, depending on where the hinge is considered. In this model, there

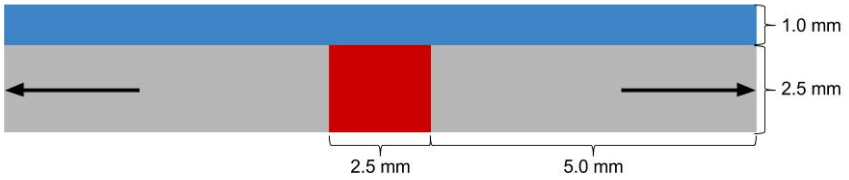

Figure 4.1. Coated tensile butt joint, with sealant (red) and top coating (blue); not to scale

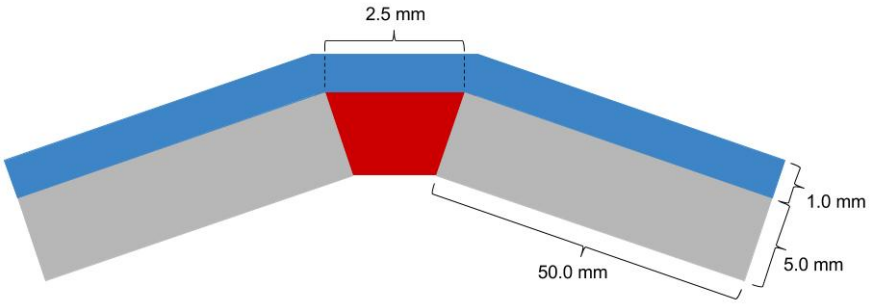

Figure 4.2. Coated two-point bend hinged butt joint after flexing, with sealant (red) and top coating (blue); not to scale

may be no neutral axis. The bend is imposed with the two ends of the substrate panels being moved toward each other a distance 15% of the original gap width, so the result is a tenting upwards. This approach offers a compact geometry and is thus a suitable candidate for testing such coated joints within a standard accelerated weathering cabinet, but the gap opening between the rigid substrates varies from top to bottom and is on average much less, so the overall deformations will be less. Bending motions usually require much less powerful, and hence less bulky, actuators and the length of the substrate panels was chosen suitably compact so that a number would fit within an exposure chamber. This joint is shown in Figure 4.2.

4.2.2. Countersunk rivet model

Many coated gaps arise when a screw or rivet is embedded within a substrate, resulting in a very small gap around the circumference of the fastener. This is extremely common. In such arrangements, coatings tend to fail on and around rivets before elsewhere on the

Figure 4.3. Countersunk rivet (black) in single panel; not to scale

substrate, noted by [100] and [101]. This can be seen on aircraft and other riveted structures; similar failure can unfortunately often be observed around the bolts used in large bridges and other structures. To exemplify these possibilities, a three-dimensional model is used consisting of a single panel with a countersunk rivet embedded within it. This is more complex than the simple geometries modeled here but is probably the most common example, by far, of a coated gap that is stretched or flexed. Since only the strains across the small gap between the rivet head and countersink are of interest for this work, we assume the walls of the rivet shaft freely touch the walls of the hole, and that the bottom of the rivet shaft is flush with the underside of the panel. This permits any tensile panel flexing to separate the shaft and hole, with the consequence of a gap opening at the top. In this model, no coatings are included (for simplicity), but the opening of the gap is mapped as the overall piece is flexed in one direction. This will demonstrate where the problems are severe for a coating that has been used to paint over such a rivet. The panel ends are bent toward each other a distance of 1 mm, giving a bending radius of 0.38 m that is more severe than most applications but perhaps suitable for accelerated testing. Diagrams of this model are shown in Figures 4.3 and 4.4.

4.3. Results

Throughout this paper, strain distributions and values are provided. In each model, fixed displacements mean that input strain is assumed to be precisely controlled. We use two strain types, uniaxial strain and von Mises uniaxial equivalent strain. Uniaxial strain is chosen when examining the sealants and coatings because their properties are usually established in terms of elongation to break, and adhesion strength is often measured as a uniaxial stress to failure. As commonly defined by [102], typical aluminum substrates reach the limit of proportionality (i.e. they yield and possibly fail) at or even below 0.5% strain;

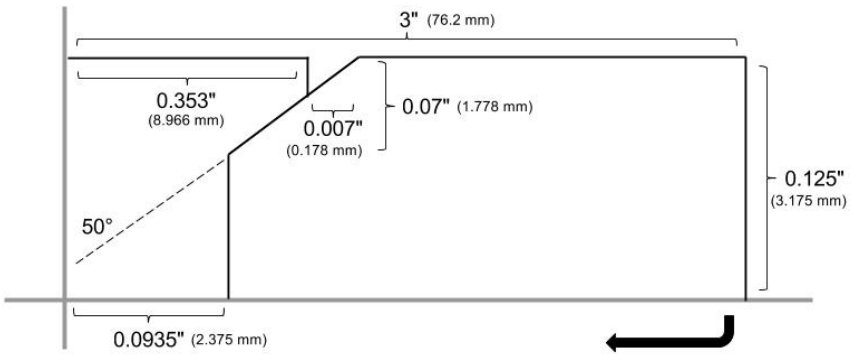

Figure 4.4. Rivet model dimensions, with vertical axis of rectangular symmetry shown; not to scale

depending on the geometry, von Mises equivalent uniaxial strain, first rigorous formulated by [103] is commonly used to determine when this point is reached. The von Mises strain ϵ_v is defined as in [104] in terms of Cartesian normal strain components ϵ and shear strains γ:

$$\epsilon_v \equiv \sqrt{\frac{1}{2}\left[(\epsilon_x - \epsilon_y)^2 + (\epsilon_y - \epsilon_z)^2 + (\epsilon_z - \epsilon_x)^2 + \frac{3}{2}(\gamma_{xy}^2 + \gamma_{yz}^2 + \gamma_{zx}^2)\right]} \tag{4.1}$$

4.3.1. Tensile butt joint

The uniaxial strain in the horizontal direction (i.e. along the tensile or bending direction) was examined in both the two-panel tensile and hinged butt joints. This strain distribution is indicated in Figure 4.5 for the tensile joint on one side of the axis of symmetry that is in the middle of the gap filler.

In the case of the tensile model, only the top half of the joint is displayed since the strain distribution in the gap sealant in consistent below that point. There is a concentration of the strain, and stress, at the stop corner of the metal panel that extends into the coating as well as the sealant. This is the locus of potential failure in either adhesion of the materials to the metal, or in elongation of the coating or sealant. In either case, failure of one type would weaken the coating or sealant towards the other type. The coating is drawn downward into the gap because the sealant must contract in that direction as dictated by its Poisson ratio value. This contributes to the strain in the coating at the corner of the metal substrate.

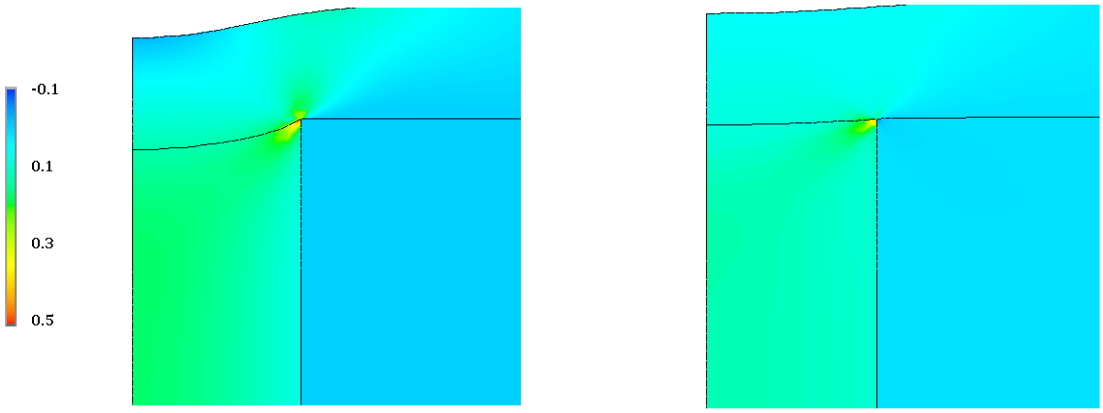

Figure 4.5. Examples of uniaxial horizontal strain distribution for tensile butt joint, with 1:1 (left) and 1000:1 (right) modulus ratio of top coating to gap sealant

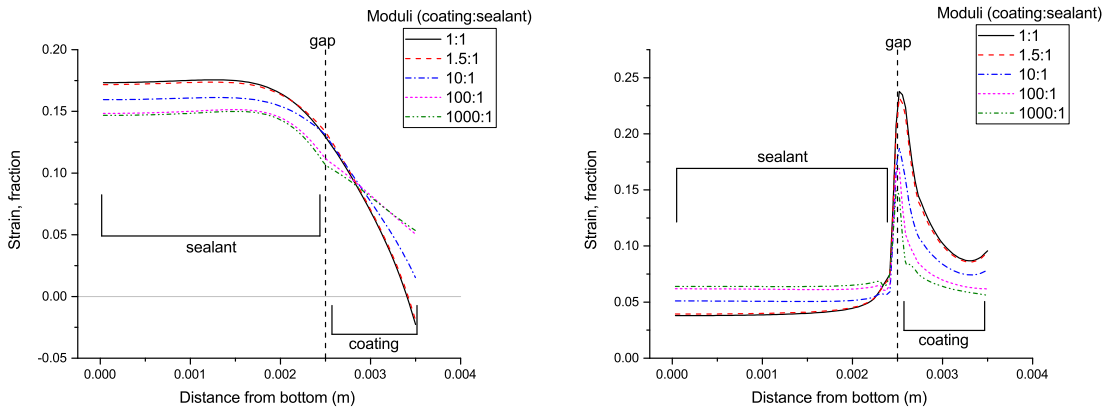

Figure 4.6. Horizontal uniaxial strain in tensile butt joint at the center vertical axis (left) and at the gap sealant wall position (right), from the bottom of the joint through the coating; modulus ratios are given as top coating to sealant

The strain in the middle of the joint is quantified in the left of Figure 4.6 for the various ratios of coating modulus to that of the gap sealant. This is the uniaxial strain in the horizontal direction (i.e. parallel to the substrate panel displacement) within the sealant and top coating from the bottom of the system upward.

Throughout most of the depth of the sealant, the strain is approximately constant, except close to the interface with the topcoat. The externally applied displacement would correspond to a strain of 15%, but the more flexible topcoat permits the strain in the gap to be almost 18%. One can see in Figure 4.5 and the right of Figure 4.6 that the strain near the walls is lower than in the middle of the gap since adhesion to the rigid walls constrains the

strain there. Hence the strain in the middle of the gap is a little higher in order to comply with the overall 15% opening imposed on the gap. For more typical coatings (like those with a modulus several orders of magnitude greater than the sealant), the effect is less and so the strain in the middle of the sealant is much closer to the expected 15%. The strain in the top coating in the center of the gap, beyond the interface, diminishes but stays large. If the coating is very flexible, it can deform and the strain even becomes compressive at the exterior surface as the coating is drawn down towards the gap sealant.

The right of Figure 4.6 quantifies the strain in the tensile direction at the interface of (and above) the metal and gap sealant. The concentration at the corner causes not only the strain to be large enough to cause possible mechanical failure of the coating and sealant, but the stresses at the metal wall corner may be large enough to risk adhesive failure. Good adhesion between a coating and metal substrate is often found in pull-off measurements to be 20 MPa. This corner is where the tensile butt joint will fail and corrosion and other problems will start. In stiffer coatings, the strains at this corner will be lower because the modulus is higher, but unfortunately stiffer coatings will be more brittle and hence likely to fail.

4.3.2. Effect of coating thickness

The models shown above were chosen to have very thick top coatings in order to more clearly observe the distribution of strain. In practice, a coating might be orders of magnitude thinner, depending on the application.

The thickness of the top coating over the tensile butt joint gap was varied over several orders of magnitude from 50 micrometers up to the thickness used above. For this comparison, the panels of the joint were separated a distance of 5% of the gap width, since it proved difficult to construct a mesh that was not excessively distorted when the thinner coatings were stretched over the gap to 15% displacement. Since many aerospace materials may fail at low deformations, as cautioned in [105], a 5% opening of the gap may be considered more realistic in engineered structures. The strain distributions within the joint were qualitatively

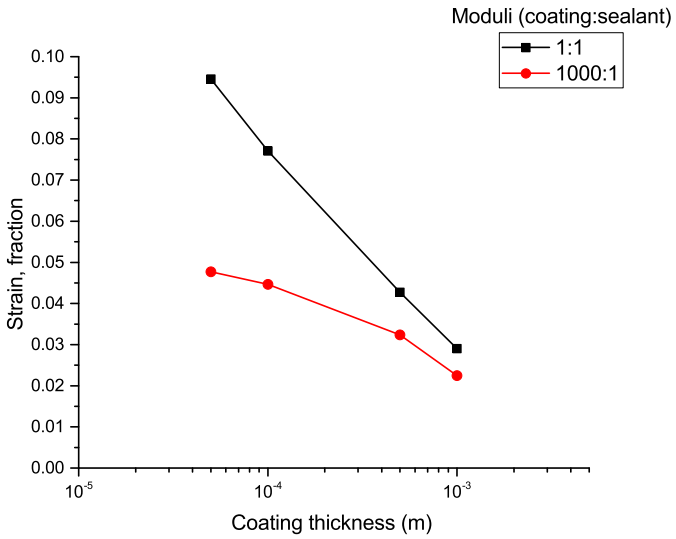

Figure 4.7. Horizontal uniaxial tensile strain in overlying coating of varying thickness at the top of the tensile butt joint over the gap edge, with 5% gap opening

similar to the thicker models and showed a large magnification of the strain at the corner of the substrates. The horizontal uniaxial strain experienced at the top surface of the coating at the edge of the gap, over the corner of the substrate, was computed for both a rubbery coating (with modulus equal to that of the gap sealant) and stiff coating (with modulus ratio 1000:1 to the gap sealant). Figure 4.7 shows these values.

When the coating and sealant have similar moduli, the strain at the top of the coating over the edge of the gap increases strongly in the thinner coatings and becomes much larger than the overall fractional opening of the gap. In fact, the results follow a power law relationship in the thickness variation considered here. The effect of the corner of the substrate cannot diminish so much through the thickness of such thin coatings, as shown in the strain distributions for the 50 um and 100 um models with equal coating and sealant modulus shown in Figure 4.8.

When the coating is much stiffer than the sealant, however, the increase in thinner coatings is not so large; the strain remains below the 5% gap opening value, approaching it as the coating becomes thinner. For each coating thickness, the stiffer coating experienced lower strain, as expected, and is consistent with previous models. Very often, thicker coatings are

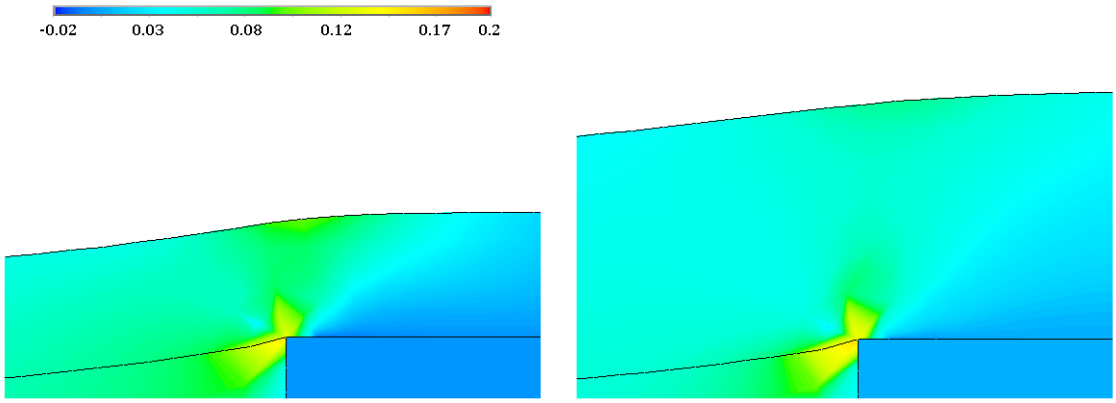

Figure 4.8. Horizontal uniaxial strain distribution zooms for tensile butt joint at 5% gap opening, with 50 um (left) and 100 um (right) coating thickness

used to provide a greater barrier to the transport of moisture and salt to the substrate. These results show that thicker coatings may provide a better barrier because they experience less strain over a gap that opens, and thus may be less prone to crack.

4.3.3. Flexed butt joint

In the flexed hinge joint, the two metal panels move toward each other at the bottom of the gap, while the top corners move away. Figure 4.9 shows that at the bottom of the gap, the strain along the direction of bending is compressive. The consequence is that from the Poisson ratio effect, the gap sealant bulges out at the bottom. Although for simplicity there is no coating over the bottom of the gap, it is easy to appreciate that the bulging would tend to push such a coating away from the substrate and possibly cause adhesive failure.

Figure 4.10 shows the strain in the flexing direction at the vertical axis of symmetry moving upward, both within the gap and at the substrate wall.

The neutral axis, where the sealant is neither in tension nor compression, depends heavily on the relative modulus between the coating and sealant. If the coating is as flexible as the sealant, the neutral axis is slightly above the midpoint of the gap depth, as expected. If the coating is much stiffer, it does not undergo much strain and the neutral axis moves up into the coating, leaving most of the sealant in compression. Figure 4.11 shows the displacement

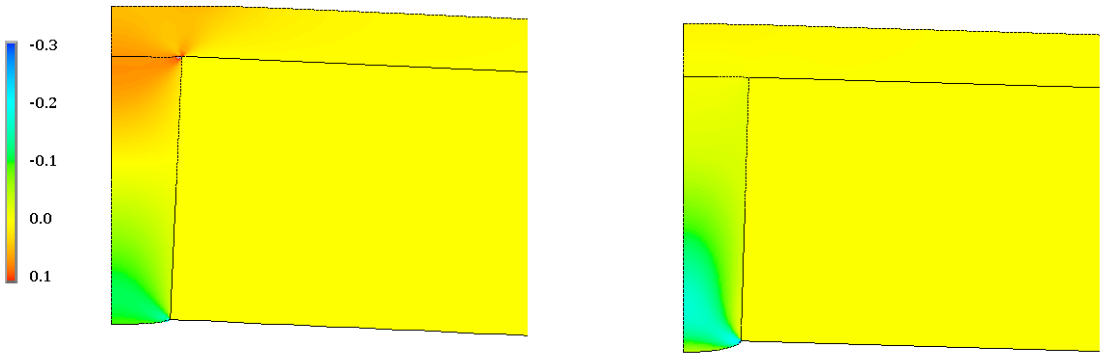

Figure 4.9. Examples of uniaxial horizontal strain distribution for hinged butt joint in flexure, with 1:1 (left) and 1000:1 (right) modulus ratio of top coating to gap sealant

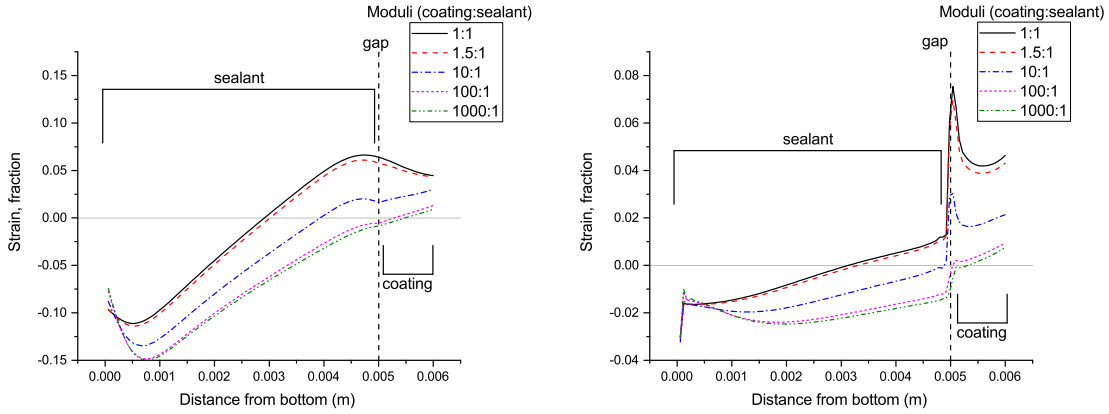

Figure 4.10. Horizontal uniaxial strain in hinged butt joint at the center vertical axis (left) and at the gap sealant wall position (right), from the bottom of the joint through the coating; modulus ratios are given as top coating to sealant

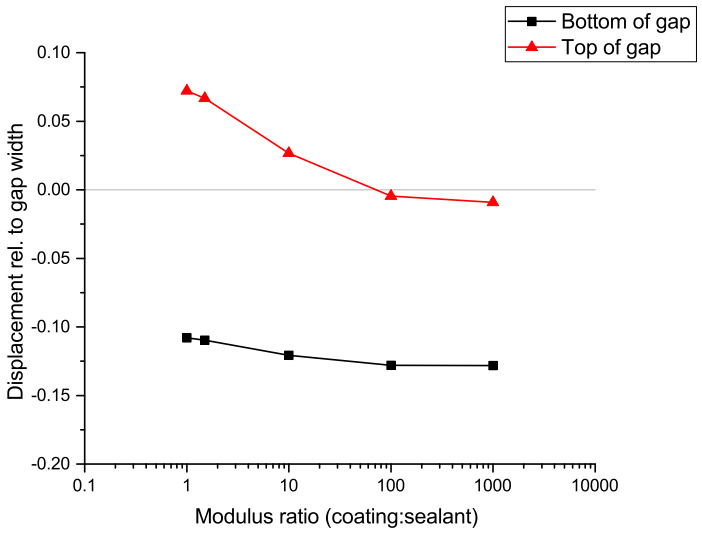

Figure 4.11. Horizontal displacement (relative to gap width) at top and bottom corners of gap in hinged butt joint; modulus ratios are given as top coating to sealant

of the top and bottom corners of the gap in the directional of flexing (horizontally in the models above).

Because the joint is flexed and the gap closes at the bottom while the top opens, the strains in the gap sealant and coating are not so high. Within the gap, the strain is not as high as within the corresponding tensile joint, so a suitable gap sealant may readily survive the deformation. If the coating is equally soft, it may also survive. If the coating is stiff, however, the neutral axis is within it and the strains may well be low enough that the coating does not suffer a cohesive failure over the middle of the gap (as in the left of Figure 4.10); however, there is still a stress concentration at the upper corner of the metal substrate (as in the right of Figure 4.10), so the materials may fail there. In flexure, this joint is less demanding overall of the properties of the gap filler and the coating than if the same joint were in tension.

The flexed joint, depending on the circumstances, produces a noticeable bulging at the bottom. This effect of the Poisson ratio is seen more readily in the expanded view of the uncoated underside of the joint in Figure 4.12.

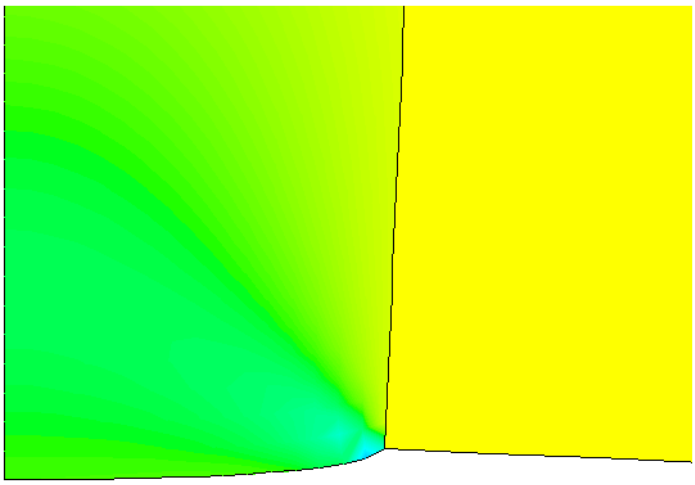

Figure 4.12. Compressive effect of Poisson ratio in underside of hinged butt joint (zoom of Figure 4.9, right)

The right of Figure 4.10 shows a small increase in the strain of the bottom of the gap regardless of the modulus ratio. The absolute value of this strain is unlikely to cause a failure of the gap sealant. However, the bulge might cause any coating there to be peeled away from its contact with the metal at the corner, causing a problem.

If the coating over the gap has a modulus similar to that of the sealant, any adhesion between them is likely to survive since the strain will be fairly continuous across the interface, especially here where the Poisson ratios are the same (chosen for simplicity). However, in both the tensile and the flexed joints, a problem will occur if the moduli are substantially different because in both joints, the sealant tends to shrink into the gap away from the coating as the gap opens. Figures 4.13 and 4.14 show how the strain in the vertical direction varies across the interface between the gap filler and the coating along the middle of the gap and at the gap wall as their relative properties change.

In both the tensile and flexed joints, the coating bends into the joint with the sealant, as indicated by Figure 4.13. In the tensile joint, the filler and coating are both in substantial compression due to the Poisson ratio, so this strain pulls them away from each other. As stated earlier, this modeling does not extend to the complexity of including adhesive strength,

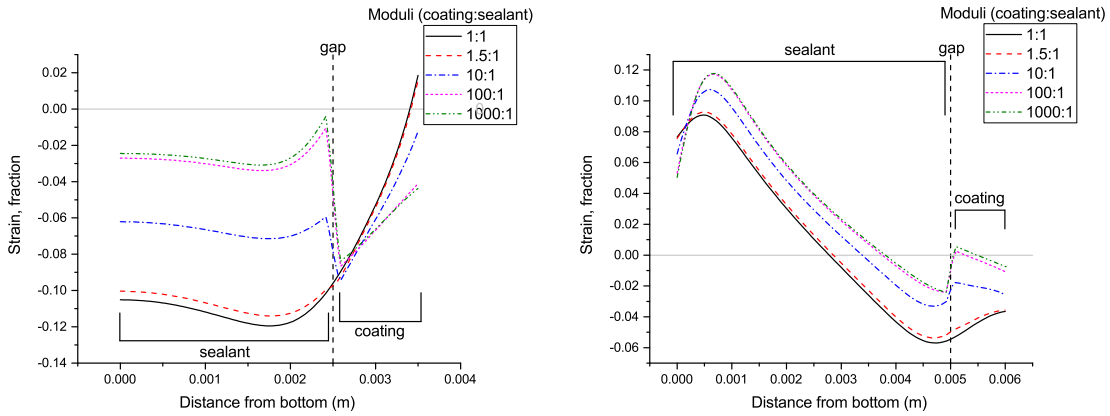

Figure 4.13. Vertical uniaxial strain along center vertical axis for tensile (left) and hinged (right) butt joints

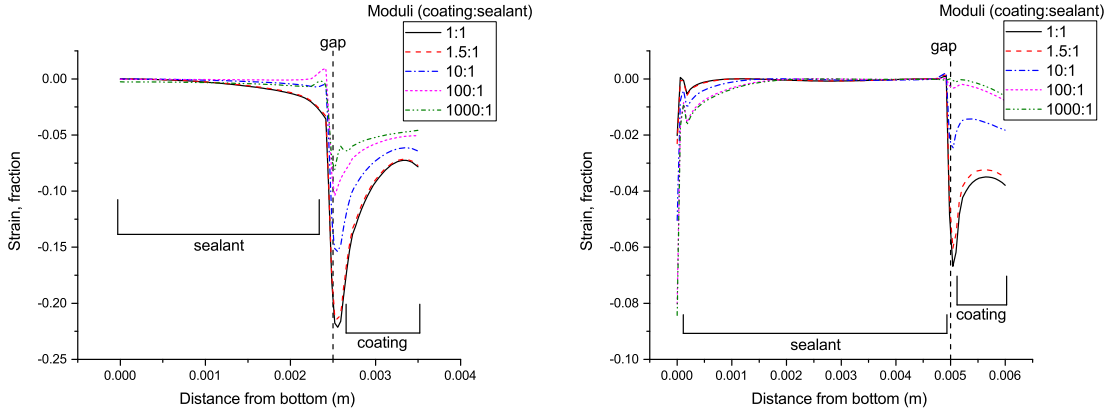

Figure 4.14. Vertical uniaxial strain along substrate wall for tensile (left) and hinged (right) butt joints

but the stress in a stiff coating corresponding to a strain of a few percent could be enough to overcome the adhesion with the gap filler. In flexure, these vertical strains at the boundary are much less, and thus less threatening.

At the wall, the vertical strain is limited in the gap filler by adhesion to the wall, as shown in Figure 4.14. As the boundary is approached, the coating which extends beyond the gap tends to exert a force on the gap filler, increasing the vertical component of the strain. Even close to the wall of the gap, in the tensile joint, both materials experience a force that tends to make them thinner and thus may cause adhesive failure. In flexure, the vertical compression at wall is due not only to the stretching in the flexure direction, but the turning of the metal panels pushes the coating towards the metal and alleviates its potential for disbonding. Nevertheless, at the corner, the component of the strain in the flexing or stretching direction can be more than sufficient to cause failure.

It is interesting that the arrangement has considerable potential for failure between the gap filler and coating, so the protection for the underlying metals is much reduced. A single application of one continuous material, instead of layers, may bring benefits.

Finally, we examine the horizontal uniaxial strain distribution across the top of the overlying coating. Since this coating is very thick and without ends, the strain field has decayed from the corner and transition effects. The strain is plotted from the center of this zone outward to the location of the substrate corner in Figure 4.15.

In the very thick coating modeled here, the material at the top of the coating can move substantially and the strain is a fraction of the gap opening ratio of 15%. For the tensile joint, the very stiff coatings have a moderate strain that is fairly consistent with position, whereas the more flexible coatings permit the middle of the span to have an even further diminished strain that is compensated somewhat at the edge of the gap. The flexed joint, with the displacement as imposed in this situation, does not suffer so much strain anywhere across the top of the coating and it does not vary so much across the gap.

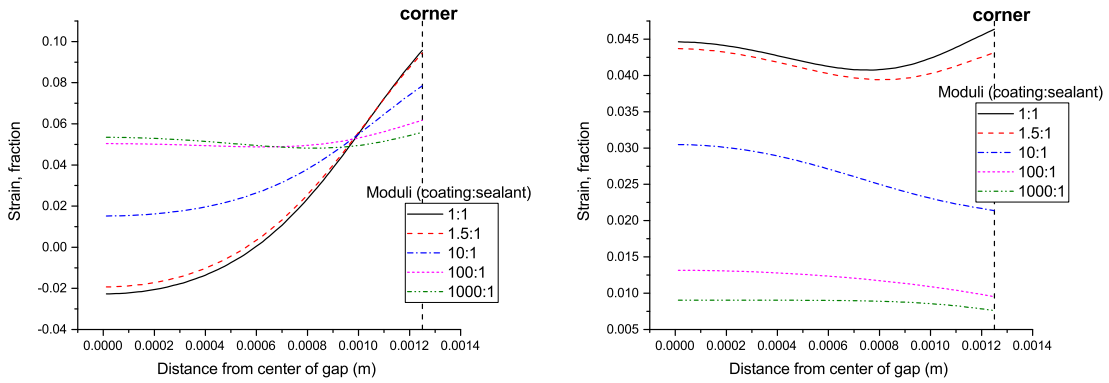

Figure 4.15. Horizontal uniaxial strain along top of overlying coating for tensile (left) and hinged (right) butt joints

4.3.4. Countersunk rivet model

The primary interest in this model is how a gap may open around the rivet when flexed. However, since we are examining a structure that has only metals and it is important to know whether any gaps will close when the flexing is removed, we observe the possibility of plastic deformation in the metals by also calculating the von Mises equivalent uniaxial strain. An elastic limit of 0.5% is typical of many metals. The flexure here amounted to a bending radius of 0.38 m, which is more severe than might be typical of many applications. Figure 4.16 shows the von Mises strain, with axes of symmetry along the left and front faces of the model.

When the panel is flexed, the rivet head experiences negligible strain since it does not adhere to the substrate panel.

In the left of Figure 4.17, we plot the longitudinal uniaxial and von Mises strains along the top long edge of the panel in the direction of bending curvature, from the center of the rivet towards the end of the panel (left to right in the above model diagram), indicating the location of the transition from rivet cap to substrate panel. The uniaxial strain perpendicular to the flexure direction and the von Mises strain are also plotted from the center of the rivet across the long axis of the panel (front to back in the diagram) in the right of Figure 4.17.

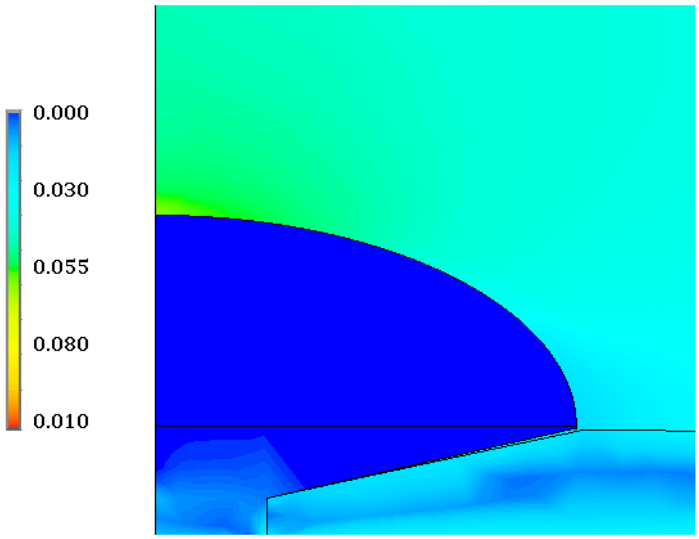

Figure 4.16. Example of von Mises equivalent uniaxial strain distribution for countersunk rivet model, with rivet head at lower left

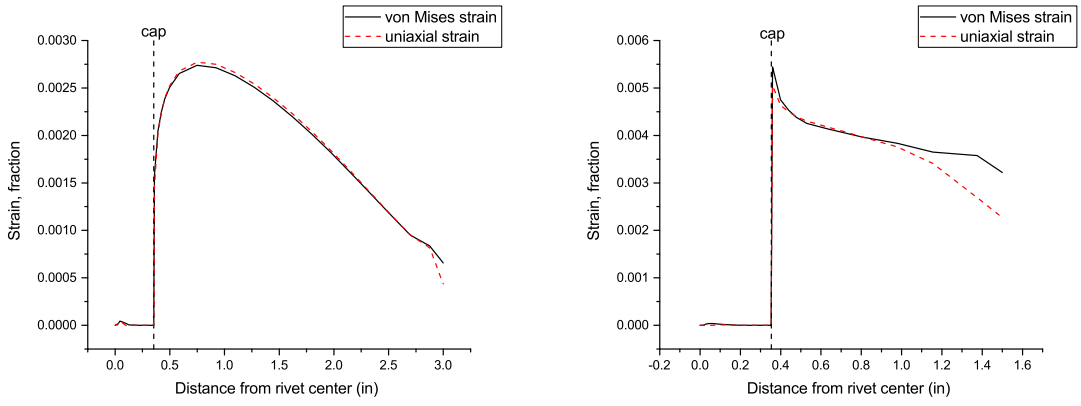

Figure 4.17. Von Mises and longitudinal uniaxial strains from center of rivet outward along the direction of curvature (left) and perpendicular to the direction of curvature (right)

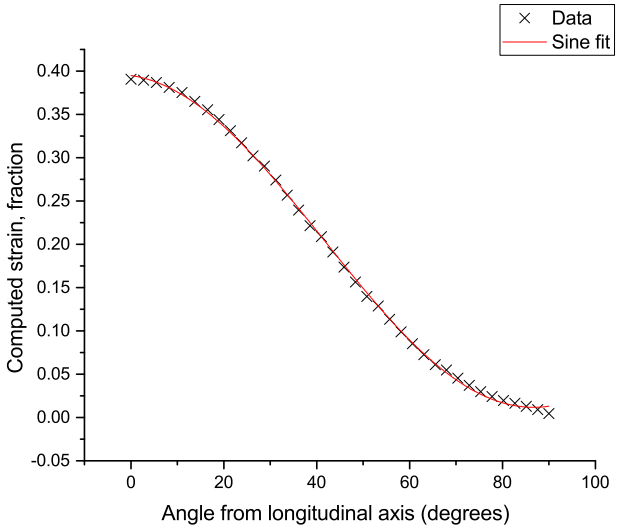

Figure 4.18. Computed strain across rivet gap as a function of circumferential angle, with best sinusoidal fit

The von Mises strains are little different from the uniaxial strains here. The bending imposed here does not produce strains that cause plastic deformation in most metals, so the gap around the rivet would close if the flexure were released in most circumstances.

Of particular interest is the strain experienced across the small gap between the outer circumference of the rivet head and the substrate. Since this gap is initially very small, any opening due to flexing necessarily imparts large strain to any coating placed over it or gap sealant within it. The nature of flexing is such that the strain must vary around the rivet head, being largest at the point along the flexing longitudinal axis and smallest at the point along the lateral axis. There are no coatings or gap fillers used here, as we instead compute the overall strain of the gap dimension using the displacements at the top of the rivet cap from the edge of the metal panel. This is shown in Figure 4.18, along with a sinusoidal curve fit.

As anticipated, the gap strain follows a sinusoidal variation around the circumference due to the simple nature of the flexing here. The peak value along the longitudinal axis is nearly 40% in this case, and so is well above the elongation to break for many types of coatings. However, most of the periphery of the rivet has a gap that opens and thus anywhere

may strain a coating or gap sealant beyond their cohesive or adhesive limits. Although there are other designs of rivets, the analyses of the gap opening in tension and bending above shows the likely routes to failure of the protective gap filler and coating, with the most likely practical consequence being corrosion of the fastener and the substrate. The presence of a rubbery sealant between the rivet head and surrounding substrate is unlikely to have a marked effect on these strain values, since the metals used are far stiffer and still force the gap open. Additionally, layering coatings above the rivet-substrate interface results in a Poisson ratio effect, as seen in the two-dimensional models, which draws the coatings inward. It is clear that when one sees evidence of corrosion or other failure around a rivet, or other type of fastener, the opening of the gap could have been a major contributor to the failure, especially if it happens many times in the service of the structure.

4.4. Conclusions

Gaps are very common in structural elements for a wide variety of reasons, and many may be filled with a sealant, grout, or caulk and then painted over. Simple coated butt joints have been examined to understand how deformation around gaps may cause failure in the protection afforded by the gap sealant and coating. The behavior of a gap around a typical rivet was calculated in order to provide context for the results from the simpler geometries. This work was done not only to better understand material failure around such joints, but also to explore how a test piece could be designed for use in accelerated laboratory testing.

Two-dimensional strain distributions for the opening, in either tension or flexure, of a filled and coated gap were calculated. The modulus of the gap sealant was chosen to represent a rubbery material and the coating above had a modulus varying from the same as the sealant to 1000 times greater.

The calculations show that not only does the opening of a narrow gap threaten the elongation to break of a coating across that gap, but also that the adhesion of the gap sealant to the walls of the gap at the corner of the substrate, and between the coating and gap filler, may fail. In tension, there is a natural tendency of the sealant and the coating

to shrink laterally, so the effect of having a layered structure is that the layers may pull apart perpendicular to the overall deformation. Although to a macroscopic view the failure is obviously around the fastener, in detail there are multiple loci of failure.

One method of imposing flexure was examined and found that bending the joint imposes fewer demands than linear tension on the gap sealant and the coating. Due to the more complex flexing of the hinged butt joint, since there is no continuous substrate, there is no simple neutral axis of the system. As a result, regions of tension and compression with the gap vary. However, this approach may prove to be the basis of a device to use in accelerated weathering so that mechanical stresses are imparted as well as the more standard environmental stresses.

A simple three-dimensional model of a countersunk rivet was examined to map how the gap around it opens in simple flexure. Rivets are an extremely common type of fastener and exemplify gaps that are commonly filled and painted over. Flexing of the substrate can produce very large strains across the gap where the strain changes sinusoidally around the circumference. The overlying coating may well fail first where the gap opens most, but the failure is likely to propagate all the way around the fastener. The two-dimensional analyses of simple coated butt joints may provide insight in how to better design fasteners or chose materials to fill the gap or paint over it.

While it has been long appreciated that a gap that opens is likely to cause the coating over the gap to fail, probably less appreciated are the additional problems that a layer of coating over a different material in the gap brings. Depending on the strain and any difference in Poisson ratio, in tension the sealant may pull away from an overlying coating. In compression, the sealant may push an overlying coating away from the metal on either side of the joint. Thus, a layered structure has several possible ways to fail, introduced solely due to there being different materials in the sealant compared to the overlying coating.

5. ANALYSIS OF A DIFFUSIVE LATTICE BOLTZMANN METHOD FOR BARRIER COATINGS

5.1. Introduction

In test, coatings are often prepared on a metal or composite substrate and exposed to moisture, either in a test chamber or complete saturation. Experimentally, techniques like electrochemical impedance spectroscopy and simple mass measurements can be used to understand the rate of diffusion of moisture over time, as well as the total uptake into the coating [107, 108]. In the case of single coating layers, Fickian diffusion is well-suited to model behavior over a range of material types.

The situation is more complex for systems consisting of multiple layers, since applications in industry most often require applications of different coating types in succession: for example, a highly-adhesive epoxy primer with a urethane protective topcoat. Each of these layers may have different diffusion properties that can vary by orders of magnitude. Because of the necessity of understanding the behavior of such systems, it is useful to model the effects of moisture exposure and cycling over long times in order to predict the time scales and uptake behavior used in test protocols and field exposure. A variety of techniques are available for such analysis, ranging from analytical solutions to finite-element approaches [32, 34, 109]. Such approaches, particularly finite-element analysis, are often computationally intensive, may not incorporate all desired phenomena, and are often closed-source software packages using methods and algorithms that are not open to verification and analysis.

The work in this chapter was conducted by the author and collaborators K.T. Strand and A.J. Wagner in a published paper [106]. Mathematical derivations were completed by the author and Strand. Simulations were designed and analyzed primarily by the author, with assistance in the convergence analysis from Strand. Fourier analysis was completed mainly by Strand and Wagner.

Any numerical technique used to model the progression of moisture in such a stackup must stably account for a wide range of diffusion constants. Since laboratory testing of candidate barrier coating systems typically includes cyclic exposure to moisture and dry ambient air over long periods of time, simulations of cyclic processes must maintain numerical stability over correspondingly longer time scales.

In order to flexibly incorporate a range of uptake phenomena (like concentration-dependent diffusion) efficiently, we first derive and analyze the error introduced in the traditional second-order approximation to the diffusion equation used in lattice Boltzmann approaches. To investigate the nature of this error, we introduce a fourth-order correction and perform a Fourier component analysis to confirm the correctness of our results. We show that the bulk of the second-order error in such a system arises from the boundary conditions used, and comment on the proper use of periodic systems to remove this error. Applications to multi-layer systems with variable diffusivity are discussed in the context of our analysis, and investigated in further detail in a later chapter.

5.2. Lattice Boltzmann methods

The dynamics of fluid density ρ obey the continuity equation

$$\partial_t \rho + \nabla \mathbf{j} = 0, \tag{5.1}$$

where $\mathbf{j}$ is the mass current. Assuming an isotropic coating, mass current will be in the direction of negative density gradient. We denote the proportionality between this current and negative gradient by D, which in the simplest case is a constant. Later, we consider a more general $D(\rho)$. We therefore have $\mathbf{j} = -D\nabla\rho$. With this constitutive relation for the mass current, we recover the well-known diffusion equation.

The lattice Boltzmann numerical method tracks the evolution of a generalized particle distribution on a lattice. The generalized lattice densities change over time under the influence of localized collisions that redistribute the particles to neighboring lattice sites. The

approach is quite general, and has been used extensively to model hydrodynamic behavior [110, 111, 112], diffusion [113, 114], electrostatics [115], and similar systems with high accuracy and computational efficiency. Unlike the use of a partial differential equation solver, the equations underlying the dynamics of a particular system are not the starting point for the method, but rather a natural emergence from it. The particular form of the collision terms, which relax the system toward a local equilibrium at each lattice point, and the moments of the local equilibrium distribution determine the governing equations for the chosen system, as we show below.

We wish to use a lattice Boltzmann approach to model diffusion through a one-dimensional medium, the boundary conditions of which will be defined later. In this case, the generalized particle distribution has three components at each lattice site: flow in the negative-x direction $f_{-1}(x,t)$, a stationary component $f_0(x,t)$, and flow in the positive-x direction $f_1(x,t)$. A velocity constant accompanies each component. This is the minimal velocity set to recover the desired diffusion equation, as described below.

A commonly-selected collision term defines a local equilibrium that only depends on conserved quantities and relaxes the actual density towards the local equilibrium; it is spatially and temporally independent. In this form, the lattice Boltzmann equation can be written as

$$f_i(x+v_i,t+1) = f_i(x,t) + \sum_j \Lambda_{ij}\left[f_j^0(\rho(x,t)) - f_j(x,t)\right]. \tag{5.2}$$

Here f_j^0 is the local equilibrium density, Λ_{ij} is a collision matrix, and $\rho(x,t)$ is the local density of the system, defined by

$$\rho(x,t) = \sum_i f_i(x,t). \tag{5.3}$$

For diffusive systems like the one considered here, the advantages of a more complex matrix form are less well established (See Ginzburg [116]), so we will employ a collision matrix of

the form

$$\Lambda_{ij} = \frac{1}{\tau}\delta_{ij} \tag{5.4}$$

that was originally proposed by Qian [110]. It establishes a relaxation time constant τ.

Using this form, the lattice Equation 5.2 becomes

$$f_i(x + v_i, t + 1) = f_i(x, t) + \frac{1}{\tau}\left[f_i^0(\rho(x, t)) - f_i(x, t)\right]. \tag{5.5}$$

We now show how this equation, coupled with distribution moments that will be defined shortly, leads to the diffusion equation. First perform a Taylor expansion of the left side of Equation 5.5 to second order:

$$f_i(x + v_i, t + 1) = f_i(x, t) + (\partial_t + v_i\partial_x)\, f_i(x, t) + \frac{1}{2}(\partial_t + v_i\partial_x)^2\, f_i(x, t) + O(\partial^3) \tag{5.6}$$

Comparison of the first-order portion of this expansion with Equation 5.5 gives a recursive expression for each distribution component:

$$f_i(x, t) = f_i^0(\rho(x, t)) - \tau(\partial_t + v_i\partial_x)f_i(x, t) + O(\partial^2) \tag{5.7}$$

Another substitution, after discarding terms of quadratic order, gives the distribution components only in terms of the local equilibrium distribution:

$$f_i(x, t) = f_i^0(\rho(x, t)) - \tau(\partial_t + v_i\partial_x)f_i^0(\rho(x, t)) + O(\partial^2) \tag{5.8}$$

In order to recover the diffusion equation, it is necessary to impose moments on the equilibrium distribution:

$$\sum_i f_i^0 = \rho \tag{5.9}$$

$$\sum_i f_i^0 v_i = 0 \tag{5.10}$$

$$\sum_i f_i^0 v_i^2 = \rho\theta \tag{5.11}$$

Here θ is a parameter. The first two moments ensure local density conservation and no net velocity at equilibrium, and the third imposes a term analogous to an ideal gas pressure. (A more general approach toward advection-diffusion could be followed by allowing nonzero velocity.) Following [117], we use these moments with our previous analysis. We combine the expansion in Equation 5.6 with the lattice Equation 5.2, dropping the explicit dependence on x and t for brevity:

$$f_i + (\partial_t + v_i\partial_x)f_i + \frac{1}{2}(\partial_t + v_i\partial_x)^2 f_i + O(\partial^3) = f_i + \frac{1}{\tau}(f_i^0 - f_i) \tag{5.12}$$

We can then substitute the distributions f_i on the left side of this equation using Equation 5.8:

$$(\partial_t + v_i\partial_x)\left[f_i^0 - \tau(\partial_t + v_i\partial_x)f_i^0\right] + \frac{1}{2}(\partial_t + v_i\partial_x)^2\left[f_i^0 - \tau(\partial_t + v_i\partial_x)f_i^0\right] = \frac{1}{\tau}(f_i^0 - f_i) \tag{5.13}$$

We then drop all terms higher than second order (including second-order time derivatives, which are fourth-order in x) and sum over all velocities i, using the moments introduced above, to obtain

$$\partial_t\rho = \partial_x\left(\tau - \frac{1}{2}\right)\partial_x(\rho\theta) \tag{5.14}$$

that establishes the lattice diffusion equation. In the case where both parameters τ and θ are constant in space and time, this gives a diffusion constant $D = \theta(\tau - 1/2)$.

Notice that this derivation has not yet specified the form of the equilibrium distribution, but rather its constraints via moments. There is a rather simple form for this distribution that uses the parameter θ as a weight applied to the local density ρ:

$$f_{-1}^0 = \rho\frac{\theta}{2} \tag{5.15}$$

$$f_0^0 = \rho(1-\theta) \tag{5.16}$$

$$f_1^0 = \rho\frac{\theta}{2} \tag{5.17}$$

Notice that this distribution trivially satisfies the given moments. It allows for a full and self-contained simulation method for a one-dimensional diffusive system. It is worth noting that the choice of distribution moments and equilibrium distribution leads to the governing diffusion equation, despite the generality of the lattice Boltzmann equation itself.

Despite the derivation needed to obtain Equation 5.14, the integration of this technique in code is extremely straightforward. At each timestep in a simulation, there are two steps: *collision* and *streaming*. In the collision step, the local density is computed at each lattice site as the sum $\sum f_i$. Then, the Bhatnagar-Gross-Krook collision operator (from above) is applied using the known local equilibrium distribution.

In the streaming step, generalized densities f_i are redistributed. Each f_{-1} component is distributed in the negative-x direction, and each f_1 component is distributed in the positive-x direction. Any f_0 component is left unchanged. We discuss boundary conditions in the subsequent section.

5.3. Application to water content of coatings

We wish to model the wetting of a single-layer coating via Fickian diffusion. Since coatings are frequently examined in the laboratory on test panels using weathering chambers that subject the coating to moisture, we will consider the case where the coating, represented by a lattice from $0 \leq x \leq L_x$, is exposed to a reservoir of varying concentration $\rho^b(t)$ at $x = 0$ and an impermeable substrate at the right end of the simulation lattice. The meaning

of ρ^b is the amount of water that will be absorbed just inside the coating as it is exposed to the environment. For an immersion in water, this corresponds to the maximal water content the coating can absorb, and we scale the density so that this value corresponds to $\rho = 1$.

We must account for these two boundary conditions in our numerical simulation. We implement the source term by setting

$$f_i(0,t) = f_i^0(\rho^b(t)) \tag{5.18}$$

(replacing Equation (5.2) at the boundary) and by replacing the streaming step at the right end by a bounceback algorithm, where the right-moving $f_1(L_x)$ is reinserted as an f_2 in the streaming step. The result for a step function $\rho^b(t) = \Theta(t)$ in the exposure is shown in Figure 5.1. We used a system with $L_x = 100$ lattice points, $\tau = 1$, $\theta = 0.5$, $\rho_0 = 1$, and ran the simulation for a variable number of iterations T. As expected, moisture is at first located closely to the surface and then penetrates the sample.

To verify the correctness of the simulation results, we construct an analytical solution for the concentration over time, using linear combinations of the well-known error function solution [31]. These are solutions of the diffusion equation for the initial condition of a step function in an infinite system. If the initial step goes from $2\rho_0$ to zero, then the solution is

$$\rho^{th,1}(x,t) = \rho_0 \left(1 - \mathrm{erf}\left(\frac{x}{\sqrt{4Dt}}\right)\right). \tag{5.19}$$

This solution has a fixed point $\rho^{th,1}(0,t) = \rho_0$ at $x = 0$, which corresponds to our boundary condition. So $\rho^{th,1}(x,t)$ for $x \geq 0$ and $t > 0$ is the analytical solution for an infinite dry coating exposed to a reservoir starting at time $t = 0$. Note that the long-time behavior gives $\rho^{th,1}(x, t \to \infty) = \rho_0$ as expected.

Suppose now that we have a finite one-dimensional coating extending from $0 \leq x \leq L_x$. At $x = 0$, the coating is exposed to a reservoir with fixed concentration $\rho(x = 0, t) = \rho_0$. At $x = L_x$ is an impermeable substrate where $\nabla\rho(x = L_x, t) = 0$.

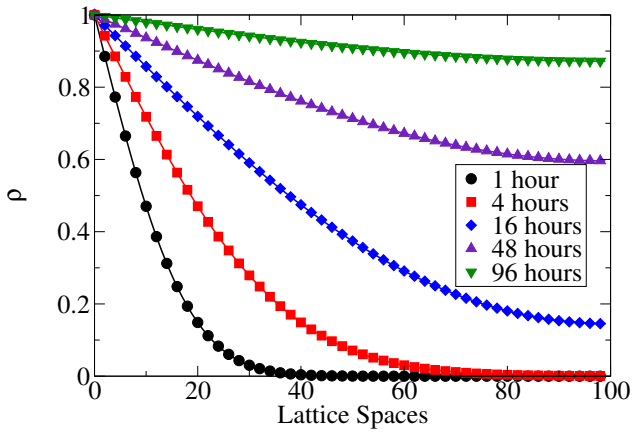

Figure 5.1. Concentration profile at $\tau = 1$, $\theta = 0.5$, $\rho_0 = 1$ at various times (symbol), with analytical solution $\rho(x,t)$ (solid line), where the diffusion constant is $D = 10^{-14}$ m^2/s.

To account for the vanishing current at the substrate, we use an image source reservoir at $x = 2L_x$. This will ensure a vanishing gradient at $x = L_x$ and, by symmetry, a vanishing current. However, when the reflected concentration becomes nonzero at the reservoir again, we must subtract another image source reservoir at $x = -2L_x$ to maintain the correct boundary condition. Repeating this process infinitely, we arrive at the final solution that includes both reservoir and substrate:

$$\rho^{th}(x,t) = \rho_0 \sum_{i=0}^{\infty} (-1)^i \left[2 + \text{erf}\left(\frac{x - 2(i+1)L_x}{\sqrt{4Dt}} \right) - \text{erf}\left(\frac{x + 2iL_x}{\sqrt{4Dt}} \right) \right] \tag{5.20}$$

For practical purposes, we find ten terms of the infinite sum in Equation (5.20) are entirely sufficient for most cases.

It is instructive to determine the correspondence between these numerical parameters and a laboratory case. A typical barrier coating might have thickness $X = 50$ μm, diffusion constant in water $D \sim 10^{-14}$ m^2/s, and be exposed to moisture in a weathering chamber for $T = 4$ hours at a time for testing. We can introduce reduced time, length, and density scales

t', x', ρ' such that

$$t = Tt' \tag{5.21}$$

$$x = Xx' \tag{5.22}$$

$$\rho = \rho_0 \rho' \tag{5.23}$$

and $0 \leq \{t', x', \rho'\} \leq 1$. Since the unit relationship $T = X^2/D$ holds by dimensional analysis, for any given experimental setup the quantity

$$F \equiv \frac{TD}{X^2} \tag{5.24}$$

is dimensionless and we have the scaled diffusion equation $\partial_{t'}\rho' = -\nabla_{x'} F \nabla \rho'$. Using the experimental parameters suggested above gives $F = 5.76 \times 10^{-2}$. In our simulations, we use total length $X = L_x = 100$ lattice sites, reservoir concentration $\rho_0 = 1$, $\theta = 0.5$, and $\tau = 1$. Since this gives a time scale $T \approx 2300$ iterations, this means one hour of equivalent macroscopic exposure corresponds to approximately 575 simulation iterations. Further, the choice of $\tau = 1$ yields immediate relaxation of local distributions, so we would expect excellent agreement to theory.

We are now in a position to comment on the accuracy of this simulation method in comparison to the analytical solution ρ^{th} in Equation (5.20). For each of the exposure times in Figure 5.1, we compute the absolute error

$$\epsilon(x) \equiv \left| \rho(x,t) - \rho^{th}(x,t) \right| \tag{5.25}$$

across the lattice space profile. The result is plotted logarithmically in Figure 5.2, showing excellent agreement. It is interesting to observe how the error changes over time; initially, the error drops substantially since moisture has not yet permeated through the entire coating lattice. This tail increases as the entire lattice becomes wet, but then uniformly decays as

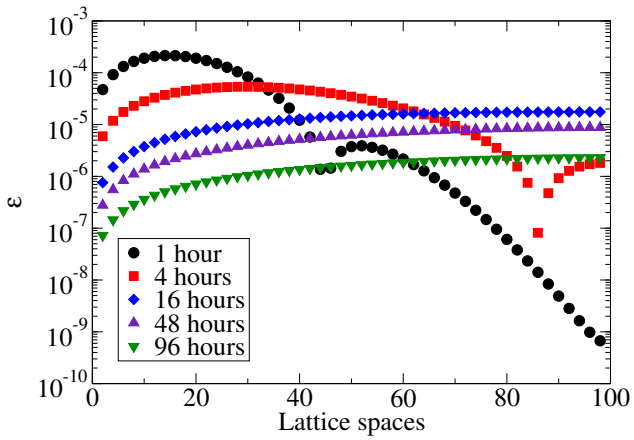

Figure 5.2. Absolute error profile ϵ between numerical and analytical concentration for exposure over time.

the numerical solution approaches saturation and agrees with the corresponding analytical solution.

While this method provides efficient and stable numerical modeling of a single coating, a given coating system might consist of two or more barrier layers in a stackup, each with a different diffusion constant that permits moisture ingress and egress at different rates from its neighbors. To extend this method to the simplest multi-layer case, we might wish to model a two-layer stackup consisting of idealized barrier coatings with different physical properties. To do so, our reservoir model is modified slightly, with the outer barrier coating represented at lattice sites $0 \leq x \leq L_x/2$ and the inner barrier coating at $L_x/2 \leq x \leq L_x$. Since the diffusion constant is controlled by the parameter τ, the presence of two diffusion constants requires that τ be position-dependent:

$$\tau = \tau(x) \equiv \begin{cases} \tau_{\text{out}} & , \quad 0 \leq x \leq L_x/2 \\ \tau_{\text{in}} & , \quad L_x/2 \leq x \leq L_x \end{cases} \tag{5.26}$$

Incidentally, changing the value of θ between the two regions will lead to different maximum water uptake in the layers, an important relationship that will be explored later.

Although such a two-layer system is not investigated here, it is essential to determine the range of τ values for which numerical and analytical solutions agree sufficiently over

Table 5.1. Values of τ and θ used in simulations, with corresponding diffusion constant D and time scale T corresponding to four hours of macroscopic equivalent exposure with $F = 5.76 \times 10^{-2}$ (all in lattice units).

τ	θ	D	T
0.55	0.5	0.025	23040
0.70	0.5	0.10	5760
1.0	0.5	0.25	2304
1.5	0.5	0.50	1152
2.0	0.5	0.75	768
10.0	0.5	4.75	121

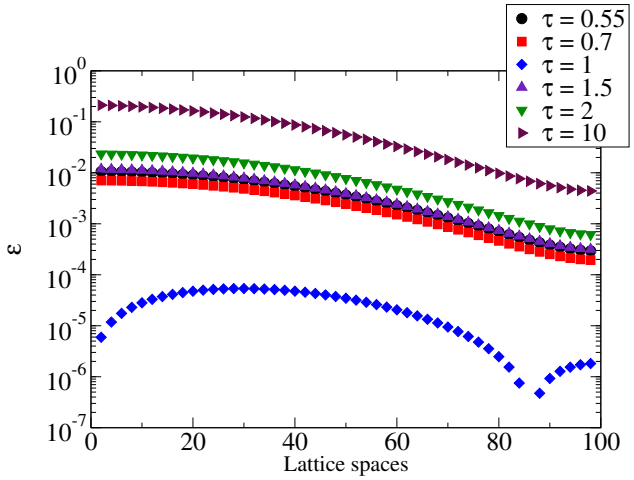

Figure 5.3. Absolute error profile ϵ between numerical and analytical concentration at various τ. All simulations were run to the same scaled time, corresponding to four hours of macroscopic equivalent time.

time. For efficient simulations, it is advantageous to choose τ as large as feasible, since this corresponds to a large diffusion constant and hence a shorter simulation time. For a quick initial evaluation, we run a series of lattice Boltzmann simulations with varying values of τ to the same macroscopic equivalent time of four hours of exposure. After that time, we compute the absolute error ϵ between numerical and analytical solutions across the entire lattice profile. Results are shown in Figure 5.3. The choices of τ, along with the corresponding time scale T, are shown in Table 5.1.

As shown earlier, the solutions agree very well for $\tau = 1$. However, the error may be orders of magnitude larger for $\tau \neq 1$. Depending on the particular application, we may

require ratios of diffusion constants that vary significantly (such as in multi-layer systems); however, the errors indicated here may cause the numerical method to appear less than ideal. We discuss the lower asymptotic limit $\tau \to 0.5$ later.

We therefore wish to examine the origin and nature of the τ-dependent error. Of note is that the derivation of the lattice diffusion equation given above (and used heavily in the literature) is done with only a second-order Taylor approximation. To determine the degree to which this approximation leads to the errors shown, we next perform a fourth-order correction to Equation (5.2).

5.4. Fourth-order limit of diffusion equation

In order to introduce a correction to the diffusion equation, we perform a Taylor expansion of the lattice Equation (5.2) to account for higher orders. As shown by Wagner [118], the one-dimensional equation expanded to the fourth order takes the form

$$(\partial_t + v_i\partial_x)f_i^0 - \left(\tau - \frac{1}{2}\right)(\partial_t + v_i\partial_x)^2 f_i^0 + \left(\tau^2 - \tau + \frac{1}{6}\right)(\partial_t + v_i\partial_x)^3 f_i^0 - \left(\tau^3 - \frac{3}{2}\tau^2 + \frac{7}{12}\tau - \frac{1}{24}\right)(\partial_t + v_i\partial_x)^4 f_i^0 \approx \frac{1}{\tau}(f_i^0 - f_i). \quad (5.27)$$

Since we have now introduced higher-order powers into this expansion, we must utilize moments up to the fourth-order. Using the equilibrium distribution, we include the higher-order moments, which must repeat [118]:

$$\sum_i f_i^0 = \rho \quad (5.28)$$

$$\sum_i v_i f_i^0 = 0 \quad (5.29)$$

$$\sum_i v_i^2 f_i^0 = \rho\theta \quad (5.30)$$

$$\sum_i v_i^3 f_i^0 = 0 \quad (5.31)$$

$$\sum_i v_i^4 f_i^0 = \rho\theta \quad (5.32)$$

Summing over all indices of Equation (5.27) using these revised moments, we are left with

$$\partial_t \rho - A(\tau)\left(\partial_t^2 \rho + \partial_x^2 \rho\theta\right) + B(\tau)\left(\partial_t^3 \rho + 3\partial_t \partial_x^2 \rho\theta\right) - C(\tau)\left(\partial_t^4 \rho + 6\partial_t \partial_x^2 \rho\theta\right) \tag{5.33}$$

where we have defined the τ-dependent prefactors

$$A(\tau) \equiv \tau - \frac{1}{2} \tag{5.34}$$

$$B(\tau) \equiv \tau^2 - \tau + \frac{1}{6} \tag{5.35}$$

$$C(\tau) \equiv \tau^3 - \frac{3}{2}\tau^2 + \frac{7}{12}\tau - \frac{1}{24} \tag{5.36}$$

for brevity.

This form is not particularly useful since there are mixed spatial and temporal derivatives in the higher-order powers. We use the diffusion equation to write the temporal derivatives in terms of the spatial derivatives as

$$\partial_t \rho \approx \left(\tau - \frac{1}{2}\right) \partial_x^2 \rho\theta. \tag{5.37}$$

It immediately follows that

$$\partial_t^2 \rho \approx \left(\tau - \frac{1}{2}\right)^2 \partial_x^4 \rho\theta^2. \tag{5.38}$$

We can then introduce these two substitutions into Equation (5.33) and we have

$$\partial_t \rho - \left(\tau - \frac{1}{2}\right) \partial_x^2 \rho\theta - \left(\tau - \frac{1}{2}\right)^3 \partial_x^4 \rho\theta^2 + \left(\tau^2 - \tau + \frac{1}{6}\right)\left(\tau - \frac{1}{2}\right) 3\partial_x^4 \rho\theta^2 - \left(\tau^3 - \frac{3}{2}\tau^2 + \frac{7}{12}\tau - \frac{1}{24}\right) \partial_x^4 \rho\theta = 0. \tag{5.39}$$

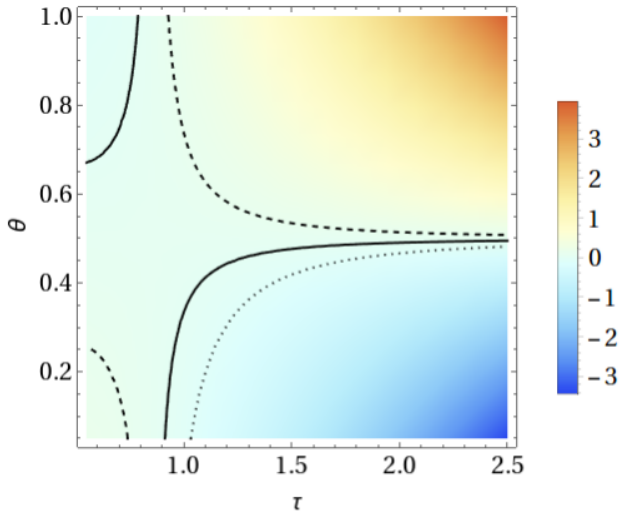

Figure 5.4. Density field representation of $\alpha(\tau,\theta)/D(\tau,\theta)$, with contour lines at values of $\alpha(\tau,\theta)/D(\tau,\theta) = 0$ (solid), $-1/\pi^2$ (dotted, predicted instability), $1/\pi^2$ (dashed, shown for symmetry).

We then obtain the form of a corrected diffusion equation

$$\partial_t \rho = D\nabla^2\rho + \alpha\nabla^4\rho \tag{5.40}$$

with corrections up to the fourth power in spatial derivatives, where we define

$$\alpha = \alpha(\tau,\theta) \equiv \left(2\tau^3\theta - \tau^3 - 3\tau^2\theta + \frac{3}{2}\tau^2 + \frac{5}{4}\tau\theta - \frac{7}{12}\tau - \frac{1}{8}\theta + \frac{1}{24}\right)\theta. \tag{5.41}$$

This definition of α represents the expected error between the second-order diffusion equation and the corrected fourth-order equation. For certain parameter values, such as $\tau = 1$ and $\theta = 1/3$, we have $\alpha = 0$, which accounts for higher accuracy observed for such parameters. We plot a density field representation of the relative error quantity $\alpha(\tau,\theta)/D(\tau\theta)$ in Figure 5.4. We indicate a contour where this quantity vanishes, as well as additional contours whose numerical importance will be explained in later sections. It is worth noting here that this derivation is performed only for the case of constant τ; however, we do not address variable τ in our applications.

The correction term has a similar form to a surface tension term in a Cahn-Hilliard equation. In this case, positive values of α would correspond to a negative surface free energy. This implies that simulations with positive α should be unstable for high frequency perturbations. This equation can be solved in Fourier space, allowing us to verify our analytical predictions with lattice Boltzmann simulations. In the subsequent section, we perform this analysis.

5.5. Fourier analysis of correction term

A Fourier transform of Equation (5.40) yields

$$\partial_t \widehat{\rho}(k,t,\alpha) = -Dk^2 \widehat{\rho}(k,t,\alpha) - \alpha k^4 \widehat{\rho}(k,t,\alpha). \tag{5.42}$$

Here k is any specific Fourier mode and $\widehat{\rho}(k,t)$ is the k-space density represented by

$$\widehat{\rho}(k) = \frac{1}{2\pi} \int_0^{L_x} \rho(x) e^{\frac{2\pi i k x}{L_x}} dx, \tag{5.43}$$

where L_x is the system size in the x-direction. Even though x is continuous, the finite periodicity of 2π causes k to be discrete. This allows for our system to contain a finite number of k modes which can be now examined independently. The form of Equation (5.42) is simple since different k modes do not couple. In k-space, the initial profile at $t = 0$ is chosen by defining $\rho(x,0)$, which for $\widehat{\rho}(k,0)$ gives Equation (5.43) and

$$\widehat{\rho}(k,t,\alpha) = \widehat{\rho}(k,0) e^{-(Dk^2 t + \alpha k^4 t)}. \tag{5.44}$$

We reproduce the uncorrected diffusion equation by setting $\alpha = 0$, obtaining

$$\widehat{\rho}(k,t,0) = \widehat{\rho}(k,0) e^{-Dk^2 t}. \tag{5.45}$$

These predictions are implemented on a discrete lattice which implies that there will be a finite number of k modes. From Equation (5.43), we have

$$k = \frac{2\pi}{L_x} \tag{5.46}$$

which implies a maximum allowed k mode when $k = \pi$ and a minimum lattice dimension of $L_x = 2$. In this finite system, we have the back transform

$$\rho(x,t) = \sum_k e^{ikx}\widehat{\rho}(k,t,\alpha). \tag{5.47}$$

It is now possible to verify this theoretical prediction by examining the decay of specific Fourier modes by imposing an initial profile

$$\rho(x,0) = \sin(kx). \tag{5.48}$$

Using this profile, the uncorrected and corrected k-space densities become, respectively,

$$\begin{aligned} \widehat{\rho}(k,t,0) &= \sin(kx)e^{-tDk^2} \\ \widehat{\rho}(k,t,\alpha) &= \sin(kx)e^{-t(Dk^2+\alpha k^4)}. \end{aligned} \tag{5.49}$$

In practice, we change k by varying the system size L_x. An interesting point to note is that when $\alpha < -\frac{D}{\pi^2}$, it is predicted that the numerical simulations would be unstable. This is predicted due to the fact that in Equation (5.49), the negative α term leads to a positive exponent and causes $\widehat{\rho}(k,t,\alpha)$ not to decay.

5.6. Numerical verification of correction term

To determine the validity of the prediction for the correction term shown in Equation (5.41), we define a ratio between the two forms of k-space density in Equation (5.49) in a

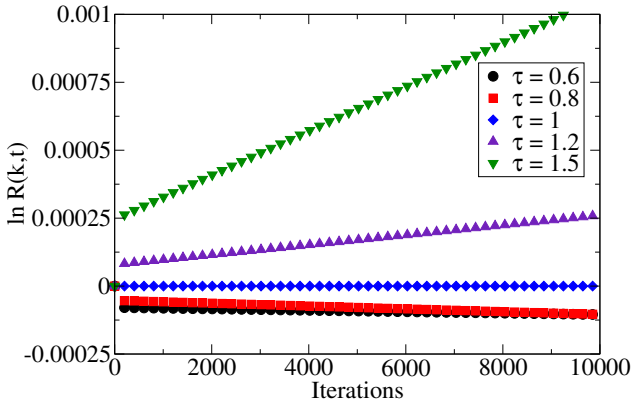

Figure 5.5. A plot of $\ln R(k,t)$ as a function of discrete time steps for various values of τ and $\theta = 1/3$ and $L_x = 200$. It is observed that there is an initial offset in $\ln R(k,t)$. As the system evolves, we see that the behavior does decay as expected. Since there is this initial offset, we cannot use these early times when calculating the derivative in Equation (5.51).

simple form such that

$$R(k,t,\alpha) \equiv \frac{\widehat{\rho}(k,t,0)}{\widehat{\rho}(k,t,\alpha)} = e^{\alpha k^4 t}. \tag{5.50}$$

We can use this relation to measure α from numerical simulations. We do this by initializing our probability distributions by $f_i(x,0) = f_i^0(\sin(2\pi x/L_x))$ and then varying L_x. Our first prediction is that $\ln(R(k,t))$ is a linear function of t. We can find α from the time evolution of the density through

$$\alpha_{\text{exp}} = \frac{1}{k^4}\frac{d}{dt}\ln R(k,t) \tag{5.51}$$

where we numerically calculate the temporal derivative using a finite difference method.

The numerical evaluation of Equation (5.50) using the numerical results is shown in Figure 5.5. At $t = 0$ we have $R = 1$ by construction, but for all $\tau \neq 1$ we observe a rapid transient change which manifests itself as a near instantaneous jump in Figure 5.5. After this transient period, the behavior of $\ln(R)$ is indeed linear, as expected. We then calculate

$$\frac{d}{dt}\ln R(k,t) \approx \frac{\ln R(k,t_2) - \ln R(k,t_1)}{t_2 - t_1}, \tag{5.52}$$

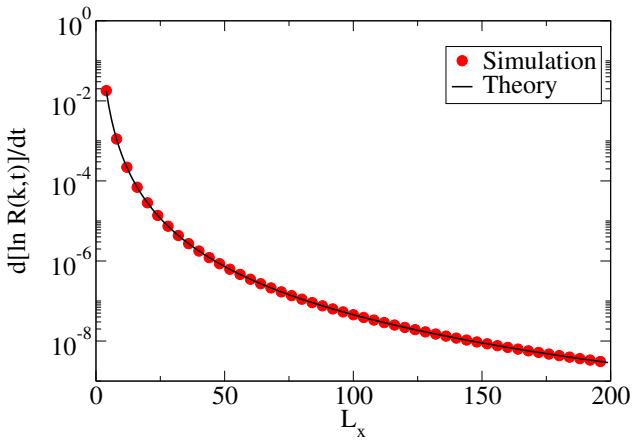

Figure 5.6. Logarithmic representation of $\frac{d}{dt}[\ln R(k,t)]$ as a function of k from simulation data for $\tau = 1$ and $\theta = 0.1$. Good agreement is observed between the simulation and the curve fit for up to $L_x = 200$.

where we take t_1 when $\widehat{\rho}(k,t,\alpha) = 0.5$ and t_2 when $\widehat{\rho}(k,t,\alpha) = 0.01$ to avoid any difficulties with the offset. Equation (5.51) gives our correction polynomial as a function of any Fourier mode k. Using this form, we can compare our predicted correction term in Equation (5.41) to a numerical representation. Figure 5.6 shows simulation data for $\frac{d}{dt}[\ln R(k,t)]$ for $\tau = 1$ and $\theta = 0.1$. We see a good fit for all k modes between simulation and the prediction in Equation (5.51).

We first test the prediction comparing α_{exp} in Equation (5.51) to our theoretical prediction for α from Equation (5.41). Figure 5.7 shows a comparison between α_{exp} and our theoretical prediction for α for various values of τ and θ as a function of L_x. For this analysis, we chose a known stable value for either τ or θ and set the other parameter as a more extreme value. For a choice of $\theta = 1/3$, we set $\tau = 0.51$ as the extreme value. In these cases, we see very good agreement between α_{exp} and our prediction. In the cases of $\theta = 1/3$ with $\tau = 1.5$ and $\theta = 0.9$ and $\tau = 1$ we observe good agreement for $L_x > 40$, but as L_x becomes smaller, deviations begin to increase. This suggests that there is a discrepancy in α_{exp} for large k modes.

In the case where $\alpha = 0$, it is interesting to note that the results match a $\frac{1}{k^6}$ rather than the predicted $\frac{1}{k^4}$ fit. This implies that there are additional correction terms which may

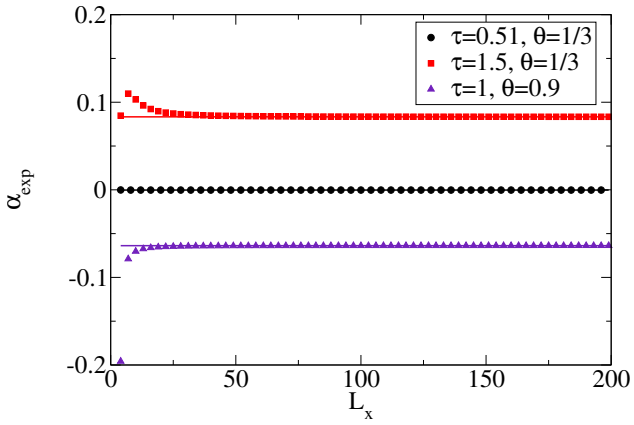

Figure 5.7. Comparison of α_{exp} (symbol) to theoretical prediction for α from Equation (5.41) (solid line) for various values of θ and τ as a function of L_x. It is observed that for $\tau = 0.51$ and $\theta = 1/3$ that α_{exp} matches the theoretical α well for all L_x. For sets of values $\tau = 1$ with $\theta = 0.9$ and $\tau = 1.5$ with $\theta = 1/3$, there is a good match for $L_x > 40$ but deviations are observed for small values of L_x.

be relevant at specific values of τ and θ. These higher-order corrections are not considered in the present analysis.

As discussed previously, Equation (5.49) predicts numerical instability when $\alpha < -\frac{D}{\pi^2}$. The density representation shown in Figure 5.4 implies that this will happen as we increase τ and decrease θ to extreme values ($\tau \gtrsim 4$ and $\theta \lesssim 0.3$ simultaneously). A contour showing $\alpha(\tau, \theta)/D(\tau, \theta) = -1/\pi^2$, the start of the region of instability, is shown in that figure.

It is instructive to examine α while holding either τ or θ fixed. Setting $\theta = \frac{1}{3}$, we examine α as a function of τ alone in Figure 5.8, which shows excellent agreement to theory over 100 independent k modes. We set $\tau = 1$ and examine α as a function of θ alone in Figure 5.9, with similarly excellent agreement.

5.7. Application of correction to reservoir diffusion

With the fourth-order correction term in hand and its correctness assured, we next determine its applicability to our reservoir coating system. Figure 5.10 shows the absolute error profile between lattice Boltzmann simulation results and a fourth-order corrected analytical solution. This solution is produced by first setting up an appropriate initial step

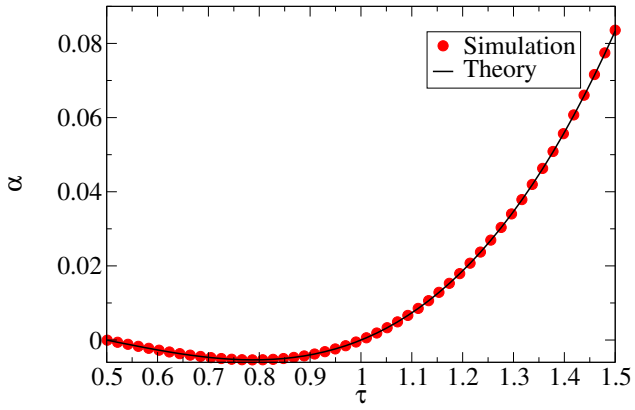

Figure 5.8. Comparison of numerical results and theoretical α as a function of τ, with $\theta = \frac{1}{3}$. Results are collected for $L_x = 100$.

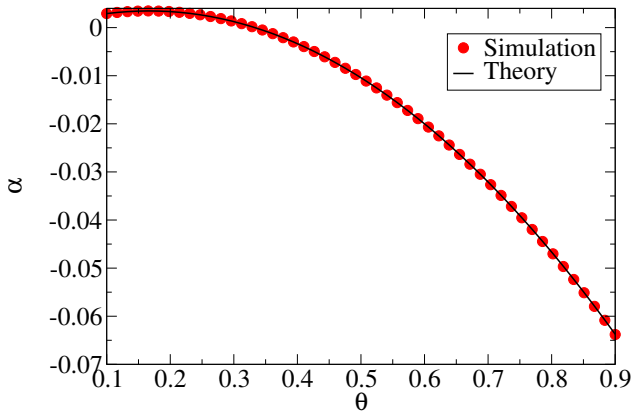

Figure 5.9. Comparison of numerical results and theoretical α as a function of θ, with $\tau = 1$. Results are collected over 100 independent k modes.

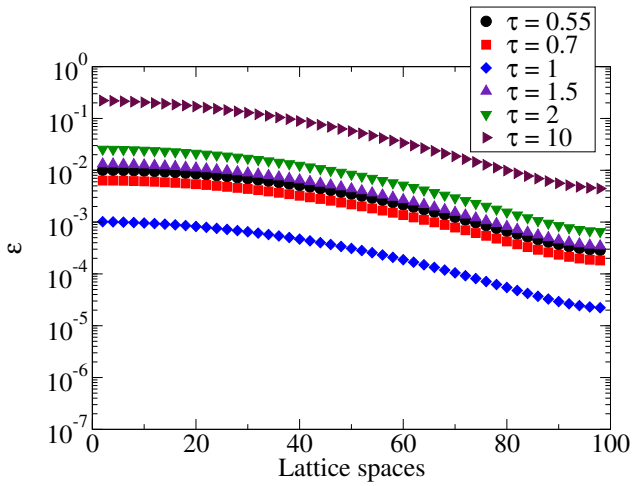

Figure 5.10. Absolute error profile ϵ between numerical and fourth-order Fourier analytical concentration at various τ. All simulations were run to the same scaled time, corresponding to four hours.

function

$$\rho(x,0) = \begin{cases} 2 & , \quad L_x < x < 3L_x \\ 1 & , \quad x = L_x \text{ or } x = 3L_x \\ 0 & , \quad \text{else} \end{cases} \tag{5.53}$$

in a periodic lattice. This is entirely equivalent to the boundary conditions implied by the derivation of the second-order error function solution in Equation (5.20). We transform this step function into k space via a discrete Fourier transform, use the fourth-order correction to perform a time evolution, and then transform the result back into real space. Strictly speaking, the method of Equation (5.20) generates a continuous solution, while the Fourier transform approach yields a discrete solution. We discuss the ramifications of this difference later and conclude that the difference in solution discretization is very small and of the same order as the error produced in our best numerical results.

We note no consistent improvement over the second-order shown in Figure 5.3 from the introduction of the fourth-order correction. However, the magnitude of the error, especially for high values of τ, is not negligible. The nature of the finite simulation lattice is such that the boundaries are treated independently of other lattice sites. In particular, the reservoir density ρ is set manually and not strictly determined by local distributions.

Since we have seen that τ-dependent errors tend to accumulate near the reservoir boundary over an order of magnitude higher than at the substrate boundary, the nature of using such a finite lattice is suspect. The case when $\tau = 1$ yielded excellent agreement throughout the finite lattice, but this is consistent with the immediate relaxation of local equilibrium distributions.

This τ-dependent error is consistent with the jump observed in Figure 5.5, where setting $f_i(x, 0) = f_i^0(\rho(x))$ led to deviations. Indeed, Equation (5.27) implies that

$$f_i = f_i^0 - \tau(\partial_t f_i^0(\rho) + v_{i\alpha}\nabla_\alpha f_i^0(\rho)) + O(\partial^2), \tag{5.54}$$

which suggests an approach that would allow us to increase the accuracy of our boundary conditions.

In our current case, however, we can avoid the cumbersome issue of the boundary condition altogether by simply embedding the system into the periodic lattice used for establishing the initial step function condition of the analytical Fourier solution. This permits a more standard lattice Boltzmann approach that does not rely on manual density adjustment at the reservoir (here at $x = 3L_x$) and uses symmetry to establish the substrate (at $x = 4L_x$) with no bounceback. We therefore expect that the τ-dependent error should be substantially reduced, especially at the reservoir boundary. Figure 5.11 shows a diagram of the periodic step function from Equation 5.53 used for this analysis.

We again run two sets of simulations for our range of τ values to the same scaled time, both using the periodically-embedded lattice simulation. The first set of simulations uses only the traditional second-order approximation and is shown in Figure 5.12. The second set applies our fourth-order correction and is shown in Figure 5.13.

As was hoped, the error at the reservoir is reduced by orders of magnitude when compared to the finite system with imposed boundaries. This confirms that the accumulated error from the finite system is due to the presence of boundary conditions that are only

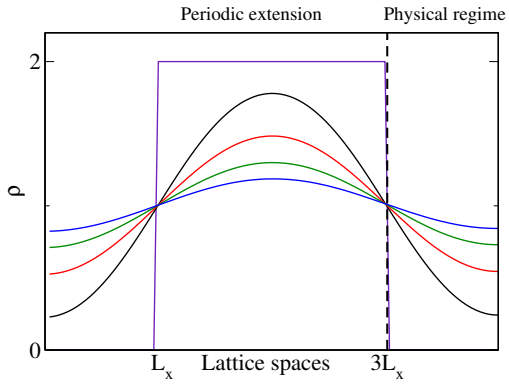

Figure 5.11. Periodic step functon from Equation 5.53, with reservoir at $x = 3L_x$ and substrate at periodic boundary $x = 4L_x$

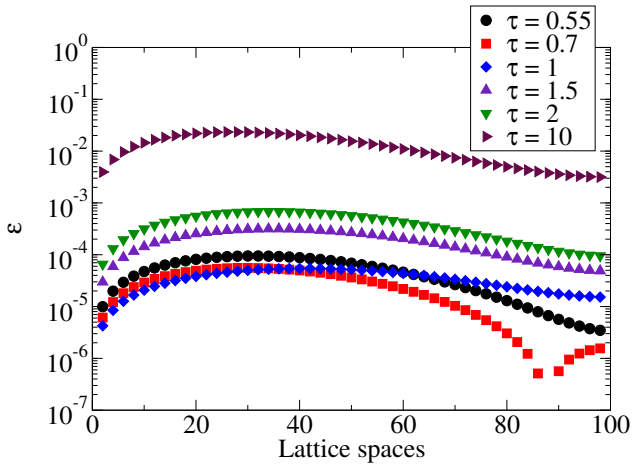

Figure 5.12. Periodic system absolute error profile ϵ between numerical and second-order Fourier analytical concentration at various τ. All simulations were run to the same scaled time, corresponding to four hours.

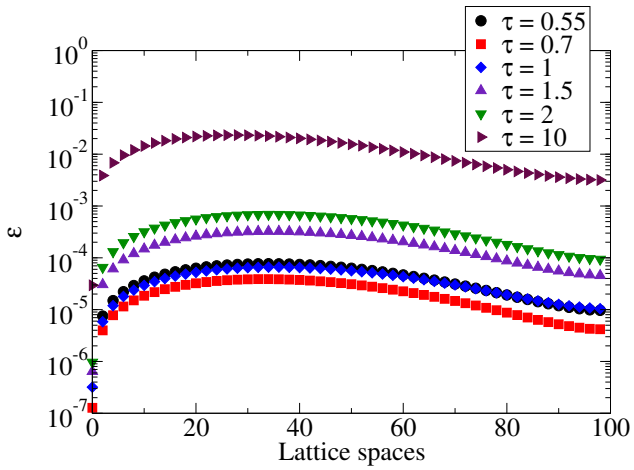

Figure 5.13. Periodic system absolute error profile ϵ between numerical and fourth-order Fourier analytical concentration at various τ. All simulations were run to the same scaled time, corresponding to four hours.

guaranteed to match at $\tau = 1$ when relaxation is immediate during collisions. However, contrary to expectation, there is almost no benefit from the fourth-order $\alpha(\tau, \theta)$ correction, even though its validity was verified via Fourier analysis.

It is of value to mention here the effects of using a progressively lower of τ, since our results suggest that errors increase with τ, regardless of the choice of boundary conditions considered. Of course, a lower choice of this parameter leads to increasingly long simulations, which must be balanced with the desired numerical accuracy. We examined a range of τ values as low as $\tau = 0.5001$ and found essentially no change in error from the $\tau = 0.55$ lower limit presented throughout this paper. This suggests that (to within machine accuracy), there is likely no theoretical limit to the ratio of diffusion constants possible. This implies that a study of a multi-layer coating stack, which fixes the diffusivity ratio through a selection of τ values, is possible for a situation where one coating's diffusion constant is orders of magnitude higher than the other.

It is natural at this point to wonder if there are any choices of parameters τ and θ for which the fourth-order correction provides substantial benefit in our reservoir problem, especially since its use in simulations incurs additional computational burden. Naturally, any such error analysis depends heavily on the particular problem of interest, and therefore

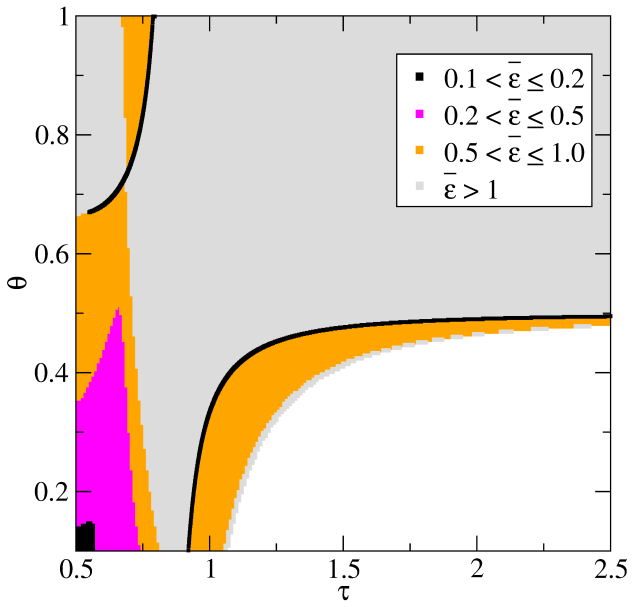

Figure 5.14. Error ratio $\bar{\epsilon}$, indicating bands comparing the second- and fourth-order Fourier solution accuracy. All simulations were run to the same scaled time, corresponding to a macroscopic system time of 3.5 seconds. Also shown is the $\alpha(\tau, \theta) = 0$ contour (black line).

on the initial profile and desired time evolution. For our system, we examine the parameter space $0.5 < \tau \leq 2.5$ and $0.1 \leq \theta \leq 1.0$. For each point in this space, we run a lattice Boltzmann periodic reservoir system simulation to the same scaled time. After this time, we compute the ratio

$$\bar{\epsilon} \equiv \frac{\epsilon_4(\tau, \theta)}{\epsilon_2(\tau, \theta)}, \tag{5.55}$$

where

$$\epsilon_{2,4} \equiv \sqrt{\frac{1}{L_x} \sum_{x=1}^{L_x} \left[\rho(x) - \rho_{2,4}(x)\right]^2} \tag{5.56}$$

is the root mean square error between numerical concentration ρ and second- or fourth-order Fourier analytical concentration $\rho_{2,4}$. If $\bar{\epsilon} \approx 1$, there is no appreciable correction from using the fourth-order solution; as $\bar{\epsilon} \to 0$, the correction becomes more substantial. From a computational perspective, there is a trade-off between the computational burden of the correction and the benefit (if any) from using it. We do not comment on the appropriate balance for any particular situation.

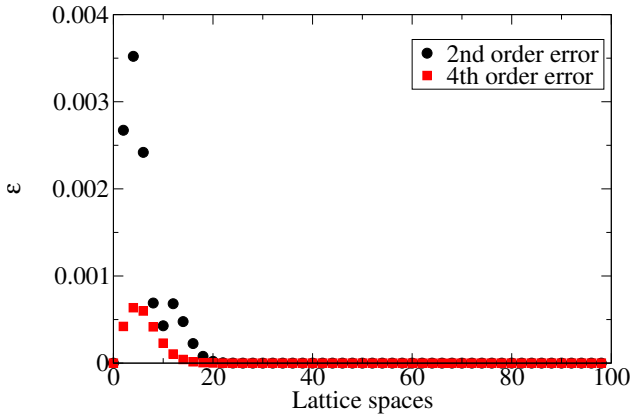

Figure 5.15. Absolute error between numerical simulation results and second-order Fourier (circles) and fourth-order Fourier (squares) analytical solutions. Simulation was run with $\tau = 0.55$ and $\theta = 0.15$ to the macroscopic equivalent time of 3.5 seconds.

Contrary to expectation, there are no regions of the given parameter space where $\bar{\epsilon} < 0.9$ during long times, indicating no appreciable benefit to the correction. Further, the fourth-order analysis predicts numerical instability in the bulk region of parameter space where $\alpha < -1/\pi^2$, although the numerical simulations and second-order analysis remain stable. This is a surprising result overall: a fourth-order correction is not only unhelpful in increasing the accuracy of these solutions at long times, it is often worse than the second-order approximation and predicts numerical problems incorrectly.

If we instead run the same analysis for a much shorter time (in the equivalent macroscopic system, just 3.5 seconds), the results are more promising and shown in Figure 5.14. For small values of both τ and θ, the fourth-order correction increases accuracy by an order of magnitude. This is largely due to the fact that the fourth-order theory accurately predicts some early time oscillations at the sharp reservoir interface, as shown by the error reduction in Figure 5.15. This discussion of higher-order effects gives the rather surprising result that for our barrier coating application, there is no noticeable improvement. This may also arise because even the second-order results are accurate enough that any resulting errors are of the same order of magnitude as the difference between continuous and discrete analytical solutions, as shown in Figure 5.17 in the Appendix.

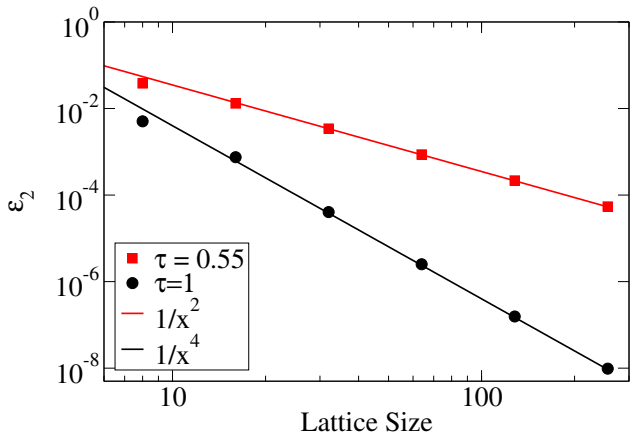

Figure 5.16. Convergence of our simulation results for different lattice sizes. For pairs (τ, θ) for which we have $\alpha = 0$, we obtain fourth-order convergence, whereas we obtain second-order convergence where $\alpha \neq 0$ as predicted by our theory.

There is another prediction we can obtain from our derivation of the correction term. In Figure 5.14, we see bold black lines indicating the domain for $\alpha(\tau, \theta) = 0$. For these values, our theory predicts that the original method (derived only to second order) is actually a fourth-order method. To test this prediction, we choose $\tau = 1$ and $\theta = 1/3$ for which we have $\alpha = 0$, and examine the convergence of the method to the Fourier term analytical solution ϵ_2 of Equation (5.56). In particular, we examine the same periodic system as before by choosing $F = 0.0576$ for different lattice sizes. Keeping F constant implies that the number of iterations scales as the square of the lattice size, which is sometimes known as diffusive scaling. This is shown in Figure 5.16, where we see that we indeed find fourth-order convergence when $\alpha = 0$. For pairs of τ and θ for which we have nonzero correction terms (e.g. we show the case $\tau = 0.55$ and $\theta = 1/3$), we see that we have a second-order convergence instead.

5.7.1. Continuous and discrete solutions

The error function solution in Equation (5.20) solves the second-order diffusion equation with the given boundary conditions in continuous real space (see [31] for a basic form of the derivation). However, we later compute a solution by transforming the appropriate initial condition into Fourier space, performing a second-order time evolution, and then transform-

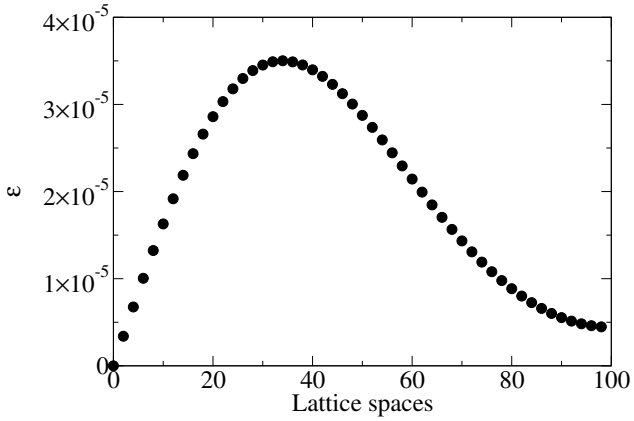

Figure 5.17. Absolute error profile ϵ between second-order error function and second-order Fourier solutions to the continuous and discrete diffusion equation, respectively.

ing back into real space. This process uses a finite number of k modes in each transform, and necessarily implies a discrete lattice sampling of both the initial condition in real space and the time-evolved form in Fourier space. We therefore expect a discrepancy when directly comparing the two solutions: the first is a solution to the continuous diffusion equation that is examined at discrete lattice points for comparison to the simulation, while the second is a sampled solution to the discrete lattice diffusion equation, the continuous form of which would require (in theory) an infinite number of k modes to match the continuous case.

To examine the extent to which these solution forms differ from each other, we compute both at the same scaled four-hour time at each lattice site, and plot the absolute value of the difference, ϵ, in Figure 5.17. The two solutions agree to within 10^{-5} of each other. Since this error is on the order of the remaining error for the periodically-embedded simulation, we conclude that any further correction of simulation results renders any error obscured by differences between the discrete and continuous solutions to the diffusion equation, and is of no practical consequence.

5.7.2. Algorithm efficiency

For a given dimensionless constant F, it is natural to question the efficiency of the algorithm over a range of scaled real-world parameters. In this work, a value $F = 0.0576$ was chosen for a representative coating sample with diffusion constant $D = 10^{-14}$ m^2/s. With

this value set and our choice of 100 lattice spaces in the simulation, the parameters τ and θ set the time scale. A higher value of τ allows for a smaller number of timesteps for a given real-world time interval, but introduces more error. Conversely, a smaller τ yields lower error but increases the number of timesteps required. For a single coating, parameter scaling makes the choice of τ arbitrary for analytical purposes, but a multiple-layer arrangement may require this.

By way of example, a choice of $\tau = 1.0$ sets the time scale at approximately 576 timesteps per hour of corresponding laboratory time. On the author's office computer, the simulation running on a single core of an Intel Core i3-4150 3.50 GHz processor is able to process one year of laboratory time in 6 seconds.

If we set $\tau = 0.55$ (much closer to its lower limit), the timescale is set to 5760 timesteps per hour of laboratory time, and the same one-year test takes approximately 84 seconds to run.

5.8. Conclusions

We have examined whether a diffusive lattice Boltzmann method is an effective tool for examining problems related to Fickian water diffusion in barrier coatings. This validation was assisted by our ability to derive an analytical solution for a simple, but not trivial, coatings problem. In Section 5.3 we presented a real-space solution for the water content of a dry coating that is initially exposed to a constant moisture reservoir on the surface. A second analytical solution in terms of Fourier components was presented in Section 5.5 that can be used both for the standard Fickian diffusion case already examined in Section 5.3, as well as the more complex fourth-order diffusion equation we derived as part of a higher-order hydrodynamic limit of the lattice Boltzmann equation. The two equivalent analytical solutions differ slightly because our Fourier series corresponds to a discrete system with only a finite number of Fourier terms.

For a simple initial implementation of the inlet boundary, we found excellent agreement only for a relaxation time $\tau = 1$. Our analysis revealed that the disagreement for $\tau \neq 1$

was caused by assuming an equilibrium distribution as the reservoir boundary condition. Eventually we were able to define a "perfect" boundary condition by doing away with the boundary altogether through an embedding of the system in a large periodic system that only requires periodic boundary conditions.

Along the way of our examination, we discovered that we can indeed identify a fourth-order accurate hydrodynamic limit of the diffusion equation. However, this higher-order correction was found to be irrelevant for the coatings problem considered here, as we could only identify a small region in parameter space where the fourth-order predictions were significantly more accurate. This may act as a cautionary tale that validating a higher-order correction does not guarantee that such predictions will always be more accurate for specific applications.

However, for the best cases, the numerical solutions agree with our analytical solutions almost as well as the two analytical solutions agree with each other, suggesting that the proposed method is indeed an excellent candidate to be applied to coatings problems.

In the future we expect to extend this from one-dimensional coatings problems, corresponding to full immersion of the coating, to the more complicated problem of droplets sitting on a coating. This case will require a full three-dimensional simulation, and wetting and drying problems then occur in one and the same simulation, spatially separated. Furthermore a droplet sitting on a coating would add a pressure gradient caused by the Laplace pressure in the drop. This may lead to an additional transport mode of advection, driven by the pressure gradient. This will require an extension of the current model to allow for some amount of advection as well. This advection would be expected to be highly overdamped, so that the local advection velocity would be simply proportional to the local pressure gradient. Technically doing this will require a replacement of the equilibrium distribution to one which allows for a non-zero first moment. Such simulations will significantly extend the current state of the art for coatings research which remains firmly focused on one-dimensional problems.

6. EFFECT OF CONCENTRATION-DEPENDENT DIFFUSIVITY ON CYCLIC MOISTURE EXPOSURE

6.1. Introduction

An idealized coating is modeled that is adhered to an impermeable substrate and exposed to either a moisture reservoir or to air. This models the common use case where a coating might be applied to an airframe or automobile, and thereafter be exposed to the elements in a cycled fashion [108]. Additionally, it models the cycled environmental exposure that most coating systems undergo in test chambers during laboratory testing, where the coating might experience repeated cycles of water misting followed by dry exposure to ultraviolet radiation. Parameters like temperature, timing, and radiation intensity of each cycle segment vary depending on the testing protocol; perhaps unsurprisingly, most protocols align cycle times with the workday (*e.g.* 8, 12, or 24 hours) to more easily accommodate predictable personnel availability.

In this chapter, we extend the lattice Boltzmann method of the previous chapter to the problem of a single-layer coating exposed to a variable reservoir and perfectly adhered to an impermeable substrate. We use Fickian diffusion to examine the kinetics of wetting and drying over time, and provide a simple scaling argument that permits us to extend the model to a variety of experimental setups and parameters. We introduce reservoir cycling to determine the effects on substrate wetting and eventual oscillatory steady-state behavior.

It is understood that in many polymeric materials, the diffusion coefficient is not constant with concentration, often with large deviations [37]. Under the influence of moisture

The work in this chapter was completed by the author and A.J. Wagner in a published paper [119]. Mathematical analysis was completed by the author. Simulations were designed and completed by the author, with additional analysis from Wagner.

(like water), the material swells and permits penetrants to diffuse more quickly than in the non-swollen state. Models for this phenomenon range from a "sharp front" model to a more gradual increase in diffusion coefficient. Due to the lack of a unified theory of concentration dependence, several common cases are considered for this dependence of the diffusivity: idealized constant diffusivity, a step function induced by instantaneous network swelling, and a linear dependence induced by gradual swelling. Variable cycle time ratios are considered throughout. We conclude by proposing material properties for coatings that may be particularly beneficial to limit corrosion.

6.2. Theory

In this section, we show the derivation of an analytical solution to the diffusion equation with correct boundary conditions. We then outline the numerical lattice Boltzmann method used for subsequent results.

6.2.1. Analytical

As in the previous chapter, the coating panel is modeled as a simple one-dimensional system bounded by an infinite reservoir and impermeable reflecting substrate. We initially examine constant diffusivity, a detailed examination of which has been presented. As we discuss later, however, polymer network swelling under the influence of a solvent may lead to concentration-dependent diffusivity, where such a simplification to the diffusion equation is no longer possible.

The model one-dimensional coating system extends in the range $0 \leq x \leq L$ for coating thickness L. At $x = 0$ is a reservoir whose concentration may vary with time. At $x = L$ is an impermeable substrate where the concentration gradient is always zero. No particular assumptions are made regarding the adhesion of the coating to the substrate, and the coating is assumed to have uniform density and saturation capacity.

The concentration solution used in the previous chapter assumes the reservoir remains at fixed concentration, modeling the case where the coating undergoes constant exposure and is eventually saturated to concentration $\rho_{\text{exp}}(0 \leq x \leq L, t \to \infty) = \rho_0$. Suppose that instead,

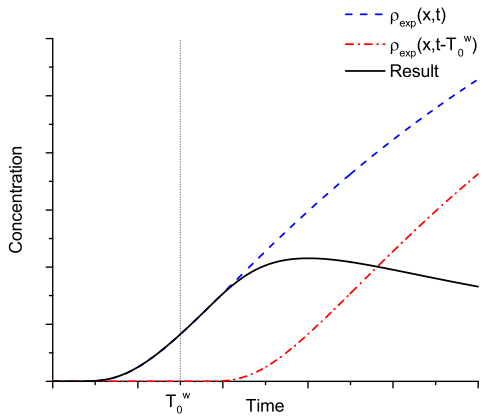

Figure 6.1. Construction of single-cycle concentration at lattice position $x = L/2$, showing constant-exposure $\rho_{\exp}(x,t)$ (dashed blue), time-shifted constant-exposure $\rho_{\exp}(x, t - T_0^w)$ (dot-dashed red), and resulting difference (solid black)

the reservoir is removed at some time T_0^w and the coating is allowed to dry. We may express the concentration over time by modifying the result. If we let $\rho_{\exp}(x, t < 0) = 0$, then the concentration at any time (before or after the reservoir is removed) may be expressed by the superposition

$$\rho_1(x,t) \equiv \rho_{\exp}(x,t) - \rho_{\exp}(x, t - T_0^w). \tag{6.1}$$

Figure 6.1 shows the construction of this expression at a representative position over time (arbitrary units). This is the correct solution to the linear partial differential diffusion equation since it is a superposition of known solutions that matches the required boundary conditions in space and time:

$$\rho_1(x, t = 0) = 0 \tag{6.2}$$

$$\nabla\rho_1(x = L, t) = 0 \tag{6.3}$$

$$\rho_1(x = 0, t < 0) = 0 \tag{6.4}$$

$$\rho_1(x = 0, 0 \leq t < T_0^w) = \rho_0 \tag{6.5}$$

$$\rho_1(x = 0, t \geq T_0^w) = 0 \tag{6.6}$$

In the general case where the wet and dry timings are arbitrary and not necessarily constant between cycles, let $T_0^w, T_1^w, \ldots$ be the lengths of each wet period, and $T_0^d, T_1^d, \ldots$ the lengths of each dry period. That is, the reservoir turns on at times $t = 0, (T_0^w + T_0^d), (T_0^w + T_0^d + T_1^w + T_1^d), \ldots$ according to the given timings. The solution then becomes

$$\rho_{\text{cycle}}(x,t) = \rho_{\text{exp}}(x,t) + \sum_{i=1}^{\infty}\left[\rho_{\text{exp}}(x, t - t_i^w) - \rho_{\text{exp}}(x, t - t_i^d)\right] \tag{6.7}$$

where we define the partial sums $t_i^w = \sum_{j=0}^{i}(T_j^w + T_j^d)$ and $t_i^d = t_i^w - T_i^d$. This is the correct solution if we add additional boundary conditions for each cycle:

$$\begin{aligned}
\rho_{\text{cycle}}(x = 0, T_0^w \le t < T_0^w + T_0^d) &= 0 && (6.8)\\
\rho_{\text{cycle}}(x = 0, T_0^w + T_0^d \le t < T_0^w + T_0^d + T_1^w) &= \rho_0 && (6.9)\\
\rho_{\text{cycle}}(x = 0, T_0^w + T_0^d + T_1^w \le t < T_0^w + T_0^d + T_1^w + T_1^d) &= 0 && (6.10)\\
&\vdots
\end{aligned}$$

6.2.2. Lattice Boltzmann

The analytical theory gives the precise concentration throughout the coating at any time for the case of constant diffusivity, regardless of the reservoir cycling used. However, it does not easily accommodate the scenario where diffusivity within a coating layer varies with concentration due to polymer network swelling under the influence of a solvent.

To incorporate polymer swelling, we employ the diffusive lattice Boltzmann method previously introduced. Because boundary conditions were shown to have a large effect on overall error, these are discussed in more detail below.

6.2.3. Boundary conditions

The substrate underlying the coating in our model is assumed to be impermeable, so we use a reflection condition for lattice density evolution there. After each collision, any f_1 outflow attempting to pass through the substrate at $x = L$ is reflected back as f_{-1}

inflow to the adjacent lattice site. Since this means the boundary is effectively located half a lattice space outward, the corresponding analytical solution is slightly modified to assume the system is correspondingly longer.

In the previous chapter, it was shown that the choice of reservoir boundary condition is critical for determining the overall numerical error, especially near the boundary and at early times. In particular, manually setting the reservoir boundary lattice densities $\{f_i\}$ to the equilibrium distribution value at each timestep resulted in substantially larger errors. One proposed solution, that of embedding of the system into a periodic lattice where such boundary conditions are replaced by symmetric initial conditions (as in the previous chapter), removes such error almost completely.

Extending this embedding to time-dependent boundary conditions (such as reservoir cycling) is possible, but we found an even simpler way of defining an inflow boundary condition in the finite lattice that retains the accuracy of the periodic embedding and keeps the system size smaller for computational efficiency. The reservoir boundary condition is modified to reflect f_{-1} outflow densities about the current reservoir concentration to f_1 inflow, instead of using the equilibrium distribution value:

$$f_1(x=0) = 2\rho_0\frac{\theta}{2} - f_{-1}(x=0) \tag{6.11}$$

It was found that this boundary condition retains the same numerical accuracy as a periodic embedding.

Due to parameter scaling, a single coating layer whose diffusivity is constant is trivial to model, since any choice of parameters τ and θ is analytically equivalent. However, the previous chapter showed that straying from $\tau = 1.0$ to higher values introduces rapidly increasing error, suggesting that $\tau = 1.0$ is a reasonable choice for this application. For this work, we use $\tau = 1.0$ and $\theta = 0.5$ when constant diffusivity is assumed, and scale to values $\tau \leq 1.0$ when working with non-constant diffusivity.

Many barrier coatings exhibit swelling, where the presence of solvent causes the crosslinked polymer network to expand and permit faster moisture ingress and egress. Conversely, one might imagine a metamaterial designed such that increased concentration reduces the effective diffusivity. Analytically, either case corresponds to defining $D = D(\rho)$ according to some functional form. There is no known unified model for this swelling behavior from first principles [37], but two common models of polymer swelling are a step function front and linear diffusivity [35]. In the step function model, the coating is assumed to be in a dry state when at low moisture concentration until a critical concentration is reached, above which it is in a wet state and at a different diffusivity. This means $D(\rho)$ takes the form of a step function. The other common functional form is that of a linear function, such that diffusivity varies monotonically with concentration. We consider both cases in the subsequent analysis.

6.3. Results and discussion

6.3.1. Constant diffusivity

A typical single-layer barrier coating might be applied with thickness 50 μm to a test panel, have a diffusion constant in water of $D \sim 10^{-14}$ m^2/s, and be exposed to moisture in an environmental chamber for four hours (14400 s). This corresponds to a dimensionless constant $F = 5.76 \times 10^{-2}$, as in the previous chapter. For simulations, we choose a lattice of size $L = 100$ lattice points, reservoir concentration $\rho_0 = 1$, relaxation time $\tau = 1.0$, and $\theta = 0.5$. This means that four hours of moisture exposure in the macroscopic system corresponds to $T \approx 3500$ timesteps in the lattice Boltzmann system. It should be noted that diffusion constants for water through barrier coatings may vary greatly, with values that may range as low as 10^{-16} m^2/s; due to the ease of scaling the problem, this does not pose a significant issue for our analysis.

We previously showed that this setup results in excellent numerical accuracy for moisture exposure over long times, typically on the order of 0.01% of the predicted theory value, several orders of magnitude better than typical experimental measurements. To verify

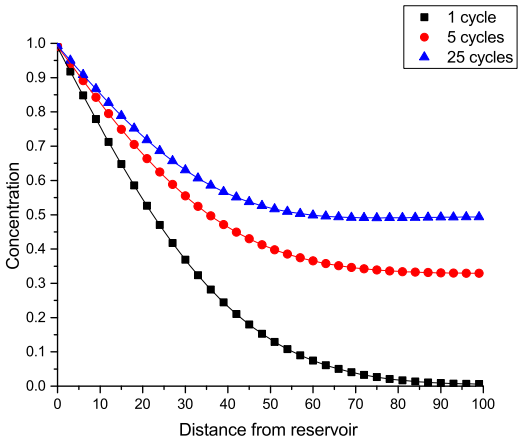

Figure 6.2. Numerical (symbols) and theoretical (Equation 6.7) (lines) concentration at the end of wet cycles over simulation lattice

that cycling the reservoir, which introduces large concentration gradients near the reservoir, retains the desired numerical accuracy to theory, we run a lattice Boltzmann simulation with the given parameters, cycling the reservoir on and off every T timesteps for a total cycle period of $2T$ timesteps. Snapshots of the lattice and corresponding theory from Equation 6.7 are shown in Figure 6.2 for the end of wet cycles (just before the reservoir turns off), and in Figure 6.3 for the end of dry cycles (just before the reservoir turns on). Even at longer times when the coating concentration reaches full saturation, the numerical solution shows excellent matching to theory.

The onset of corrosion is commonly expected once the substrate becomes sufficiently wet. However, it remains an open question at what moisture content corrosion onset is expected. We examine the substrate concentration as it evolves toward a periodic late-time regime by fixing the total wet-and-dry cycle length at $2T = 7000$ timesteps (equivalent to eight hours in the corresponding macroscopic system) and varying the wet-to-dry cycle time ratio. In the periodic late-time regime, the inflow and outflow at any point in the lattice occur at the same rate. The concentration averaged over a period is the same throughout the lattice. Since the concentration oscillates about a value that is determined by the relative time-averaged concentration at the reservoir, we also know that this will be the same average

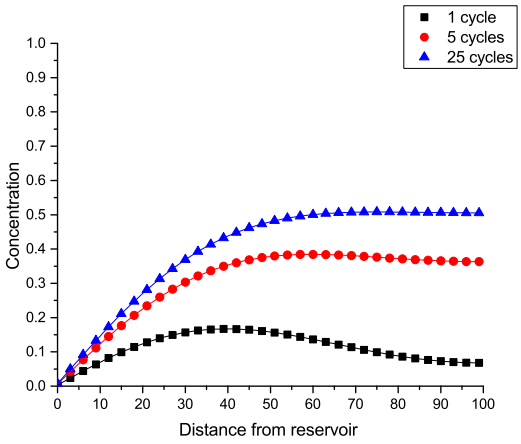

Figure 6.3. Numerical (symbols) and theoretical (lines) concentration at the end of dry cycles over simulation lattice

value at the substrate. That is, for a wet-to-dry cycle ratio of 1:R_t for some ratio R_t, the late-time average concentration value should be $1/(R_t + 1)$.

For simulations, we divide the time evolution into windows of length $10T$, where for a given set of simulation parameters T depends on τ and θ, which in turn are set by the choice of diffusion constant D; we say the system has reached a steady state when the maximum and minimum values within a window are within 0.01 of the values in the next window. For reference, with a 1:1 cycle time ratio, the system comes within 2% of the asymptotic value after about 13 full moisture cycles, corresponding in our equivalent macroscopic system to slightly over four days of cycled exposure. We then compute the average substrate concentration from that point. Results are shown in Figure 6.4. Reassuringly, the final concentration scales precisely with the cycle time ratio.

6.3.2. Variable diffusivity: step function

Diffusion of water through some polymeric coatings may be modeled by an instantaneous change in diffusivity that occurs at a particular critical concentration ρ_c. The diffusivity $D(\rho)$ takes on a constant value D_{dry} below ρ_c, and another value D_{wet} above ρ_c. When examining a single-layer coating in this way, we therefore have a three-parameter step

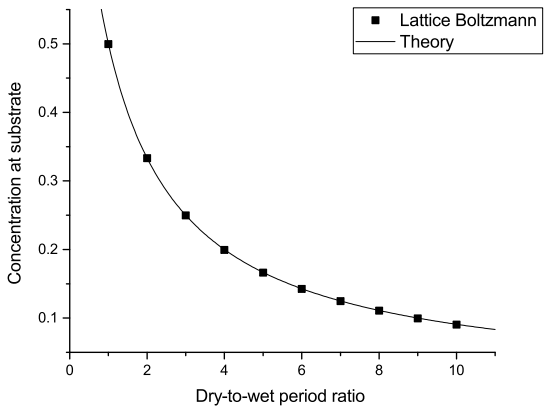

Figure 6.4. Constant diffusivity steady-state average substrate concentration (symbols) with varying wet-to-dry cycle timings and total cycle length $2T = 7000$ timesteps, with comparison to $1/(R_t + 1)$ theory (line)

function:

$$D(\rho) = \begin{cases} D_{\text{dry}}, & \rho < \rho_c \\ D_{\text{wet}}, & \rho \geq \rho_c \end{cases} \tag{6.12}$$

However, for our choice of dimensionless constant F in which oscillations at the substrate are small, we need only be concerned with wet and dry diffusion constant ratios due to parameter scaling. It suffices to reduce to a two-parameter function where the saturated diffusivity is scaled

$$R \equiv \frac{D_{\text{wet}}}{D_{\text{dry}}} \tag{6.13}$$

from the dry value. Most polymeric materials swell under the influence of solvent and permit faster moisture transport, so in this model such coatings would have $R > 1$. We also present results for $R < 1$, and discuss the implications in Section 6.4.

In simulations, we set the diffusion constant for one concentration range using $\tau = 1.0$ and $\theta = 0.5$, and set the value for the other τ lower to achieve the proper diffusion constant for that ratio R:

$$\tau = \frac{D}{\theta} + \frac{1}{2} = \frac{4D + 1}{2} \tag{6.14}$$

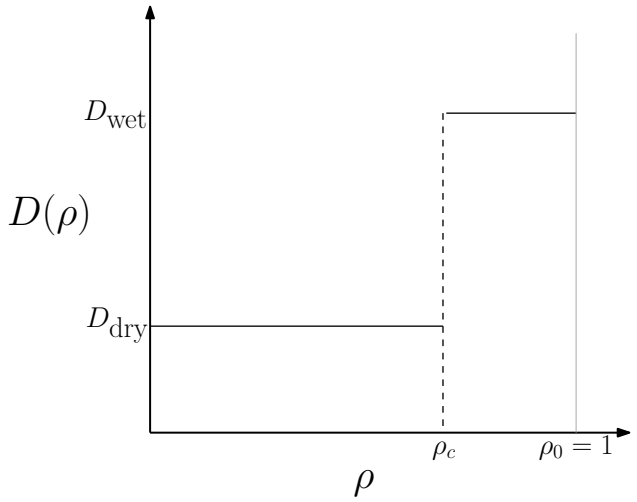

Figure 6.5. Three-parameter step function $D(\rho)$, indicating two diffusivity values and critical concentration

As discussed previously, this minimizes numerical error. Figure 6.5 shows a diagram of such a step function.

Unlike in the constant diffusivity case, we now have two regimes of interest: dry and wet. It is instructive to consider the expected behavior of extreme values for the step function $D(\rho)$. First, in the asymptotic (but nonphysical) case where $\rho_c \to 0$, the polymer is always in the wet state, and exhibits the same behavior as in the case of constant diffusivity; the long-time periodic substrate concentration must therefore scale with the cycle timings. Similarly, if $\rho_c \to \rho_0 = 1$, the polymer is always in the dry state, with the same result. The only difference between the two scenarios lies in the constant diffusivity value in the regime of interest, which reduces to a scaling problem corresponding to a different value of the dimensionless constant F, and therefore provides no new information about the system.

In the range $0 < \rho_c < 1$, the behavior is less obvious. One expects a higher periodic substrate concentration in this range for $R > 1$ due to the presence of variable timescales, but it is not immediately clear what form the effect should take. We examine a range of diffusivity ratios R numerically. For each, we ran a series of lattice Boltzmann simulations that vary the critical concentration $0 < \rho_c < 1$ and determine the substrate concentration oscillatory behavior at long times for cycle wet-to-dry ratios of 1:1, 1:2, 1:3, and 1:4, with

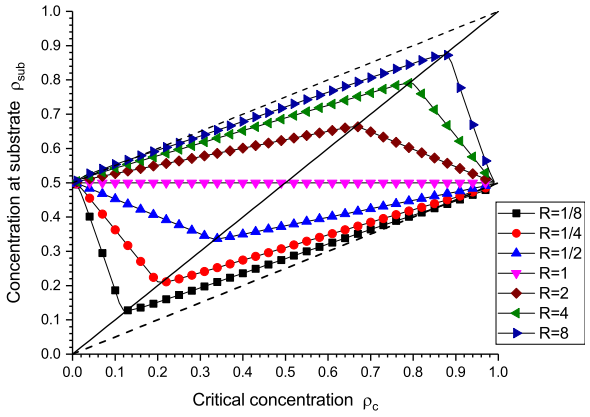

Figure 6.6. Concentration at substrate ρ_{sub} versus step function critical concentration ρ_c for selected diffusivity ratios R; all simulations use 1:1 cycle timing ratio. Peaks occur on the solid line $\rho_{\text{sub}} = \rho_c$, and dashed lines represent the asymptotic values for $R \to \infty$ and $R \to 0$

the cycle timescale set by the fixed lower diffusivity. Since oscillations were found to be sufficiently small for the constant diffusivity case with $\tau = 1.0$, scaling to a lower value of τ does not pose any problems. While we ran the simulations for many diffusivity ratios, we plot the time-averaged steady-state results for only a representative few in Figure 6.6 for the 1:1 cycle ratio to illustrate the behavior.

The results for $\rho_c \to 0$ and $\rho_c \to \rho_0 = 1$ are clear; when the coating is either always dry or always wet, the resulting concentration scales precisely with the cycle timings regardless of the actual value of the diffusion constant used. Interestingly, the intermediate behavior shows two distinct linear regimes. For any given diffusivity ratio (*i.e.* on one of the curves in Figure 6.6), there is a maximal time-averaged substrate wetting for $R > 1$, and a minimal wetting for $R < 1$. Further, these extreme values lie on the solid line $\rho_{\text{sub}} = \rho_c$ shown in the figure, implying that this occurs precisely at the corresponding swelling critical concentration.

An interesting asymptotic case occurs when either $R \to \infty$ or $R \to 0$. This corresponds to the coating having extremely low (resp. high) diffusivity before reaching the critical concentration; that is, when $D_{\text{dry}} \to 0$ (resp. $D_{\text{wet}} \to 0$). Effectively, this is equivalent to a scaled system whose concentration is allowed to vary only in the range $\rho_c \leq \rho \leq \rho_0 = 1$

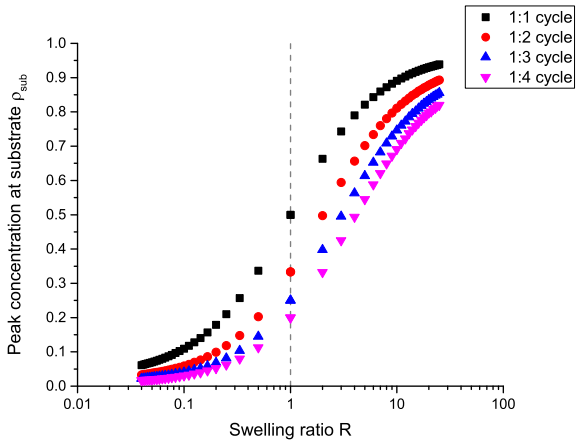

Figure 6.7. Step function model extreme concentration at substrate ρ_{sub} versus diffusivity ratio R, given for multiple cycle timing ratios; values at $R = 1$ (dashed) follow cycle timing ratio

for $R \to \infty$, or in the range $0 \leq \rho \leq \rho_c$ for $R \to 0$. In such a system, the eventual periodic concentration at the substrate must follow the dashed lines $\rho_{\text{sub}} = \frac{\rho_0}{2}(1 + \rho_c)$ for $R \to \infty$, or $\rho_{\text{sub}} = \frac{\rho_0}{2}\rho_c$ for $R \to 0$, shown in Figure 6.6.

What is unclear from first principles, however, is how the extreme substrate concentration value varies with either the diffusivity ratio or the cycle timing ratio. Figure 6.7 plots the location of these extrema as a function of diffusivity ratio.

The values for $R = 1$, corresponding to the constant-diffusivity case, exhibit the cycle timing ratio scaling discussed earlier. When the coating is allowed to dry for increasing time intervals relative to wetting, the extreme substrate wetting is reduced for all R; however, this reduction is far less effective farther from $R = 1$. In any case, both the step function magnitude and cycle time ratio play a large role in the "worst-case" substrate wetting that can arise for larger diffusivity ratios. We discuss the range $R < 1$ in Section 6.4.

6.3.3. Variable diffusivity: linear

While a step function represents a simple and useful model for concentration-dependent diffusivity arising from polymer network swelling, it is not the only such model. Most polymer networks exhibit a more gradual swelling behavior, making a step function only an approximation to physical behavior.

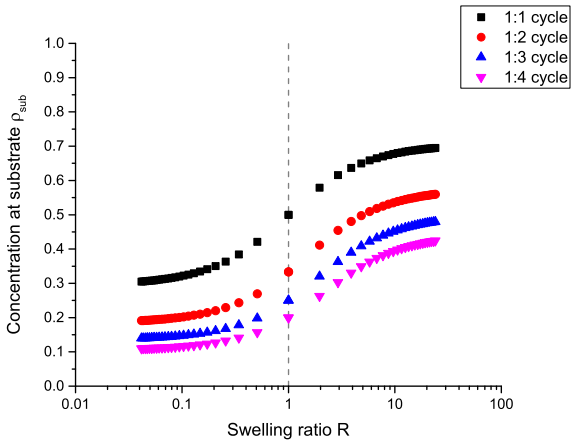

Figure 6.8. Linear model concentration at substrate ρ_{sub} versus diffusivity ratio R, given for multiple cycle timing ratios; values at $R = 1$ (dashed) follow cycle timing ratio

We consider here the effect of a linear change to diffusivity. In this model, the completely dry coating permits the slowest (but nonzero) moisture transport rate, which increases linearly to the fastest rate when fully saturated:

$$D = D(\rho) = (D_{\text{wet}} - D_{\text{dry}})\rho + D_{\text{dry}} \tag{6.15}$$

$$= D_{\text{dry}}\left[(R-1)\rho + 1\right] \tag{6.16}$$

Materials for which $R < 1$ result in a negative slope, discussed further in Section 6.4. Analysis of this linear model is in some sense a simpler process, since it reduces to a single parameter R.

Similarly to the step function case, we run a series of lattice Boltzmann simulations that fix the dry diffusivity using Equation 6.14 and vary the saturated diffusivity (effectively setting the slope of the linear dependence). The simulations run cycle time ratios of 1:1, 1:2, 1:3, and 1:4, with the overall cycle time fixed and the timescale set by the average of the two diffusivity values. We allow the system to reach long-time periodic behavior and examine the substrate time-averaged concentration. Figure 6.8 shows the time-averaged value of the substrate long-time oscillations for varying diffusivity and cycle time ratios.

Even though the diffusivity values at the dry and saturated extremes are chosen to be the same for both the step function and linear models for any given ratio R, the behavior is markedly different. For any given diffusivity ratio, the resulting concentration values in the linear model are more closely clustered near the $R = 1$ value than their step function extreme value counterparts.

6.4. Application to optimal material properties

We have so far discussed the effects of a diffusivity ratio $R > 1$; that is, when a swollen coating permits faster moisture transport, either by an instantaneous increase in diffusivity at a critical concentration or more gradually in a linear manner. However, it is insightful to consider the symmetric case when $R < 1$. This corresponds in the step function model to reversing the roles of the wet and dry constant values, and in the linear model to a negative slope. This would represent the behavior of a material that inhibits moisture transport at higher concentration levels.

In Figure 6.6, bilinear curves for $R < 1$ lie below the line $\rho_{\text{sub}} = 0.5$, and by symmetry each exhibits a distinct minimum value that lies on the line $\rho_{\text{sub}} = \rho_c$ and decreases as $R \to 0$. Hence, for any given diffusivity ratio, there is a choice of critical concentration that minimizes the long-time saturation of the substrate below the value dictated by the cycle time ratio. This is in sharp contrast to materials for which $R > 1$, where the cycle time values represent the "best" case for wetting, and any other critical concentration results in greater substrate wetting over time. Of course, any cycle time ratio that increases the relative dry time will also reduce the overall substrate wetting, even for $R < 1$ materials.

We see the same effect in the linear $R < 1$ case in Figure 6.8. There, the model provides no critical concentration to vary, and the mechanics of diffusion are set solely by the slope of $D(\rho)$. Any choice of $R < 1$ results in eventual substrate saturation lower than otherwise dictated by the cycle time ratio, and is further affected by the relative wet and dry times of that cycle structure.

These results have implications for possible research into optimal single-layer materials for inhibiting corrosion. A metamaterial designed to slow diffusive processes with concentration leads to a far lower long-time substrate saturation than would otherwise be possible for an idealized material that allowed constant, and even extremely low, diffusivity.

6.5. Summary and conclusions

A discrete lattice Boltzmann method was used to model a finite coating test system consisting of an infinite moisture reservoir, a finite idealized barrier coating, and an impermeable substrate. The reservoir may be set to any concentration at any time. This models both natural environmental exposure and the common scenario when a coating is prepared on a test panel and placed into an environmental chamber for cyclic testing, where it is exposed to different moisture levels for long periods of time in order to determine its robustness for later use in service. An analytical solution for the concentration over time was presented, allowing for arbitrary cycling under the assumption of constant diffusivity. The numerical simulations matched the analytical solution with excellent accuracy.

We used the lattice Boltzmann simulations to determine the effects of moisture cycling at different cycle time ratios on the oscillatory concentration ρ at the substrate after long times. Since the onset of corrosion of a panel system is commonly linked to exposure of the substrate to moisture, it is important to understand how ρ evolves and stabilizes under different exposure regimes.

In the case where diffusivity is constant with concentration (as in the idealized Fickian case often used for barrier coatings), the steady-state behavior scales as expected with the cycle time ratio due to simple time averaging. However, many types of polymeric materials swell in the presence of sufficient solvent, increasing the rate of diffusivity. We considered two simple forms for the concentration-dependent diffusivity $D(\rho)$: a step function, where the polymer network is collapsed until a critical concentration is reached and swollen thereafter, and a linear model, where the dry network has a nominal diffusivity that increases until it reaches a maximal level when the coating is fully saturated.

Under the step function model, all parameters in the model affect the long-time oscillatory concentration. Regardless of the step function parameters (critical concentration and diffusivity change after wetting), increasing the relative dry time in a cycle protocol leads to a lower steady-state substrate concentration. As the critical concentration varies from very low (where the coating is almost always in the wet state) to very high (where it is almost always in the dry state), the long-time value increases linearly, reaches a peak whose location is fixed by the wet diffusivity, and thereafter decreases linearly.

Using the linear model, the behavior is similar, but much different in extent. As in the step function model, the cycle timing ratio has an effect on the overall behavior, but it is minimal compared to the overall saturation.

In either model, the results indicate that there is a second very different, but symmetric, regime that inverts the wet and dry diffusivity values. For traditional materials that permit faster transport under saturation, the choice of material properties can minimize substrate wetting to a value that will be greater than the constant diffusivity case for any cycle protocol. However, a metamaterial structurally designed to inhibit transport under saturation would permit an optimization of properties allowing for substrate wetting far lower than under constant diffusivity, even under cycle protocols with high relative wet periods.

These results imply that moisture cycling can play a large role in understanding the timescales and concentrations that may lead to corrosion, especially when considering the types of environmental tests that are regularly performed on candidate coating systems. Whether or not a particular type of polymeric system is subject to swelling, as in the case of a good urethane barrier topcoat versus an epoxy primer, plays a much larger role in the long-time behavior, and the parameters and form of the swelling lead to large variations. Since electrochemical means of determining diffusion and uptake behavior, such as impedance spectroscopy, rely on constant electrolyte exposure so that a useful equivalent circuit is applicable, controllable simulations such as these offer unique insight into variations caused

by moisture cycling, and offer a path toward the design of better coating systems and test protocols.

7. MULTI-LAYER LATTICE BOLTZMANN DIFFUSION

7.1. Introduction

In the previous chapters, the diffusion of water through a single coating layer was investigated in detail. We considered the effect of diffusion rate on substrate wetting during constant exposure using efficient lattice Boltzmann numerical simulations. Additionally, we considered the implementation of concentration-dependent diffusion, modeling two different simplified models of polymer swelling under the influence of moisture.

Earlier work on the modeling of moisture through multiple coating layers is limited [120], focusing primarily on mathematically simpler single layers [109]. Some experimental work has been done using electrochemical methods on bilayer coated panels [108, 107]. Corresponding numerical models typically solve the Fickian diffusion equation with appropriate boundary conditions, and assume an idealized interface between coating layers [32]. It has recently been shown that this simplification may not correctly predict wetting behavior at longer times due to the complexity of moisture pathways between layers, but no satisfactory corrections to the assumption have been studied [120]. Some experimental research indicates that layer interface effects are important [121]. Such analyses notably do not model concentration-dependent diffusion that may have effects on this phenomenon [122], but this is not specifically examined here.

We extend our single-layer lattice Boltzmann models to examine multiple layers that adjoin each other. We allow for the layers to have different diffusion coefficients and, through a modification to the imposed chemical potential, different saturation. As in earlier work, we assume instantaneous equilibration across the idealized interface, as well as uniform and homogeneous layers. We provide a brief outline of methods used for such modeling, and

provide a selection of examples. We comment on areas of future research, including the integration of more complex potential forms and swelling behavior.

7.2. Theory

We consider a modification to the equation of motion modeled using our lattice Boltzmann technique, writing

$$\partial_t \rho = \nabla M \nabla \mu \tag{7.1}$$

for mobility $M \equiv \frac{D\rho}{\theta}$ and potential $\mu \equiv \theta \ln \rho$. This equation of motion implies that the potential μ is spatially continuous. Here D is the diffusion coefficient, ρ is the moisture concentration, and θ is a unitless parameter that we will use to control relative saturation between layers.

As before, we consider a one-dimensional finite system bounded at one end by a moisture reservoir, and at the other end by a reflective substrate. In this chapter, we will allow the interior of the system to contain either a single layer or multiple layers of idealized coating through which moisture diffuses according to Fickian diffusion.

In the simplified case of a single coating layer, saturation is achieved by our simplification of the effective chemical potential μ, since during moisture exposure the coating fills with water to a maximal level defined by coating material properties. Despite the logarithmic ideal gas potential given above, we approximate the potential by a linear function, and account for saturation by imposing an arbitrarily large slope above a set concentration:

$$\mu = \mu(\rho) \equiv \begin{cases} \rho\theta & (\rho \leq 1) \\ \infty & (\rho > 1) \end{cases} \tag{7.2}$$

This is necessary to properly model saturation differences between layers, discussed below.

Because our system of interest consists of a reservoir with a fixed maximum concentration, the reservoir boundary condition can be considered a potential boundary condition,

with an equivalent density boundary condition $\rho(x = 0) = 1$. This has the effect of forcing a saturation of the coating at $\rho = 1$, the reservoir concentration.

Recall from our earlier work that our derivation of the lattice Boltzmann diffusion equation resulted in a diffusion coefficient $D = (\tau - \frac{1}{2})\theta$, where $\tau > \frac{1}{2}$ is a timescale parameter. The potential form given above means that the choice of θ is therefore somewhat arbitrary in a single layer, as we showed previously a range of θ values that provide excellent numerical stability. In this case, the diffusion coefficient D is effectively controlled solely by the choice of τ.

In the more general case of multiple layers, the interfaces between the layers require more careful treatment. We may be interested in variations of the diffusion rate between the layers. In typical usage, a barrier coating system consists of a topcoat that permits low ingress of moisture, with an underlying primer that provides good substrate adhesion but may have a diffusion coefficient orders of magnitude higher than the topcoat. Such a scenario may be easily modeled by choosing a fixed θ between layers and varying the timescale τ at the interface (say, $x = x'$) to achieve the desired diffusion coefficient, D, for each layer:

$$\tau = \tau(x) \equiv \begin{cases} \tau_1 & (x < x') \\ \tau_2 & (x \geq x') \end{cases} \tag{7.3}$$

To model the effect of saturation differences between the layers, the chemical potential form is similarly established piecewise by first varying θ between the layers:

$$\theta = \theta(x) \equiv \begin{cases} \theta_1 & (x < x') \\ \theta_2 & (x \geq x') \end{cases} \tag{7.4}$$

This yields a piecewise potential

$$\mu = \mu(\rho, x) \equiv \begin{cases} \rho\theta_1 & (x < x') \\ \rho\theta_2 & (x \geq x') \end{cases} \tag{7.5}$$

Since μ is spatially continuous, it must be constant across the layer interface. The result of this formation is a discontinuity in concentration across the interface determined by the ratio of θ values in the adjoining layers:

$$\rho(x = x'^{+}, t) = \frac{\theta_1}{\theta_2}\rho(x = x'^{-}, t) \tag{7.6}$$

Here we slightly abuse notation and let x'^{+} and x'^{-} be the values of x approaching the layer interface from the right and left, respectively. This is a statement of Henry's law, which relates concentration to partial pressures of gases. It has been applied in other multilayer mathematical and numerical work on water-polymer interactions, and is used here [32, 109]. At long constant exposure times ($t \to \infty$), each layer in a multi-layer system becomes saturated according to the θ ratio of its adjoining layers.

7.3. Lattice Boltzmann model

Our redefinition of the equation of motion, while equivalent to our earlier work on single-layer Fickian diffusion, requires a modification in the lattice Boltzmann numerical algorithms. The distribution equation

$$f_i(x + v_i, t + 1) = f_i(x, t) + \frac{1}{\tau}\left[f_i^0(\rho(x, t)) - f_i(x, t)\right] \tag{7.7}$$

introduced in the previous chapters has the equilibrium distributions $\{f_i^0\}$ modified and expressed in terms of the potential:

$$f_{-1}^0 = \frac{\mu(\rho)}{2} \tag{7.8}$$

$$f_0^0 = \rho - \mu(\rho) \tag{7.9}$$

$$f_1^0 = \frac{\mu(\rho)}{2} \tag{7.10}$$

This construction can also accommodate more general potential forms than the linear simplification we use. Indeed, choosing the linear potential $\mu(\rho) = \rho\theta$ recovers the equilibrium

distributions from the previous chapters. Within each layer, we set τ and θ spatially in simulations before each lattice site undergoes the collision step that modifies the local distributions toward the equilibrium values.

We note that this lattice Boltzmann construction, like that of the previous chapters, models diffusion with no advection effects. It is possible to model advection-diffusion, and even the full Navier-Stokes equation, by modifying the moments of the equilibrium distribution (introduced in an earlier chapter) to include imposed velocity terms. The derivations from such constructions are technical and can be found elsewhere [123]. Our construction effectively sets any such imposed velocities to zero to exclude advection.

7.4. Simulations

The appearance of both parameters τ and θ in the computation of the diffusion coefficient $D = (\tau - \frac{1}{2})\theta$ implies an interplay between these parameters for each coating layer under consideration. Since τ sets the diffusion timescale, varying it alone will affect the diffusion rate through a corresponding variation of D. To illustrate the effect of a τ variation between layers, we consider an example three-layer system similar to those in industrial and laboratory test environments. We consider the outermost and innermost layer (relative to the substrate) to be a barrier coating with low diffusion coefficient $D = 10^{-16}$ m^2/s, while the layer in the middle is a coating with higher diffusion coefficient $D = 10^{-15}$ m^2/s. Each layer has thickness 50 μm.

Such coatings might model, for example, certain urethane barrier topcoats and epoxy primers that are common in industrial applications, though the diffusion coefficient values may vary widely among different materials. We do not assume any particular material types or chemistry here. For this initial example, all layers are assumed to saturate equally. This somewhat arbitrary constraint ensures that θ is kept constant among all layers while the timescale τ is varied, as shown in Table 7.1.

Table 7.1. Simulation parameters τ and θ used for each layer, with diffusion coefficient in simulation units (D_{sim}) and scaled to laboratory units (D_{lab})

Layer	τ	θ	D_{sim}	$D_{\text{lab}}(\text{m}^2/\text{s})$
Outer	0.6	0.5	0.05	10^{-16}
Middle	1.5	0.5	0.5	10^{-15}
Inner	0.6	0.5	0.05	10^{-16}

In this table, D_{sim} is the diffusion coefficient in simulation units, while D_{lab} is the corresponding diffusion coefficient in laboratory units. This value is obtained through the scaling argument used in the previous chapters.

As an example, the lattice simulation is run for the laboratory equivalent of 376 days. The fractional spatial concentration profile (relative to saturation) is shown in Figure 7.1. As expected from the interface boundary condition, the profile is continuous but has a slope discontinuity corresponding to the different diffusion rates.

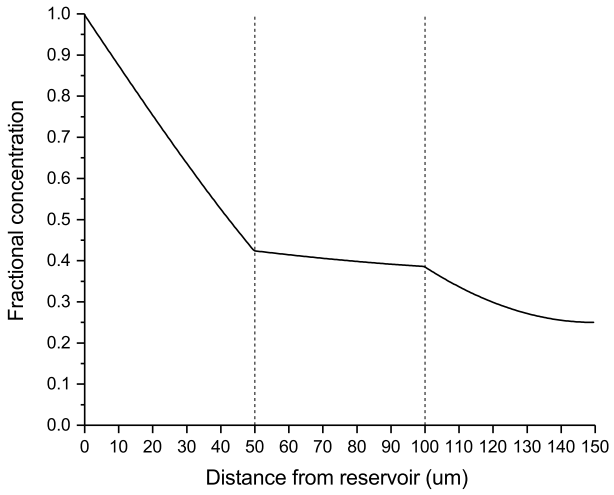

Figure 7.1. Spatial concentration profile for simulated three-layer coating system with low-diffusivity outer and inner layers (leftmost and rightmost regions) and higher-diffusivity middle layer (center region) after 376 days of moisture exposure

.

The physical representation of a θ variation between layers is more subtle, since the parameter affects both saturation and the value of the diffusion coefficient D. To examine differences in saturation using the Henry's law approach, we consider a three-layer system as before. The innermost and outermost layers have the same θ and τ (and therefore diffusion coefficient) as before. However, we choose several different θ values for the middle layer in order to change its saturation relative to the neighboring layers. Because this also changes the diffusion coefficient, we adjust the value of τ such that $D = 10^{-15}$ m/s^2 in laboratory units regardless of the relative saturation. Table 7.2 shows the different parameters used for the middle layer.

Table 7.2. Parameter choices for τ and θ used in middle layer for different saturation ratios (inner : middle), with corresponding diffusion constant in lattice units (D_{sim}) and in laboratory units (D_{lab})

Ratio	θ	τ	D_{sim}	D_{lab}
1 : 1	0.5	1.5	0.5	10^{-15} m^2/s
1 : 2	0.25	2.5	0.5	10^{-15} m^2/s
1 : 3	0.167	3.49	0.5	10^{-15} m^2/s
1 : 4	0.125	4.5	0.5	10^{-15} m^2/s

Qualitatively, decreasing θ should produce a filling effect that delays the transport of moisture by a saturation effect. To confirm this, we run a simulation for each of the listed saturation ratios for the same laboratory time of 376 days. Figure 7.2 shows the spatial concentration profile of these simulations.

The results confirm that increasing a layer's saturation, even at the same diffusion rate, delays the passage of moisture to neighboring layers through a "fill-up" effect. For the choices of parameters used here, setting the middle layer's saturation to twice that of its neighboring layers decreased the final substrate concentration by 26%, for example.

To better understand the effects of the saturation fill-up on the substrate, a simulation for each of the layer saturation ratios is run until the entire three-layer system reaches equilibrium. The substrate moisture concentration is tracked and plotted for the entire

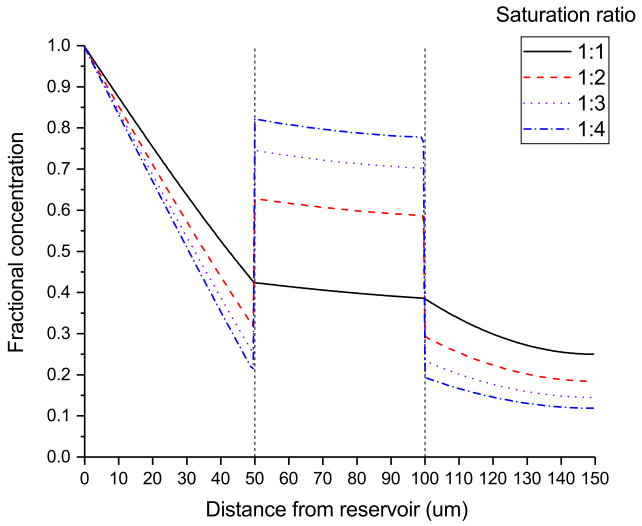

Figure 7.2. Spatial concentration profile for simulated three-layer coating system for varying layer saturation ratios, each run for 376 days of moisture exposure

.

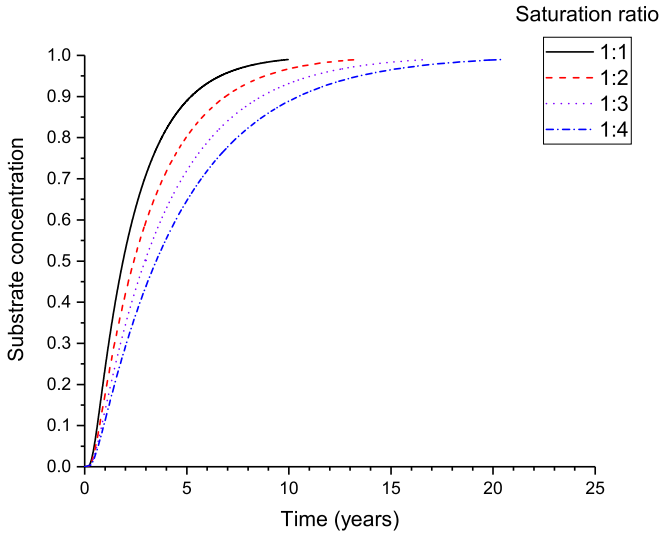

Figure 7.3. Substrate concentration over time for simulated three-layer coating system for varying layer saturation ratios, each run to equilibrium

.

time period in Figure 7.3. Higher middle-layer saturation produces a delay in moisture reaching the substrate that corresponds to the filling effect observed in Figure 7.2. Since the concentration gradients become very small as the system nears full saturation, there is an appreciable difference between the equilibrium times.

7.5. Conclusions

We have demonstrated that the diffusive lattice Boltzmann numerical method previously used to study single-layer coatings undergoing both constant and cycled moisture exposure can be extended to an arbitrary number of layers undergoing Fickian diffusion. Within each layer, the rate of diffusion and layer saturation can be controlled independently, matching the Henry's law behavior other authors have used to account for saturation differences in different material types. For example, many protective coating systems consist of a low-saturation outer barrier layer with low diffusion coefficient, and a higher-saturation base or primer layer with high diffusion coefficient. More complex systems, like in automotive or aerospace applications, may have additional intermediate layers.

We introduced a simple three-layer system consisting of an outer and inner layer with low diffusion rate and saturation, a rough approximation to common barrier urethanes. The middle layer has a higher diffusion rate and saturation, which could model materials like epoxies. This system was chosen in order to better examine how the middle layer fills and acts as a source that feeds the inner layer. A Henry's law interface saturation discontinuity results in qualitatively expected behavior, in that the middle layer feeds the inner layer, but with a delay; an increase in the layer's saturation means it exhibits a "filling-up" effect that delays the passage of moisture to its neighboring layer.

Unlike other finite-element simulations and those using differential equation solvers, this lattice method exhibits no interface instabilities, even in the presence of high gradients. Further, it is possible to introduce concentration-dependent diffusion rates using this method, which we investigated in detail for single-layer systems. However, we leave such analysis for future work. With this numerical approach, it is possible to input exposure parameters like diffusion coefficient, layer saturation, coating thickness, and exposure time and model quantities like moisture uptake and concentration spatial profiles, providing useful data on moisture transport and the effects of different exposure regimes over time.

8. FUTURE WORK

In this brief chapter, we outline areas of interest for future work and research.

8.1. Molecular dynamics

As discussed, molecular dynamics has been used to successfully model a variety of behaviors in representative models of physical systems. Originally used to examine Lennard-Jones fluids, it has seen wide interest in glass-forming thermoplastic chain models of simple coarse-grained polymeric systems. Only recently, however, have molecular dynamics simulations been applied to models of densely-crosslinked thermosets.

Recent work by collaborators has investigated the heterogeneity present in model crosslinked networks, since mathematical approaches using broader statistics originally assumed generally homogeneous bonding [22]. Since not every chemical precursor will be optimally placed for bonding at all crosslinking sites, imperfections will exist even well into the gel state during a thorough crosslinking process [1, 30]. The types and relative occurrence of small fragments, loops, cycles, and dangling ends in a thermoset network have been examined for the select representative 3- and 6-functional systems considered here, and these results are assumed to represent the extrema of networks whose functionality distribution lies between them.

A complete analysis of the structure of networks undergoing degradation remains open. In this work, we examined the distribution of network fragments in model thin films during stochastic degradation, as well as the effect of bond scission on network percolation that is linked to the gel point. However, it has not been demonstrated whether the statistics of more complex imperfections in network structure during the crosslinking process should be mirrored during degradation. While the crosslinking process is influenced by the types of network precursors and spatial distribution needed for bond formation, bond scission is treated as a random process that is not simply the reversal of crosslinking. A full treatment

of network heterogeneity during stochastic bond scission can provide a more complete picture of network behavior in service as a polymeric system ages.

We previously showed that network imperfections couple with spatial constraints of rapid cooling to produce bulk void structures as a sudden occurrence [23]. This implies that an apparently well-formed crosslinked network at high conversion may eventually form percolating paths through a film structure to permit the ingress of moisture and other aggressive species. The requirements for such a path over a broad coating system are not well understood, nor is the precise dependence on conversion or more complex imperfections that may result from non-ideal formation or application. Future work may extend our cavitation analysis to a more comprehensive set of simulations that examine percolating path formation, both as a result of incomplete conversion and the types of degradation we examined in model films.

8.2. Finite-element analysis

The cohesive zone model (CZM) is a numerical approach to computing the onset and growth of material fractures [124, 125]. Earlier linear elastic crack growth models assumed the existence of a crack or flaw in a material, and that the nonlinear plastic region ahead of the crack was negligible. While this approach is useful when modeling brittle materials where the location and magnitude of an existing crack is known *a priori*, it breaks down when applied to more pliant materials or any time a preexisting crack is not assumed. The approach has been used to successfully model crack formation and propagation in materials as varied as concrete and poly(methyl methacrylate).

For normal separation, debonding is established using a bilinear normal traction function as in Figure 8.1. Here Γ_0 is the debond energy, σ_u the maximum normal stress at the start of debonding, and δ_r is the gap separation when debonding is complete.

Many experimental adhesion tests commonly used to characterize materials are known to be problematic in accurately measuring the critical strain energy release rate. In one such method, the peel test, work done in the test is often dissipative as the material undergoes

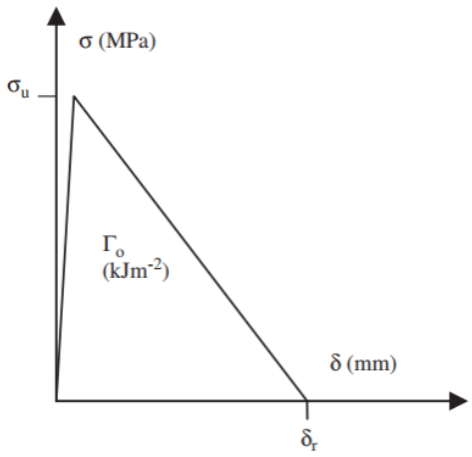

Figure 8.1. Bilinear CZM traction separation curve, with debonding energy Γ_0, maximum stress at start of debonding σ_u, and contact gap after debonding δ_r

plastic yielding [126]. Another method, the lap shear test, assumes materials undergo small strains and precludes nonlinear behavior [127].

Recently, a novel adhesive test method has been developed to more accurately measure debonding energies [128]. This method requires only a tensile testing apparatus. To apply it, a substrate-film bilayer is formed with a small portion of the film debonded during construction. The bilayer is subjected to a pressure P; as a result, the bonded portion of the bilayer stretches a fraction λ'' of its original length, and the debonded portion stretches a fraction λ'. The elastic energy stored in the bonded bilayer divided by its undeformed area is computed as

$$U_b(\lambda'') = \int_1^{\lambda''} P_b(\lambda)\, d\lambda \tag{8.1}$$

where $P_b(\lambda)$ is the force-stretch curve of the bilayer, measured before the experiment. We define the same quantity for the substrate alone, $U_s(\lambda')$, analogously. The useful result is that of the strain energy release rate, given to be $G \equiv U_b(\lambda'') - U_s(\lambda') + P(\lambda' - \lambda'')$. When the pressure P is sufficient for the advancement of debonding, the energy release rate G reaches the value of the debonding energy Γ_0.

Future work may use such methods to determine material parameters needed to implement accurate CZM modeling of joint types discussed previously. Additionally, the

extension of our models to complete three-dimensional systems will permit a more thorough and careful analysis of possible edge effects that are necessarily ignored in two-dimensional models.

8.3. Lattice Boltzmann modeling

We developed a one-dimensional lattice Boltzmann model of moisture diffusion through a coating system. The technique remained stable through a wide parameter range that accommodates the large gradients present during cycled exposure in the presence of a reservoir. The model included adjustments for material parameters like diffusion rates, swelling behaviors, and maximal saturation. A natural extension of this work is to permit the use of two- and three-dimensional systems. Our one-dimensional system necessarily excludes edge effects and assumes a uniform distribution of moisture at the coating surface. This assumption is reasonable for the case of a coated panel immersed into a bath of water. However, in testing and the environment, sprays and dew formation are more likely to produce a distribution of localized droplets on the coated surface, leading to evaporation and diffusion more complex than can be included in our existing model. Lattice Boltzmann numerical techniques have previously been employed to successfully examine droplet behavior under evaporation [129] in two dimensions. An extension of our diffusive work to a full three-dimensional model would permit the study of similar droplet behavior, but with the addition of inward diffusion as well as evaporation. Pressure distribution may be explicitly considered in such a model as a function of droplet shape over time. Comparison to the idealized reservoir case that we examined could determine whether a given application or study requires the complexity of droplet modeling at all.

For single-layer coatings, we examined two forms of concentration-dependent diffusion coefficient $D(\rho)$ and showed that substrate concentration depends heavily on the interplay between the form of $D(\rho)$ and the time parameters used in moisture cycling. The numerical method was then extended two multi-layer coating systems, but assuming constant diffusion coefficient within each layer. Future work could include non-constant $D(\rho)$ in the multi-layer

model. This would permit a more complete numerical characterization of each layer under consideration for a particular material stack.

Finally, new advances in lattice Boltzmann theory provide intriguing applications to, for example, coarse-grained molecular dynamics [130]. Investigations into possible applications of efficient lattice Boltzmann setups to other types of polymeric systems, traditionally modeled with much more complex molecular dynamics simulations, would be useful. Such studies provide useful connections between the different numerical techniques employed in our broader work.

REFERENCES

[1] D.M. Kroll and S.G. Croll. Heterogeneity in polymer networks formed by a single copolymerization reaction: I. Gelation and pre-gel structure. *Polymer*, 115:154 – 163, 2017.

[2] Paul J Flory. Network structure and the elastic properties of vulcanized rubber. *Chemical reviews*, 35(1):51–75, 1944.

[3] Walter H. Stockmayer. Theory of molecular size distribution and gel formation in branched-chain polymers. *The Journal of Chemical Physics*, 11(2):45–55, 1943.

[4] Loup Verlet. Computer "experiments" on classical fluids. I. thermodynamical properties of Lennard-Jones molecules. *Phys. Rev.*, 159:98–103, Jul 1967.

[5] J Dana Honeycutt and Hans C Andersen. Molecular dynamics study of melting and freezing of small Lennard-Jones clusters. *Journal of Physical Chemistry*, 91(19):4950–4963, 1987.

[6] Marvin Bishop, M. H. Kalos, and H. L. Frisch. Molecular dynamics of polymeric systems. *The Journal of Chemical Physics*, 70(3):1299–1304, 1979.

[7] Gary S. Grest and Kurt Kremer. Molecular dynamics simulation for polymers in the presence of a heat bath. *Phys. Rev. A*, 33:3628–3631, May 1986.

[8] Brian Hinderliter and Stuart Croll. Monte Carlo approach to estimating the photodegradation of polymer coatings. *Journal of Coatings Technology and Research*, 2(6):483–491, 2005.

[9] S.G. Croll, B.R. Hinderliter, and S. Liu. Statistical approaches for predicting weathering degradation and service life. *Progress in Organic Coatings*, 55(2):75 – 87, 2006. Coatings Science International Conference Program.

[10] L.D.R. Grant, R.D. Adams, and Lucas F.M. da Silva. Experimental and numerical analysis of single-lap joints for the automotive industry. *International Journal of Adhesion and Adhesives*, 29(4):405 – 413, 2009.

[11] Min You, Zhan-Mou Yan, Xiao-Ling Zheng, Hai-Zhou Yu, and Zhi Li. A numerical and experimental study of gap length on adhesively bonded aluminum double-lap joint. *International Journal of Adhesion and Adhesives*, 27(8):696 – 702, 2007.

[12] Dieter Kockott. Natural and artificial weathering of polymers. *Polymer Degradation and Stability*, 25(2):181 – 208, 1989.

[13] U. Schulz, P. Trubiroha, U. Schernau, and H. Baumgart. The effects of acid rain on the appearance of automotive paint systems studied outdoors and in a new artificial weathering test. *Progress in Organic Coatings*, 40(1–4):151 – 165, 2000.

[14] F. Deflorian, S. Rossi, and M. Fedel. Organic coatings degradation: Comparison between natural and artificial weathering. *Corrosion Science*, 50(8):2360 – 2366, 2008.

[15] K.M. Wernståhl. Service life prediction of automotive coatings, correlating infrared measurements and gloss retention. *Polymer Degradation and Stability*, 54(1):57 – 65, 1996.

[16] F. Deflorian, S. Rossi, L. Fedrizzi, and C. Zanella. Comparison of organic coating accelerated tests and natural weathering considering meteorological data. *Progress in Organic Coatings*, 59(3):244 – 250, 2007.

[17] F. Deflorian, L. Fedrizzi, and S. Rossi. Electrochemical impedance spectroscopy and fourier transform infrared spectroscopy of natural and accelerated weathering of organic coatings. *CORROSION*, 54(8):598–605, 1998.

[18] B.R. Hinderliter, S.G. Croll, D.E. Tallman, Q. Su, and G.P. Bierwagen. Interpretation of {EIS} data from accelerated exposure of coated metals based on modeling of coating physical properties. *Electrochimica Acta*, 51(21):4505 – 4515, 2006.

[19] Mark Nichols, John Boisseau, Lynn Pattison, Don Campbell, Jeff Quill, Jacob Zhang, Don Smith, Karen Henderson, Jill Seebergh, Douglas Berry, Tony Misovski, and Cindy Peters. An improved accelerated weathering protocol to anticipate Florida exposure behavior of coatings. *Journal of Coatings Technology and Research*, 10(2):153–173, 2013.

[20] Mark E. Nichols. Anticipating paint cracking: The application of fracture mechanics to the study of paint weathering. *Journal of Coatings Technology*, 74(924):39–46, 2002.

[21] S.R. Taylor, F. Contu, R. Santhanam, and P. Suwanna. The use of cationic fluoroprobes to characterize ionic pathways in organic coatings. *Progress in Organic Coatings*, 73(2–3):169 – 172, 2012.

[22] D.M. Kroll and S.G. Croll. Influence of crosslinking functionality, temperature and conversion on heterogeneities in polymer networks. *Polymer*, 79:82 – 90, 2015.

[23] Malia Zee, Aaron J. Feickert, D.M. Kroll, and S.G. Croll. Cavitation in crosslinked polymers: Molecular dynamics simulations of network formation. *Progress in Organic Coatings*, 83:55 – 63, 2015.

[24] Jonathan W. Martin. *Repeatability and Reproducibility of Field Exposure Results*, chapter 1, pages 2–22. American Chemical Society, 2001.

[25] Henry K. Hardcastle and William L. Meeks. Considerations for characterizing moisture effects in coatings weathering studies. *Journal of Coatings Technology and Research*, 5(2):181–192, 2008.

[26] Viktor Baukh, Hendrik P. Huinink, Olaf C.G. Adan, and Leendert G.J. van der Ven. Natural versus accelerated weathering: Understanding water kinetics in bilayer coatings. *Progress in Organic Coatings*, 76(9):1197 – 1202, 2013.

[27] Xiaodong Shi, Brian R. Hinderliter, and Stuart G. Croll. Environmental and time dependence of moisture transportation in an epoxy coating and its significance for accelerated weathering. *Journal of Coatings Technology and Research*, 7(4):419–430, 2010.

[28] Takuya Kamisho, Yukitoshi Takeshita, Seizo Sakata, and Takashi Sawada. Water absorption of water-based anticorrosive coatings and its effect on mechanical property and adhesive performance. *Journal of Coatings Technology and Research*, 11(2):199–205, 2014.

[29] Minas M. Mezedur, Massoud Kaviany, and Wayne Moore. Effect of pore structure, randomness and size on effective mass diffusivity. *AIChE Journal*, 48(1):15–24, 2002.

[30] D.M. Kroll and S.G. Croll. Heterogeneity in polymer networks formed by a single copolymerization reaction: II. Post-gelation structure and pendants. *Polymer*, 116:113 – 123, 2017.

[31] John Crank. *The Mathematics of Diffusion*. Oxford University Press, 1979.

[32] L De Rosa, T Monetta, DB Mitton, and F Bellucci. Monitoring degradation of single and multilayer organic coatings I. absorption and transport of water: Theoretical analysis and methods. *Journal of the Electrochemical Society*, 145(11):3830–3838, 1998.

[33] Muhammad Sahimi and Dietrich Stauffer. Efficient simulation of flow and transport in porous media. *Chemical Engineering Science*, 46(9):2225 – 2233, 1991.

[34] Deqiang Mu, Zhong-Sheng Liu, Cheng Huang, and Ned Djilali. Prediction of the effective diffusion coefficient in random porous media using the finite element method. *Journal of Porous Materials*, 14(1):49–54, 2007.

[35] Aman Pathania, Raj Kumar Arya, and Sanjeev Ahuja. Crosslinked polymeric coatings: Preparation, characterization, and diffusion studies. *Progress in Organic Coatings*, 105:149 – 162, 2017.

[36] Viktor Baukh, Hendrik P. Huinink, Olaf C.G. Adan, Sebastiaan J.F. Erich, and Leendert G.J. van der Ven. Predicting water transport in multilayer coatings. *Polymer*, 53(15):3304 – 3312, 2012.

[37] G.K. van der Wel and O.C.G. Adan. Moisture in organic coatings — a review. *Progress in Organic Coatings*, 37(1–2):1 – 14, 1999.

[38] Brian R. Hinderliter, Kerry N. Allahar, Gordon P. Bierwagen, Dennis E. Tallman, and Stuart G. Croll. Water sorption and diffusional properties of a cured epoxy resin measured using alternating ionic liquids/aqueous electrolytes in electrochemical impedance spectroscopy. *Journal of Coatings Technology and Research*, 5(4):431–438, 2008.

[39] Joannie W. Chin, Tinh Nguyen, and Khaled Aouadi. Sorption and diffusion of water, salt water, and concrete pore solution in composite matrices. *Journal of Applied Polymer Science*, 71(3):483–492, 1999.

[40] Dan Y Perera. Effect of pigmentation on organic coating characteristics. *Progress in Organic Coatings*, 50(4):247 – 262, 2004.

[41] M. Gordon. Good's theory of cascade processes applied to the statistics of polymer distributions. *Proceedings of the Royal Society of London A: Mathematical, Physical and Engineering Sciences*, 268(1333):240–256, 1962.

[42] K. Dušek and M. Dušková-Smrčková. Network structure formation during crosslinking of organic coating systems. *Progress in Polymer Science*, 25(9):1215 – 1260, 2000.

[43] Douglas R. Miller and Christopher W. Macosko. A new derivation of post gel properties of network polymers. *Macromolecules*, 9(2):206–211, 1976.

[44] Søren Kiil. Quantification of simultaneous solvent evaporation and chemical curing in thermoset coatings. *Journal of Coatings Technology and Research*, 7(5):569–586, 2010.

[45] Srikanth Sastry, Pablo G. Debenedetti, and Frank H. Stillinger. Statistical geometry of particle packings. II. "Weak spots" in liquids. *Phys. Rev. E*, 56:5533–5543, Nov 1997.

[46] V. G. Baidakov and K. S. Bobrov. Spontaneous cavitation in a Lennard-Jones liquid at negative pressures. *The Journal of Chemical Physics*, 140(18):184506, 2014.

[47] Y. Cai, H. A. Wu, and S. N. Luo. Cavitation in a metallic liquid: Homogeneous nucleation and growth of nanovoids. *The Journal of Chemical Physics*, 140(21):214317, 2014.

[48] Mark J. Stevens. Interfacial fracture between highly cross-linked polymer networks and a solid surface: Effect of interfacial bond density. *Macromolecules*, 34(8):2710–2718, 2001.

[49] Mesfin Tsige and Mark J. Stevens. Effect of cross-linker functionality on the adhesion of highly cross-linked polymer networks: A molecular dynamics study of epoxies. *Macromolecules*, 37(2):630–637, 2004.

[50] Mesfin Tsige, Christian D. Lorenz, and Mark J. Stevens. Role of network connectivity on the mechanical properties of highly cross-linked polymers. *Macromolecules*, 37(22):8466–8472, 2004.

[51] K. Kremer and G. Grest. Monte Carlo and molecular dynamics simulations in polymer science. chapter 4, pages 194–271. Oxford University Press, New York, 1995.

[52] Gary S. Grest and Kurt Kremer. Statistical properties of random cross-linked rubbers. *Macromolecules*, 23(23):4994–5000, 1990.

[53] Steve Plimpton. Fast parallel algorithms for short-range molecular dynamics. *Journal of Computational Physics*, 117(1):1 – 19, 1995.

[54] Mark J. Stevens. Manipulating connectivity to control fracture in network polymer adhesives. *Macromolecules*, 34(5):1411–1415, 2001.

[55] Raquel G. Duarte, Sergio González, Antonio S. Castela, Mário G.S. Ferreira, and Ricardo M. Souto. Sensing polymer inhomogeneity in coated metals during the early stages of coating degradation. *Progress in Organic Coatings*, 74(2):365 – 370, 2012.

[56] Jia-Sun Tsang and David Erhardt. Current research on the effects of solvents and gelled and aqueous cleaning systems on oil paint films. *Journal of the American Institute for Conservation*, 31(1):87–94, 1992.

[57] R Estevez and D Long. Probing and characterizing the early stages of cavitation in glassy polymers in molecular dynamics simulations. *Modelling and Simulation in Materials Science and Engineering*, 19(4), 2011.

[58] B. Sixou. Molecular dynamics simulation of the first stages of the cavitation process in amorphous polymers. *Molecular Simulation*, 33(12):965–973, 2007.

[59] Jörg Rottler and Mark O. Robbins. Yield conditions for deformation of amorphous polymer glasses. *Phys. Rev. E*, 64:051801, Oct 2001.

[60] A. R. C. Baljon and Mark O. Robbins. Simulations of crazing in polymer glasses: Effect of chain length and surface tension. *Macromolecules*, 34(12):4200–4209, 2001.

[61] Dhiraj K. Mahajan, Bhupinder Singh, and Sumit Basu. Void nucleation and disentanglement in glassy amorphous polymers. *Phys. Rev. E*, 82:011803, Jul 2010.

[62] V.P. Voloshin and Yu.I. Naberukhin. Homogeneity loss phase transition in packings of Lennard-Jones atoms under density decreasing. *Journal of Molecular Liquids*, 82(1):19 – 26, 1999.

[63] D. S. Corti, P. G. Debenedetti, S. Sastry, and F. H. Stillinger. Constraints, metastability, and inherent structures in liquids. *Phys. Rev. E*, 55:5522–5534, May 1997.

[64] A. Yu. Kuksin, G. E. Norman, and V. V. Stegailov. The phase diagram and spinodal decomposition of metastable states of Lennard-Jones system. *High Temperature*, 45(1):37–48, 2007.

[65] Srikanth Sastry. Liquid limits: Glass transition and liquid-gas spinodal boundaries of metastable liquids. *Phys. Rev. Lett.*, 85:590–593, Jul 2000.

[66] V. G. Baidakov and S. P. Protsenko. Singular point of a system of Lennard-Jones particles at negative pressures. *Phys. Rev. Lett.*, 95:015701, Jun 2005.

[67] K. M. Flores, D. Suh, R. H. Dauskardt, P. Asoka-Kumar, P. A. Sterne, and R. H. Howell. Characterization of free volume in a bulk metallic glass using positron annihilation spectroscopy. *Journal of Materials Research*, 17(5):1153–1161, 2002.

[68] A Rozanski, A Galeski, and M Debowska. Initiation of cavitation of polypropylene during tensile drawing. *Macromolecules*, 44(1):20–28, 2010.

[69] G. Dlubek, K. Saarinen, and H. M. Fretwell. The temperature dependence of the local free volume in polyethylene and polytetrafluoroethylene: A positron lifetime study. *Journal of Polymer Science Part B: Polymer Physics*, 36(9):1513–1528, 1998.

[70] Pablo G. Debenedetti and Thomas M. Truskett. The statistical geometry of voids in liquids. *Fluid Phase Equilibria*, 158–160:549 – 556, 1999.

[71] A.E. Hughes, A. Trinchi, F.F. Chen, Y.S. Yang, I.S. Cole, S. Sellaiyan, J. Carr, P.D. Lee, G.E. Thompson, and T.Q. Xiao. The application of multiscale quasi 4D CT to the study of SrCrO4 distributions and the development of porous networks in epoxy-based primer coatings. *Progress in Organic Coatings*, 77(11):1946 – 1956, 2014.

[72] Giulio Biroli and Chiara Cammarota. Fluctuations and shape of cooperative rearranging regions in glass-forming liquids. *Phys. Rev. X*, 7:011011, Jan 2017.

[73] Raffaele Pastore, Massimo Pica Ciamarra, Giuseppe Pesce, and Antonio Sasso. Connecting short and long time dynamics in hard-sphere-like colloidal glasses. *Soft Matter*, 11(3):622–626, 2015.

[74] Christoph Bennemann, Claudio Donati, Jorg Baschnagel, and Sharon C. Glotzer. Growing range of correlated motion in a polymer melt on cooling towards the glass transition. *Nature*, 399:246–249, 1999.

[75] Mya Warren and Jörg Rottler. Atomistic mechanism of physical ageing in glassy materials. *EPL (Europhysics Letters)*, 88(5):58005, 2009.

[76] Raffaele Pastore, Giuseppe Pesce, Antonio Sasso, and Massimo Pica Ciamarra. Cage size and jump precursors in glass-forming liquids: experiment and simulations. *The Journal of Physical Chemistry Letters*, 8(7):1562–1568, 2017.

[77] K. Vollmayr-Lee. Single particle jumps in a binary Lennard-Jones system below the glass transition. *The Journal of Chemical Physics*, 121(10):4781–4794, 2004.

[78] C. Bennemann, J. Baschnagel, W. Paul, and K. Binder. Molecular-dynamics simulation of a glassy polymer melt: Rouse model and cage effect. *Computational and Theoretical Polymer Science*, 9(3):217 – 226, 1999.

[79] Massimo Pica Ciamarra, Raffaele Pastore, and Antonio Coniglio. Particle jumps in structural glasses. *Soft Matter*, 12(2):358–366, 2016.

[80] Raffaele Pastore, Antonio Coniglio, and Massimo Pica Ciamarra. From cage-jump motion to macroscopic diffusion in supercooled liquids. *Soft Matter*, 10:5724–5728, 2014.

[81] Mesfin Tsige and Mark J Stevens. Effect of cross-linker functionality on the adhesion of highly cross-linked polymer networks: a molecular dynamics study of epoxies. *Macromolecules*, 37(2):630–637, 2004.

[82] Mark J Stevens. Interfacial fracture between highly cross-linked polymer networks and a solid surface: effect of interfacial bond density. *Macromolecules*, 34(8):2710–2718, 2001.

[83] Mesfin Tsige, Christian D Lorenz, and Mark J Stevens. Role of network connectivity on the mechanical properties of highly cross-linked polymers. *Macromolecules*, 37(22):8466–8472, 2004.

[84] Malia Zee, Aaron J. Feickert, D.M. Kroll, and S.G. Croll. Cavitation in crosslinked polymers: Molecular dynamics simulations of network formation. *Progress in Organic Coatings*, 83:55 – 63, 2015.

[85] Edward H. Erath and Robert A. Spurr. Occurrence of globular formations in thermosetting resins. *Journal of Polymer Science*, 35(129):391–399, 1959.

[86] James L. Racich and James A. Koutsky. Nodular structure in epoxy resins. *Journal of Applied Polymer Science*, 20(8):2111–2129, 1976.

[87] Farid F. Abraham and Y. Singh. The structure of a hard-sphere fluid in contact with a soft repulsive wall. *The Journal of Chemical Physics*, 67(5):2384–2385, 1977.

[88] J. Helfferich, F. Ziebert, S. Frey, H. Meyer, J. Farago, A. Blumen, and J. Baschnagel. Continuous-time random-walk approach to supercooled liquids. i. different definitions of particle jumps and their consequences. *Phys. Rev. E*, 89:042603, Apr 2014.

[89] J. Helfferich, F. Ziebert, S. Frey, H. Meyer, J. Farago, A. Blumen, and J. Baschnagel. Continuous-time random-walk approach to supercooled liquids. II. Mean-square displacements in polymer melts. *Phys. Rev. E*, 89:042604, Apr 2014.

[90] C. Bennemann, J. Baschnagel, and W. Paul. Molecular-dynamics simulation of a glassy polymer melt: Incoherent scattering function. *The European Physical Journal B - Condensed Matter and Complex Systems*, 10(2):323–334, 1999.

[91] Katharina Vollmayr-Lee, Robin Bjorkquist, and Landon M. Chambers. Microscopic picture of aging in sio_2. *Phys. Rev. Lett.*, 110:017801, Jan 2013.

[92] Anton Smessaert and Jörg Rottler. Distribution of local relaxation events in an aging three-dimensional glass: Spatiotemporal correlation and dynamical heterogeneity. *Phys. Rev. E*, 88:022314, Aug 2013.

[93] Reinhard Diestel. *Graph Theory*, volume 173 of *Graduate Texts in Mathematics*. Springer-Verlag, 5th edition, 2016.

[94] Sirish K. Reddy, Kristi S. Anseth, and Christopher N. Bowman. Modeling of network degradation in mixed step-chain growth polymerizations. *Polymer*, 46(12):4212 – 4222, 2005.

[95] Aaron J. Feickert and S. G. Croll. Failure of coatings over joints and gaps: finite-element models. *Journal of Coatings Technology and Research*, Oct 2017.

[96] Xiaocong He. A review of finite element analysis of adhesively bonded joints. *International Journal of Adhesion and Adhesives*, 31(4):248 – 264, 2011.

[97] MGGV Elices, GV Guinea, J Gomez, and J Planas. The cohesive zone model: advantages, limitations and challenges. *Engineering Fracture Mechanics*, 69(2):137–163, 2002.

[98] Richard W Macek and Stewart A Silling. Peridynamics via finite element analysis. *Finite Elements in Analysis and Design*, 43(15):1169–1178, 2007.

[99] MD Banea and Lucas FM da Silva. Adhesively bonded joints in composite materials: an overview. *Proceedings of the Institution of Mechanical Engineers, Part L: Journal of Materials Design and Applications*, 223(1):1–18, 2009.

[100] T. Mertens, F.J. Gammel, M. Kolb, O. Rohr, L. Kotte, S. Tschöcke, S. Kaskel, and U. Krupp. Investigation of surface pre-treatments for the structural bonding of titanium. *International Journal of Adhesion and Adhesives*, 34:46 – 54, 2012.

[101] T. Mertens and H. Kollek. On the stability and composition of oxide layers on pretreated titanium. *International Journal of Adhesion and Adhesives*, 30(6):466 – 477, 2010.

[102] ASTM E8 / E8M-16a. Standard test methods for tension testing of metallic materials. Technical report, ASTM International, 2016.

[103] R Von Mises. Mechanics of solid bodies in the plastically-deformable state. *Nachr. Ges. Wiss. Goettingen, Math.-Phys. Kl*, 1:582–592, 1913.

[104] Magd Abdel Wahab. *The Mechanics of Adhesives in Composite and Metal Joints*. DEStech Publications, 2014.

[105] FAA. MMPDS-10: Metallic materials properties development and standardization. Technical report, Federal Aviation Administration, 2015.

[106] Kyle T. Strand, Aaron J. Feickert, and Alexander J. Wagner. Fourth-order analysis of a diffusive lattice Boltzmann method for barrier coatings. *Phys. Rev. E*, 95:063311, Jun 2017.

[107] P. Carbonini, T. Monetta, L. Nicodemo, P. Mastronardi, B. Scatteia, and F. Bellucci. Electrochemical characterisation of multilayer organic coatings. *Progress in Organic Coatings*, 29(1):13 – 20, 1996. Proceedings of the 21st International Conference in Organic Coatings Science and Technology.

[108] J.H Park, G.D Lee, H Ooshige, A Nishikata, and T Tsuru. Monitoring of water uptake in organic coatings under cyclic wet–dry condition. *Corrosion Science*, 45(8):1881 – 1894, 2003.

[109] Brian R. Hinderliter and Erik D. Sapper. Water concentration distribution in coatings during accelerated weathering protocols. *Journal of Coatings Technology and Research*, 12(3):477–487, May 2015.

[110] YH Qian, Dominique d'Humières, and Pierre Lallemand. Lattice BGK models for Navier-Stokes equation. *EPL (Europhysics Letters)*, 17(6):479, 1992.

[111] Michael R. Swift, W. R. Osborn, and J. M. Yeomans. Lattice Boltzmann simulation of nonideal fluids. *Phys. Rev. Lett.*, 75:830–833, Jul 1995.

[112] U. Frisch, B. Hasslacher, and Y. Pomeau. Lattice-gas automata for the Navier-Stokes equation. *Phys. Rev. Lett.*, 56:1505–1508, Apr 1986.

[113] Dieter Wolf-Gladrow. A lattice Boltzmann equation for diffusion. *Journal of Statistical Physics*, 79(5-6):1023–1032, 1995.

[114] Xiaowen Shan and Gary Doolen. Diffusion in a multicomponent lattice Boltzmann equation model. *Phys. Rev. E*, 54:3614–3620, Oct 1996.

[115] A.J. Wagner and S. May. Electrostatic interactions across a charged lipid bilayer. *Eur Biophys J*, 36:293–303, April 2007.

[116] Irina Ginzburg. Prediction of the moments in advection-diffusion lattice Boltzmann method. i. truncation dispersion, skewness, and kurtosis. *Phys. Rev. E*, 95:013304, Jan 2017.

[117] Alexander J. Wagner and Kyle Strand. Fluctuating lattice Boltzmann method for the diffusion equation. *Phys. Rev. E*, 94:033302, Sep 2016.

[118] A. J. Wagner. Thermodynamic consistency of liquid-gas lattice Boltzmann simulations. *Phys. Rev. E*, 74:056703, Nov 2006.

[119] Aaron J. Feickert and Alexander J. Wagner. Optimizing coating performance for diffusion under cyclic moisture exposure. *Phys. Rev. Materials*, 1:033804, Aug 2017.

[120] K. N. Allahar, B. R. Hinderliter, D. E. Tallman, and G. P. Bierwagen. Water transport in multilayer organic coatings. *Journal of The Electrochemical Society*, 155(8):F201–F208, 2008.

[121] A. Miszczyk and T. Schauer. Electrochemical approach to evaluate the interlayer adhesion of organic coatings. *Progress in Organic Coatings*, 52(4):298 – 305, 2005. AETOC 2003.

[122] N.L Thomas and A.H Windle. A theory of case II diffusion. *Polymer*, 23(4):529 – 542, 1982.

[123] Timm Krüger, Halim Kusumaatmaja, Alexandr Kuzmin, Orest Shardt, Goncalo Silva, and Erlend Magnus Viggen. *The Lattice Boltzmann Method: Principles and Practice*. Graduate Texts in Physics. Springer, 2017.

[124] M Elices, GV Guinea, J Gomez, and J Planas. The cohesive zone model: advantages, limitations and challenges. *Engineering Fracture Mechanics*, 69(2):137–163, 2002.

[125] Teng Zhang, Shaoting Lin, Hyunwoo Yuk, and Xuanhe Zhao. Predicting fracture energies and crack-tip fields of soft tough materials. *Extreme Mechanics Letters*, 4:1–8, 2015.

[126] A. N. Gent and G. R. Hamed. Peel mechanics of adhesive joints. *Polymer Engineering & Science*, 17(7):462–466, 1977.

[127] K Kendall. Crack propagation in lap shear joints. *Journal of Physics D: Applied Physics*, 8(5):512, 1975.

[128] Jingda Tang, Jianyu Li, Joost J Vlassak, and Zhigang Suo. Adhesion between highly stretchable materials. *Soft Matter*, 12(4):1093–1099, 2016.

[129] Joseph B. Miller, Austin C. P. Usselman, Rebecca J. Anthony, Uwe R. Kortshagen, Alexander J. Wagner, Alan R. Denton, and Erik K. Hobbie. Phase separation and the 'coffee-ring' effect in polymer-nanocrystal mixtures. *Soft Matter*, 10:1665–1675, 2014.

[130] M. Reza Parsa and Alexander J. Wagner. Lattice gas with molecular dynamics collision operator. *Phys. Rev. E*, 96:013314, Jul 2017.